2-D Analytical Modeling and Simulation of Electrical Characteristics of Ultrathin Body CG HD-GC-JAM MOSFET

3.1 Introduction

Various device engineering techniques like the gate-electrode-material engineering (Dubey *et al.*, 2008) (i.e., use of multiple metal-like materials in cascade to form the gate electrode contact), hetero dielectric stacking (Mitra, Goswami and Bhowmick, 2016) (i.e., replacing SiO_2 by a high-k dielectric or using a horizontal or vertical stacking of SiO_2/high-k) and channel doping engineering (Pratap *et al.*, 2014a; Goel *et al.*, 2016a) (i.e., using different channel doping profile other than uniform doping in the channel) have been discussed in Chapter-1 for improving the performance characteristics of the MOS transistors. In Chapter-2, we have modelled the combined effects of graded channel (GC) engineering and dual material (DM) engineering in CG JAM MOSFET. The literature survey in Chapter-1 shows that the use of a vertically/laterally stacked high-k/SiO_2 gate-oxide structure in the MOS transistors can reduce the gate leakage current and improves the drain current (Pratap *et al.*, 2016). That is why, the present chapter is devoted to consider the modelling of effect of a laterally stacked HfO_2/SiO_2 hetero-dielectric (HD) gate-oxide structure on the electrical characteristics of an ultrathin nanowire based cylindrical gate (CG) graded channel (GC) JAM MOSFET (CG HD-GC JAM MOSFET). The HfO_2 (high-k) oxide near the source side is used to enhance the source/channel barrier potential and hence the I_{ON} current due to increase in the gate capacitance (Pratap *et al.*, 2016), whereas the asymmetric halo-doped graded channel (GC) is used to decrease the HCEs by reducing the electric field near the drain side (Chen *et al.*, 2013). The combined effects in

the proposed JAM MOSFET structure are used to improve its I_{ON}/I_{OFF} ratio with reduced SCEs and HCEs.

Section 3.2 presents fabrication feasibility and 2-D analytical model formulation of CG HD-GC JAM MOSFET. The 2-D Poisson's equation in cylindrical coordinate system has been solved by using the superposition method for the central channel potential of the device. The potential function is then used to obtain the lateral electric field, threshold voltage, roll-off, DIBL, g_m, g_d and SS of HD-GC-JAM MOSFETs. Quantum correction has also been included in the model for improving the accuracy of the threshold voltage of the device for a channel radius below 5 nm. An effective model for total drain current (I_D-V_{GS} and I_D-V_{DS}) including GIDL has been formulated to study the effects of negative bias stability in JAM MOSFETs. Some important model results and related discussions have been presented in Sec. 3.3. Finally, Sec. 3.4 concludes the major observations of the present chapter.

3.2 Device fabrication and model formulation

It is believed that the proposed HD-GC JAM MOSFET structure can be fabricated by exploring the asymmetric halo doping of GC MOSFET (Pavanello, Martino and Flandre, 2001) and SiO_2 wet etching followed by atomic layer deposition of HfO_2 as in HD FET (Lee, Jang and Choi, 2013) fabrication processes along with the nanowire MOSFET (Lee *et al.*, 2010) fabrication technology. A schematic of vertical CG HD-GC JAM MOSFET fabrication process has been shown in fig 3.1.

Figure 3.2 shows the 3-D view of the simulated HD-GC-JAM-MOSFET structure, and its corresponding 2-D view is shown in Fig. 3.3. Here $L = L_1 + L_2$ is the total length of the channel with L_1 and L_2 as the control and screen gate lengths, respectively. Two different gate dielectric oxides of uniform thickness t_{ox} have been used for the control and screen gate regions. The HfO_2 is used as the high-k gate dielectric in the control gate region (Region 1) while the

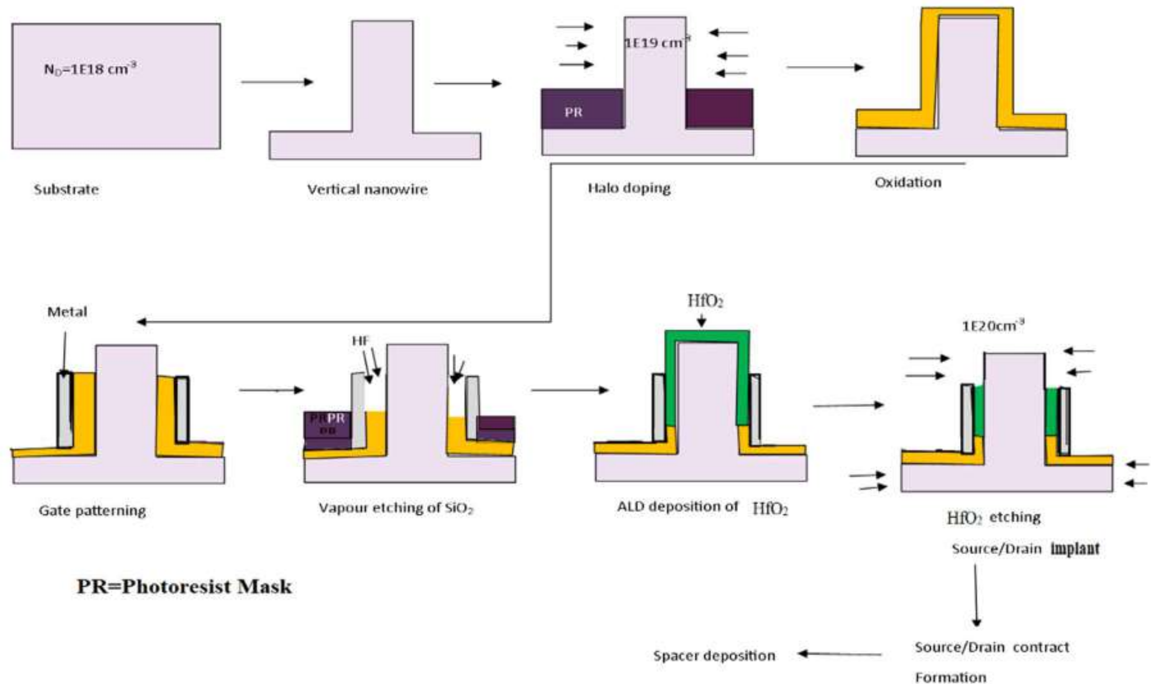

Fig. 3.1: A schematic of HD-GC-JAM MOSFET fabrication steps.

conventional SiO_2 has been considered as the gate dielectric in the screen gate region (Region 2). To control the DIBL effect in short channel MOSFETs the channel radius should also be scaled down to ultra-thin body. Quantum mechanical effects have been considered while modeling channel radius below 5 nn (Wang, 2006). The channel is assumed to be fully depleted under

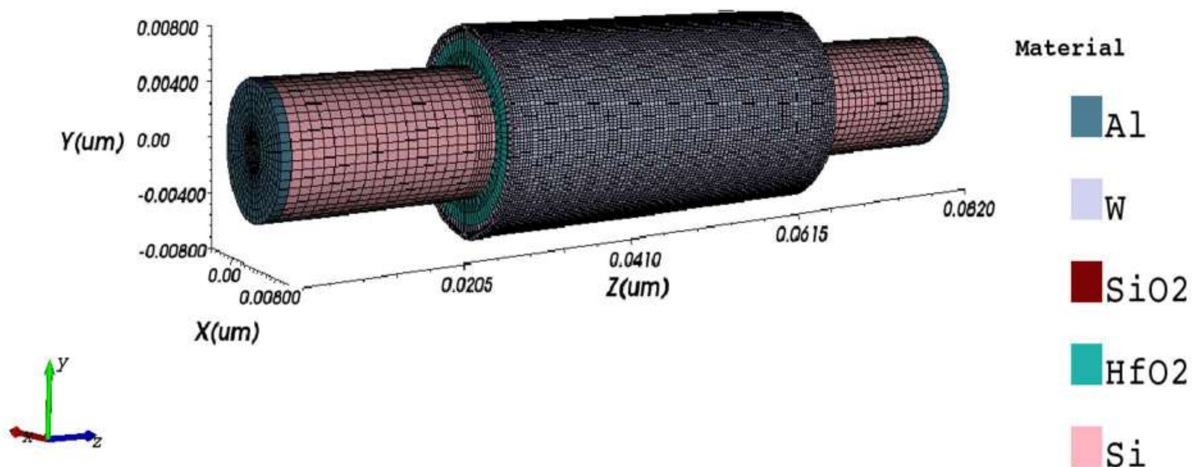

Fig. 3.2: 3-D view of nanowire HD-GC-JAM- MOSFET.

no bias condition of the device. Since source (drain) doping is much higher than the channel doping, the depletion region extension in the source (drain) regions at source/channel (drain/channel) junction have been neglected for the simplification of the model (Singh, 2016),(Holtij *et al.*, 2014; Trivedi *et al.*, 2016).

3.2.1 Modelling of Channel Potential

The channel potential distribution of the cylindrical MOSFETs is invariant in θ in the cylindrical coordinate system. Suppose that $\psi_1(r,z)$ and $\psi_2(r,z)$ represent the channel potential distribution functions in region-1 (R_1) and region-2 (R_2) under L_1 and L_2 sections with doping concentrations N_1 and N_2 respectively as shown in Fig. 3.3. Thus, the 2-D potential distribution $\psi_i(r,z)$ in the channel region R_i $(i = 1,\ 2)$ can be obtained by solving the following Poisson's equations:

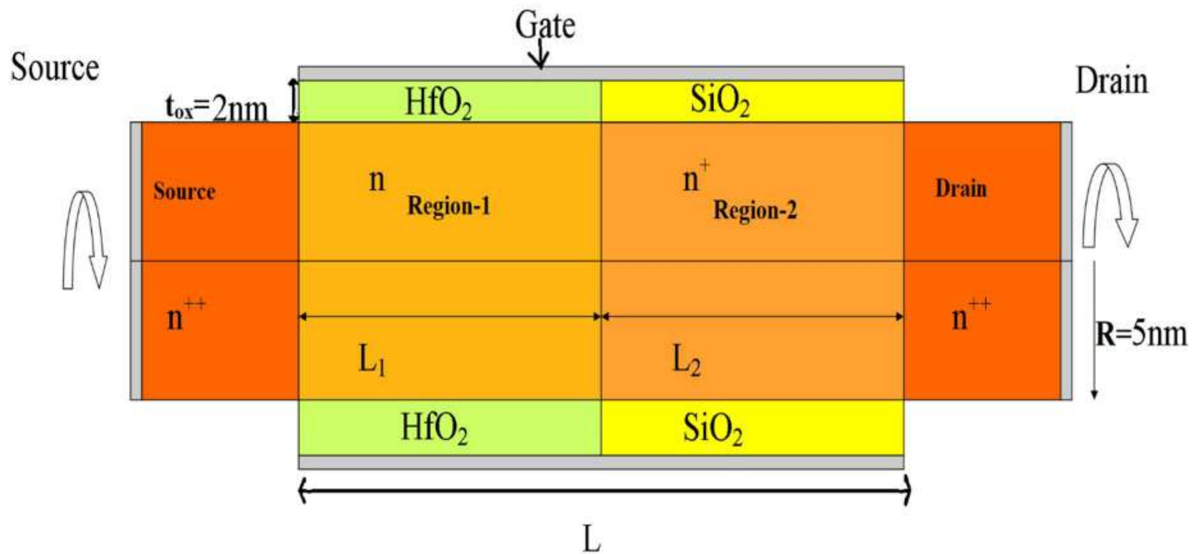

Fig. 3.3: Cross-section view of nanowire HD-GC-JAM- MOSFET

$$\frac{d^2\psi_i(r,z)}{dz^2} + \frac{1}{r}\frac{d}{dr}r\frac{d\psi_i(r,z)}{dr} = -\frac{qN_i}{\varepsilon_{Si}},\ i = 1,2\ , \tag{3.1}$$

where q and $\varepsilon_{Si}$are electron charge (1.632×10^{-19} C) and permittivity of silicon (8.85×10^{-12} F/m) respectively.

Applying the superposition technique, the solution of the Poisson's equation can be expressed as: $\psi_i(r,z) = \nu_i(r,z) + \phi_i(r)$ (3.2)

where $\phi_i(r)$ is the solution a 1-D Poison's equation and$\nu_i(r,z)$ is the solution of the 2-D Laplace equation described respectively as (Dubey *et al.*, 2008; Li *et al.*, 2013; Trivedi, Kumar, Haldar, S. S. Deswal, *et al.*, 2016):

$$\frac{1}{r}\frac{d}{dr}r\frac{d\phi_i(r)}{dr} = -\frac{qN_i}{\varepsilon_{Si}} \quad (3.3)$$

$$\frac{d^2\nu_i(r,z)}{dz^2} + \frac{1}{r}\frac{d}{dr}r\frac{d\nu_i(r,z)}{dr} = 0 \quad (3.4)$$

In general, the bandgap in Si starts narrowing for a doping concentration above 10^{17} cm^{-3} (Singh *et al.*, 2017). Since the channel doping in junctionless MOSFETs is in the order ~10^{18} cm^{-3} (Trivedi *et al.*, 2016), the effect of bandgap narrowing should be considered for improving the accuracy of the model. Thus, the two effects have been incorporated into our present model in terms of the following equations:

$$\Delta E_{g,i} = \beta_E\left(ln(N_i/\beta_N) + \sqrt{ln(N_i/\beta_N)^2 + \beta_C}\right) \quad (3.5)$$

$$E_{g,i\ CL}^{eff} = E_g - \Delta E_{g,i} \quad (3.6)$$

$$\chi_i^{eff} = \chi + \Delta E_{g,i}/2 \quad (3.7)$$

where, $\beta_E = 6.92 \times 10^{-3}$eV, $\beta_N = 1.3 \times 10^{17}$$cm^{-3}$and $\beta_C = 0.5$ are some empirical constants at room temperature; E_g and χ are the energy band gap and electron affinity, $E_{g,i\ CL}^{eff}$ and $\chi_i^{eff}$are the effective energy band gap for classical modeling and electron affinity of the channel material after incorporating the above model in R_1 and R_2 regions respectively.

3.2.1.1 Energy band gap correction for quantum effects

The effects of quantum confinements should be considered while considering a channel radius below 5 nm. In the subthreshold region with negligible mobile charges, the Poisson-Schrödinger could be solved in a decoupled manner. Further, considering the quantum confinement in the transverse direction we could write as (Wang, 2006):

$$-\frac{\hbar^2}{2m_e}\left[\frac{d^2}{dr^2}+\frac{1}{r^2}\frac{d}{dr}+\frac{1}{r^2}\frac{d^2}{d\theta^2}\right]\lambda(r,\theta)+(U-E)\lambda(r,\theta)=0 \tag{3.8}$$

where, m_e is the effective mass; $\lambda(r, \theta)$ is the wave function; $U(r, \theta)$ is the potential; E is the discretized energy of the conduction band and $\left(\hbar=\frac{h}{2\pi}\right)$ is the modified Plank's constant. Using the separation of variables method, the solution of (29) could be written as [25]:

$$\lambda(r,\theta)=\Omega_1 J_l\left(\kappa_{l,n}\frac{r}{R}\right) \tag{3.9}$$

where, $\Omega_1=\frac{1}{\int_0^{2\pi}d\theta\int_0^R r|\lambda(r,\theta)|^2 dr}$, l and n are the angular and radial quantum number, respectively; $\kappa_{l,n}$ is the nth zero of the lth order Bessel's function; $\kappa_{l,n}$ can be found by following boundary condition (Tsormpatzoglou *et al.*, 2009):

$$\lambda(R,\theta)=0 \tag{3.10}$$

Further, each electron corresponds to six different ellipsoidal surfaces of constant energy with an effective mass of m_l=0.97m_0 and m_t=0.19m_0 along the longitudinal and transverse direction, where m_0=9.1x10^{-31} Kg is mass of the free electron. The confinement mass of electron in transverse valleys could be approximated as cylindrical mass $m_c=\frac{2m_t m_l}{m_t+m_l}=0.315m_0$ and for longitudinal valleys as m_t=0.19m_0 (Tsormpatzoglou *et al.*, 2009). Due to quantum confinement, the continuous energy band takes discrete values and there is a widening of band gap given as (Wang, 2006; Tsormpatzoglou *et al.*, 2009; Chiang and Liou, 2013):

$$\Delta E_c=\frac{\hbar^2\kappa^2{}_{l,n}}{2R^2 m_e} \tag{3.11}$$

where $\frac{1}{m_e} = \frac{1}{m_c} + \frac{1}{m_t}$, applying this quantum correction factor and accounting for bandgap widening (Chiang and Liou, 2013):

$$E_{g,i}^{eff}{}_{QM} = E_{g,i}^{eff}{}_{CL} + \Delta E_c \tag{3.12}$$

where $E_{g,i}^{eff}{}_{QM}$ is effective bandgap for quantum modeling.

The 1-D (i.e., long channel) potential $\phi_i(r)$ and 2-D (*i.e.,* short-channel) potential $\nu_i(r,z)$ can be obtained by solving the respective 1-D Poisson and 2-D Laplace equations using following boundary conditions (Pratap *et al.*, 2014; Trivedi *et al.*, 2016):

$$\left.\frac{d\psi_i(r,z)}{dr}\right|_{r=0} = 0 \tag{3.13}$$

$$\varepsilon_{Si} \left.\frac{d\psi_i(r,z)}{dr}\right|_{r=R} = C_{ox,i}\left[V_{GS} - V_{fb,i} - \psi_i(r,z)\right] \tag{3.14}$$

$$\varepsilon_{Si} \left.\frac{d\nu_{(i)}(r,z)}{dr}\right|_{r=R} = C_{ox(i)}[\nu_i(r,z)] \tag{3.15}$$

$$\nu_1(r,0) = V_{bi,1} - \phi_1(r) \tag{3.16}$$

$$\nu_2(r,L) = V_{bi,2} - \phi_2(r) + V_{DS} \tag{3.17}$$

$$V_{bi,(1,2)} = V_T \, ln\left(N_{S,D}/N_i\right) \tag{3.18}$$

where, V_{GS} and V_{DS} are the gate-to-source and drain-to-source voltages, respectively; $V_{fb,i} = \varphi_m - \varphi_{s,i}$ is the flat band voltage for regions $R_i (i = 1,\ 2)$ where φ_m is the gate-electrode metal work function and $\varphi_{s,i} = \chi_i^{eff} + E_{g,i}^{eff}{}_{CL/QM}/2q - \varphi_{fi}$ is the channel material work function with $\varphi_{fi} = V_T \, ln(N_i/n_i)$as the Fermi potential with V_T as the thermal voltage and n_i as the intrinsic carrier concentration; $\varepsilon_{ox,i}$ and $C_{ox,i} = \varepsilon_{ox,i}/t_{ox}$ are the gate oxide permittivity and gate-oxide capacitance for region R_i respectively; $t_{ox'} = R \, ln(1 + t_{ox}/R)$ is the effective

gate-oxide thickness (Li *et al.*, 2013) where R is the radius of the channel; V_{bi1} (V_{bi2}) represents the barrier potential at source/channel (drain/channel) junction.

Now the potential functions $\phi_i(r)$ and $v_i(r,z)$ can be expressed as (Trivedi *et al.*, 2016):

$$\phi_i(r) = \left[\frac{-qN_i}{4\varepsilon_{Si}} r^2 + \frac{qN_i R^2}{4\varepsilon_{Si}} - \frac{qN_i R}{2C_{ox}} + V_{GS} - V_{fb,i}\right] \tag{3.19}$$

$$v_i(r,z) = \sum_1^{\infty} J_0\left(\frac{\beta_{n,i}\, r}{R}\right)\left[C_{n,i}\, e^{\frac{\beta_{n,i} z}{R}} + D_{n,i}\, e^{\frac{-\beta_{n,i} z}{R}}\right] \tag{3.20}$$

where $\beta_{n,i}$ are the eigenvalues to be obtained by solving the following equation:

$$J_0(\beta_{n,i}) = -\frac{\varepsilon_{Si}\beta_{n,i}}{C_{ox,i}R} J_1(\beta_{n,i}) \tag{3.21}$$

where J_0 and J_1 are the Bessel's function of order 0 and 1, respectively; $C_{n,i}$ and $D_{n,i}$ are arbitrary constants for the region $R_i (i = 1,\ 2)$ which can be determined by using the following boundary conditions:

$$\psi_1(r, L_1) = \psi_2(r, L_1) \tag{3.22}$$

$$\frac{d\psi_1(r,L_1)}{dz} = \frac{d\psi_2(r,L_1)}{dz} \tag{3.23}$$

Now $C_{n,i}$ and $D_{n,i}$ $(i = 1,\ 2)$ can be expressed as

$$\begin{pmatrix} \boldsymbol{C_{n,1}} \\ \boldsymbol{D_{n,1}} \end{pmatrix} = \frac{1}{\Delta_1}\begin{pmatrix} \mathbf{1} & P_{11} \\ \mathbf{-1} & P_{12} \end{pmatrix} \begin{pmatrix} A_{11} + Q_{11} \\ D_{11} \end{pmatrix} \tag{3.24}$$

$$\begin{pmatrix} \boldsymbol{C_{n,2}} \\ \boldsymbol{D_{n,2}} \end{pmatrix} = \frac{1}{\Delta_2}\begin{pmatrix} exp(-\beta_{n,2}L/R) & P_{21} \\ -\,exp(\beta_{n,2}L/R) & P_{22} \end{pmatrix} \begin{pmatrix} A_{12} + Q_{12} \\ D_{12} \end{pmatrix} \tag{3.25}$$

where, $P_{11} = \left[\frac{\beta_{n,1}}{\beta_{n,2}} \boldsymbol{sinh}\left(\frac{\beta_{n,2}\boldsymbol{L_2}}{\boldsymbol{R}}\right) - \boldsymbol{cosh.}\left(\frac{\beta_{n,2}\boldsymbol{L_2}}{\boldsymbol{R}}\right)\right] \exp\left(\frac{-\boldsymbol{\beta_{n1,}L_1}}{\boldsymbol{R}}\right)$ (3.26)

$$P_{12} = \left[\frac{\beta_{n,1}}{\beta_{n,2}} \boldsymbol{sinh}\left(\frac{\beta_{n,2}\boldsymbol{L_2}}{\boldsymbol{R}}\right) + \boldsymbol{cosh}\left(\frac{\beta_{n,2}\boldsymbol{L_2}}{\boldsymbol{R}}\right)\right] \exp\left(\frac{\beta_{n,1}\boldsymbol{L_1}}{\boldsymbol{R}}\right) \tag{3.27}$$

$$P_{21} = -\left[\frac{\beta_{n,2}}{\beta_{n,1}}\boldsymbol{sinh}\left(\frac{\beta_{n,1}\boldsymbol{L_1}}{\boldsymbol{R}}\right) + \boldsymbol{cosh}\left(\frac{\beta_{n,1}\boldsymbol{L_1}}{\boldsymbol{R}}\right)\right]\exp\left(\frac{-\beta_{n,2}\boldsymbol{L_1}}{\boldsymbol{R}}\right) \quad (3.28)$$

$$P_{22} = \left[\boldsymbol{cosh}\left(\frac{\beta_{n,1}\boldsymbol{L_1}}{\boldsymbol{R}}\right) - \frac{\beta_{n,2}}{\beta_{n,1}}\boldsymbol{sinh}\left(\frac{\beta_{n,1}\boldsymbol{L_1}}{\boldsymbol{R}}\right)\right]\exp\left(\frac{\beta_{n,2}\boldsymbol{L_1}}{\boldsymbol{R}}\right) \quad (3.29)$$

$$Q_{11} = \boldsymbol{cosh}\left(\frac{\beta_{n,2}\boldsymbol{L_2}}{\boldsymbol{R}}\right)(\boldsymbol{B_{11}} + \boldsymbol{C_{11}}) \quad (3.30)$$

$$Q_{12} = \boldsymbol{cosh}\left(\frac{\beta_{n,1}\boldsymbol{L_1}}{\boldsymbol{R}}\right)(\boldsymbol{B_{12}} + \boldsymbol{C_{12}}) \quad (3.31)$$

$$\Delta_2 = -2\left[cosh\left(\frac{\beta_{n,1}L_1}{R}\right)sinh\left(\frac{\beta_{n,2}L_2}{R}\right) + \frac{\beta_{n,2}}{\beta_{n,1}}sinh\left(\frac{\beta_{n,1}L_1}{R}\right)cosh\left(\frac{\beta_{n,2}L_2}{R}\right)\right] \quad (3.32)$$

$$\Delta_1 = 2\left[cosh\left(\frac{\beta_{n,2}L_2}{R}\right)sinh\left(\frac{\beta_{n,1}L_1}{R}\right) + \frac{\beta_{n,1}}{\beta_{n,2}}sinh\left(\frac{\beta_{n,2}L_2}{R}\right)cosh\left(\frac{\beta_{n,1}L_1}{R}\right)\right] \quad (3.33)$$

$$A_{11} = \frac{w_1(V_{bi2}+b_2V_2-w_2a_2+V_{DS})}{u_1w_2}, B_{11} = \frac{w_2b_1V_1-w_1b_2V_2}{w_2u_1} \quad (3.34)$$

$$C_{11} = \frac{w_1(a_2-a_1)}{u_1}, \quad D_{11} = \frac{V_{bi1}+b_1V_1-w_1a_1}{u_1} \quad (3.35)$$

$$A_{12} = \frac{w_2(V_{bi1}+b_1V_1-w_1a_1)}{u_2w_1}, \quad B_{12} = \frac{w_1b_2V_2-w_2b_1V_1}{w_1u_2} \quad (3.36)$$

$$C_{12} = \frac{w_2(a_1-a_2)}{u_2}, \ D_{12} = \frac{V_{bi2}+V_{DS}+b_2V_2-w_2a_2}{u_2} \quad (3.37)$$

$$u_i = \frac{\beta_{n,i}^2[{J_0}^2(\beta_{n,i})+{J_1}^2(\beta_{n,i})]}{2}, w_i = \beta_{n,i}J_1(\beta_{n,i}), b_i = \frac{-qN_iR^2}{4\varepsilon_{Si}} \quad (3.38)$$

$$V_i = [\beta_{n,i}J_1(\beta_{n,i}) - 2J_2(\beta_{n,i})], a_i = \left[V_{GS} - V_{fbi} + \frac{qN_iR^2}{4\varepsilon_{Si}} + \frac{qN_iR}{2C_{oxi}}\right] \quad (3.39)$$

3.2.1.2 Modelling of the lateral electric field

Electric field could be defined as a gradient of potential and can be expressed as:

$$\xi_{x,i} = -\frac{d\psi_i(r,z)}{dz}, (i = 1,\ 2) \quad (3.40)$$

$$\xi_{x,i} = \sum_1^\infty J_0\left(\frac{\beta_{n,i}r}{R}\right)\frac{\beta_{n,i}}{R}\left[C_{n,i}\,exp(\beta_{n,i}z/R) - D_{n,i}\,exp(-\beta_{n,i}z/R)\right] \quad (3.41)$$

3.2.2 Modelling of the threshold voltage

The threshold voltage (V_{th}) is an important parameter for any MOS device. It can be defined as the gate-to-source voltage at which the minimum central potential is equal to the intrinsic Fermi potential for a junctionless device (Gupta, 2015). Since the region R_1has a lower doping than the regionR_2, the minimum potential will lie in the R_1 region. The location of the minimum central potential can be obtained by solving

$$\left.\frac{d\left(\psi_i(r,z)|_{\langle E_{g,i}^{eff}{}_{CL}\rangle/\langle E_{g,i}^{eff}{}_{QM}\rangle}\right)}{dz}\right|_{r=0,z=z_{min}} \tag{3.42}$$

where $\psi_i(r,z)|_{\langle E_{g,i}^{eff}{}_{CL}\rangle/\langle E_{g,i}^{eff}{}_{QM}\rangle}$ is the 2-D potential distribution for classical and quantum (considering quantum band gap widening), respectively.

which gives

$$z_{min} = \frac{R}{2\beta_n} ln\left(\frac{D_{n,j}}{C_{n,j}}\right) \tag{3.43}$$

$$\psi_{min}(r, z_{min}) = V_{GS} + a_{0j}\sqrt{C_{n,j}D_{n,j}} \tag{3.44}$$

where, $a_{0i} = a_i - V_{GS}$.

Now, equating the minimum potential to the Fermi potential (φ_{fi}) and changing V_{GS} to V_{th}, the threshold voltage, V_{th}, can be obtained as (Chiang and Liou, 2013):

$$\psi_{min}(r, z_{min})|_{V_{GS}=V_{th}} = \varphi_{fi} \tag{3.45}$$

which give $\left.\left(V_{gs} + 2\sqrt{C_{n,i}D_{n,i}}\right)\right|_{V_{GS}=V_{th}} = V_{tL}$ (3.46)

where V_{tL} is the long channel threshold voltage given by

$$V_{tL} = \varphi_{fi} - a_{0i} \tag{3.47}$$

Since the minimum central potential lies in the R_1region, we can be written as (Martinez *et al.*, 2010; Ferain, Colinge and Colinge, 2011):

$$A_{11} = E_{12} - F_{12}V_{th} \text{ and } D_{11} = E_{11} - F_{11}V_{th} \tag{3.48}$$

$$\text{where, } C_{1,n}D_{1,n} = G_1 + G_2V_{th} + G_3{V_{th}}^2 \tag{3.49}$$

Now, the threshold voltage can be expressed as:

$$\partial_1{V_{th}}^2 + \partial_2V_{th} + \partial_3 = 0 \tag{3.50}$$

$$E_{11} = \frac{1}{u_1}[V_{bi1} + b_1V_1 - w_1a_{01})], \qquad F_{11} = \frac{w_1}{u_1} \tag{3.51}$$

$$E_{12} = \frac{1}{u_2w_2}[w_1(V_{bi2} + b_2V_2 - w_2a_{02} + V_{DS})], F_{12} = \frac{w_1}{u_2} \tag{3.52}$$

$$G_1 = M_{11}M_{21}, G_2 = M_{11}M_{22} + M_{12}M_{21}, G_3 = M_{12}M_{22} \tag{3.53}$$

$$\partial_1 = 4G_3 - 1, \partial_2 = 4G_2 + 2V_{tL}, \partial_3 = 4G_1 - {V_{tL}}^2 \tag{3.54}$$

$$M_{11} = \frac{1}{\Delta_1}\left[E_{12} + N_{11} - E_{11}[N_{13} - N_{12}]exp\left(\frac{-\beta_{n,1}L_1}{R}\right)\right] \tag{3.55}$$

$$M_{12} = \frac{1}{\Delta_1}\left[F_{11}[N_{13} - N_{12}]exp\left(\frac{-\beta_{n,1}L_1}{R}\right) - F_{12}\right] \tag{3.56}$$

$$M_{21} = \frac{1}{\Delta_1}\left[-E_{12} - N_{11} + E_{11}[N_{13} + N_{12}]exp\left(\frac{\beta_{n,1}L_1}{R}\right)\right] \tag{3.57}$$

$$M_{22} = \frac{1}{\Delta_1}\left[F_{12} - F_{11}[N_{13} + N_{12}]exp\left(\frac{\beta_{n,1}L_1}{R}\right)\right] \tag{3.58}$$

$$N_{11} = cosh\left(\frac{\beta_{n,2}L_2}{R}\right)[B_{11} + C_{11}] \tag{3.59}$$

$$N_{12} = cosh\left(\frac{\beta_{n,2}L_2}{R}\right), N_{13} = \frac{\beta_{n,1}}{\beta_{n,2}}sinh\left(\frac{\beta_{n,2}L_2}{R}\right) \tag{3.60}$$

which gives

$$V_{th} = \frac{-\partial_2 \pm \sqrt{(\partial_2{}^2 - 4\partial_1\partial_3)}}{2\partial_1} \tag{3.61}$$

Since the threshold voltage of a Junctionless MOSFET is always positive in the simulations, the positive sign has been considered in Eq. (61).

3.2.2.1 Modeling of threshold voltage roll-off and DIBL

The threshold voltage roll-off can be defined as the difference in threshold voltage between the short channel and long channel device and can be expressed as (Dubey *et al.*, 2013)

$$V_{roll-off} = V_{th}|_{short-channel} - V_{tL} \tag{3.62}$$

The drain induced barrier lowering (DIBL) can be expressed as (Goel *et al.*, 2016):

$$DIBL = -\frac{V_{th}|_{V_{DS}=0.05\text{V}} - V_{th}|_{V_{DS}=1\text{V}}}{V_{DS}(0.05\text{V}) - V_{DS}(1\text{V})} \quad \text{mV/V} \tag{3.63}$$

3.2.3 Modelling of the Drain Current

Drain current of a device is an important parameter for switching purposes. Higher the ratio of I_{ON}/I_{OFF} higher is the noise tolerance of the device. A complete drain current model for different regions could be expressed as (Trivedi *et al.*, 2016);

$$I_D = \begin{bmatrix} I_{btbt} for - 1V \leq V_{GS} \leq 0V \\ I_{sub} for 0V < V_{GS} \leq V_{th} \\ I_{sat} for V_{th} < V_{GS} \leq V_{DS} + V_{th} \\ I_{lin} for V_{DS} + V_{th} < V_{GS} \leq V_{DD} \end{bmatrix} \tag{3.64}$$

For I_D- V_{DS} analysis when, $V_{GS} > V_{th}$

$$I_D = \begin{bmatrix} I_{lin} for V_{DS} < V_{GS} - V_{th} \\ I_{sat} for V_{DS} \geq V_{GS} - V_{th} \end{bmatrix} \tag{3.65}$$

I_{btbt} could be defined as the gate induced drain leakage due to band-to-band tunneling in the overlap region near the drain junction. BTBT generation rate could be defined as (Bouhdada *et al.*, 1997; Sachdeva, Vashishath and Bansal, 2018);

$$BTBT_{gen} = A \times E^2{}_{tot}\, exp\left(\frac{-B}{E_{tot}}\right) \tag{3.66}$$

where, $A = \frac{q^2 m_r{}^{0.5}}{18\pi h^2 E_{g,2}{}^{0.5}}$ and $B = \frac{\pi m_r{}^{0.5} E_{g,2}{}^{0.5}}{2\sqrt{2}qh} = 2.13MV/m$

$$E^2{}_{tot} = E^2{}_{si} + E^2{}_h \tag{3.67}$$

$$I_{btbt} = 2\pi R^2 \Delta L \times BTBT_{gen} \tag{3.68}$$

$$E_{si} = \frac{qN_{D,S}}{\varepsilon_{si}}\sqrt{\frac{2\varepsilon_{si}\psi_{si}}{qN_{D,S}}},\ E_h = \frac{V_{DS}-V_{GS}}{\left(\frac{\varepsilon_{si}}{\varepsilon_{ox}}t_{ox}\varpi\right)^2} \tag{3.69}$$

$$\psi_{si} = (V_{DS} - V_{GS}) - V_{fb,2} + \frac{qN_{D,S}t^2{}_{ox}\varepsilon_{si}}{\varepsilon^2{}_{ox}} \times \left[\sqrt{\left[\frac{qN_{D,S}t^2{}_{ox}\varepsilon_{si}}{\varepsilon^2{}_{ox}} + (V_{DS} - V_{GS}) - V_{fb,2}\right]^2 - \left((V_{DS} - V_{GS}) - V_{fb,2}\right)^2}\right] \tag{3.70}$$

$$\varpi = \frac{10^{-4}R^{2/3}L^{2/5}}{t^{3/4}{}_{ox}},\Delta L = \sqrt{\frac{2\varepsilon_{si}\psi_{si}}{qN_{D,S}}}, \tag{3.71}$$

where, ΔL is the length of the overlapped area, m_r=0.315m_0 where, m_0 is mass of the electron at rest, E_{si} and E_h are vertical and horizontal field respectively and h is the plank constant (Chen, Wong and Wang, 2001).

I_{sub} could be calculated by a minimum potential method as;

$$I_{sub} = 2\pi R^2 \mu_{eff,1} q V_T n_{i,1}\left(\frac{1-\exp\left(\frac{-V_{DS}}{V_T}\right)}{\int_0^L \frac{1}{\int_0^R \exp\left(\frac{\psi_{min}(r, z_{min})}{V_T}\right)dr}dz}\right) \tag{3.72}$$

As the minimum potential is highest for region-1, only region-1 is taken for the calculation

$$\mu_{eff,i} = \frac{\mu_{max} - \mu_{min}}{1+\left(\frac{N_i}{N_{ref}}\right)^{\tau}}, \tag{3.73}$$

μ_{max}=1330 and μ_{min}=65 cm^2/Vs, N_{ref}=8.5×10^{16}/cm^3, $\tau = 0.73$

$$I_{sat} = \frac{2\pi R\mu_{eff,2}C_{ox,2}}{\left(1+\frac{V_{Dsat}}{E_C L}\right)(L-L_{sat})}\left[\rho(V_{GS}-V_{ths})^{\gamma}V_{Dsat} - \frac{\theta_S V^2{}_{Dsat}}{2} + V_T\theta_s(1+exp\left(\frac{V_{DS}-V_{Dsat}}{V_T}\right)\right] \quad (3.74)$$

$$\theta_s = 0.1 \Big/ \frac{\partial\psi_{\min}(0,z_{\min})}{\partial V_{GS}} \quad \text{at} \quad V_{GS} = V_{th} \quad (3.75)$$

$$V_{ths} = V_{th}(1-\theta_s), \quad E_C = \frac{2V_{sat}}{\mu_{eff,2}} \quad (3.76)$$

$$V_{Dsat} = \frac{V_{GS}-V_{th}}{1+\frac{(V_{GS}-V_{th})\mu_{eff,2}}{LV_{sat}}} \quad (3.77)$$

$$L_{sat} = \lambda\, ln\left(\frac{V_{DS}-V_{Dsat}}{E_C L + \sqrt{1+\left(\frac{V_{DS}-V_{Dsat}}{E_C L}\right)^2}}\right) \quad (3.78)$$

where, γ is a fitting parameter varies between 0.5 to 1.5, γtaken here is 1.5. L_{sat} is defined as characteristics length and $\rho$is a technological dependent fitting parameter varying between 0 and 1, E_C is critical field V_{sat} is critical velocity.λ is also a fitting parameter whose value depends on permittivities and thickness of semiconductor and gate oxide. $V_{sat}$is the saturation velocity assumed as 1.03×10^7cm/s. Since the influence of the drain side is dominant during saturation$C_{ox,2}$ for Region-2 has been considered for saturation current calculations.

Current in the linear region could be calculated as below

$$I_{lin} == \frac{2\pi.R.\mu_{eff,1}.C_{ox,1}}{(E_C L+V_{DS})(L-L_{sat})}\left[\rho(V_{GS}-V_{ths})^{\gamma/2}V_{DS} - \frac{\theta_S V_{DS}{}^2}{2}\right] \quad (3.79)$$

3.2.3.1 Modelling transconductance and output conductance

Transconductance g_m and output conductance g_d are important parameters for analog applications and can be given as derivative of current I_D with V_{GS} and V_{DS} respectively.

$$g_m = \frac{\partial I_D}{\partial V_{GS}} \tag{3.80}$$

$$g_d = \frac{\partial I_D}{\partial V_{DS}} \tag{3.81}$$

3.2.3.2 Subthreshold slope modelling

Subthreshold slope (SS) is an essential parameter and important for DC analysis of the device. SS could be given as below;

$$SS = \frac{dV_{GS}}{d\,lo\ \ (I_{sub})} \tag{3.82}$$

3.3 Results and discussion

In this section, we have compared our model results of proposed HD-GC-JAM and GC-JAM MOSFETs with that of JAM MOSFET (Pratap *et al.*, 2014) for highlighting the merits of our proposed device. For fair comparisons, arithmetic mean of doping $N_1$and N_2 (graded channel) have been taken for the uniformly doped JAM MOSFET (Goel *et al.*,) Various parameters used for the computations are given in Table 3.1. The analytical results have been validated by comparing them with the 3-D COGENDA TCAD (Visual TCAD, 2017) simulation data. The *Fermi-Dirac*, *Lucent mobility*, *BGN*, *Trap,* and *BBT* models have been used for the carrier statistics, mobility, bandgap narrowing, trapping effect and band to band tunneling in the device, respectively. The *HotCarrier* model has been enabled in the TCAD simulator to account for the hot carrier effects. *DDML1* (drift-diffusion level model-I) solves simple drift-diffusion equations numerically and has been used for simulating the classical device (CL) with R≥5 nm. For devices R<5 nm, to include quantum confinement effects (QM) *QDDM* (quantum density model) solver which numerically solves Schrödinger-Poisson equation has been used. *EBML* (energy balance model) solver which accounts for hot carrier, impact ionization and numerically solves drift-diffusion equation with carrier temperature has been invoked for carrier temperature (Visual TCAD, 2017).

First of all, the TCAD simulation data have been calibrated against the experimental data in fig. 3.4 (a) for V_{DS}=1V. The electron mass of m_e=0.31m_0 and hole mass m_h=0.67m_o have been taken (Fan *et al.*, 2015). Fig. 3.4(b) shows carrier temperature variation against the length of the channel, whereas fig. 3.5 shows the contour plot of the same. Since HD-GC-JAM has the lowest electric field near the drain region, therefore less impact ionization (i.e., carrier with lower energies) and HCEs. Thus, it may be observed that carrier temperature (electron temperature) near the drain end is smaller for our proposed HD-GC-JAM MOSFETs than the conventional JAM and GC-JAM structures. Thus, the proposed HD-GC-JAM MOSFET is believed to have the highest immunity towards HCEs. Fig. 3.6 shows the variations of central potential as a function of channel length for L=40 and 20 nm. Among the three structures, the highest source to channel barrier observed in the HD-GC-JAM confirms its highest immunity to SCEs. Further, the shifting of the position of the minimum channel potential in both the GC-JAM and HD-GC-JAM MOSFETs confirms that they have better immunity to drain voltage variations than the JAM MOSFETs. The smaller source to channel barrier of 20 nm devices than the 40 nm device is attributed to the DIBL for short channel devices. Fig. 3.7 and 3.8 shows the central potential variations with the channel length for GC-JAM and HD-GC-JAM MOSFET for different L_1:L_2 ratios, respectively. The increase in the source-channel barrier

TABLE 3.1: Specifications of different JAM MOSFET structures

MOSFET Type	***Source/Drain Doping (N_S/N_D) (cm^{-3})***	***Channel Doping (cm^{-3}) N_1/N_2***	***Dielectric Gate-oxide***	***Gate Work-function (eV)***	***I_{on}/I_{off}***
HD-GC-JAM	10^{20}	10^{18}/10^{19}	HfO_2/SiO_2	4.9	2.03×10^{11}
GC-JAM	10^{20}	10^{18}/10^{19}	SiO_2	4.9	2.81×10^{10}
JAM	10^{20}	5×10^{18}	SiO_2	4.9	8.67×10^{8}

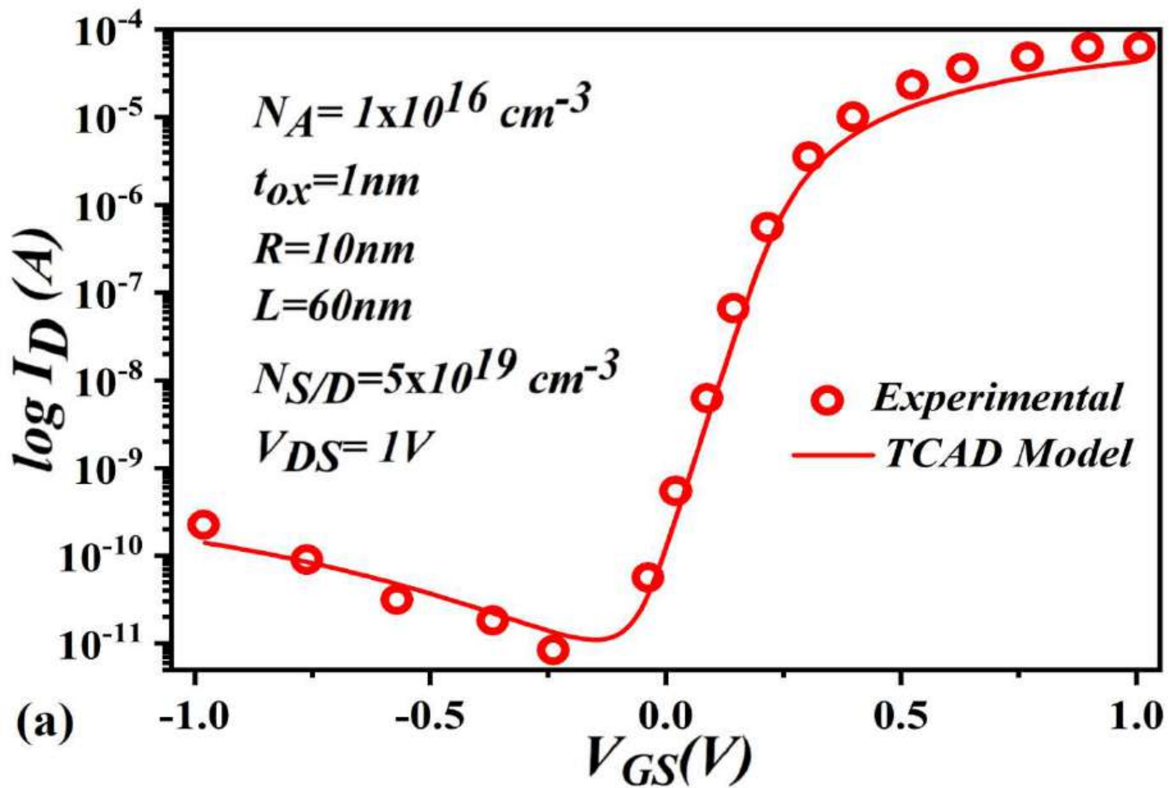

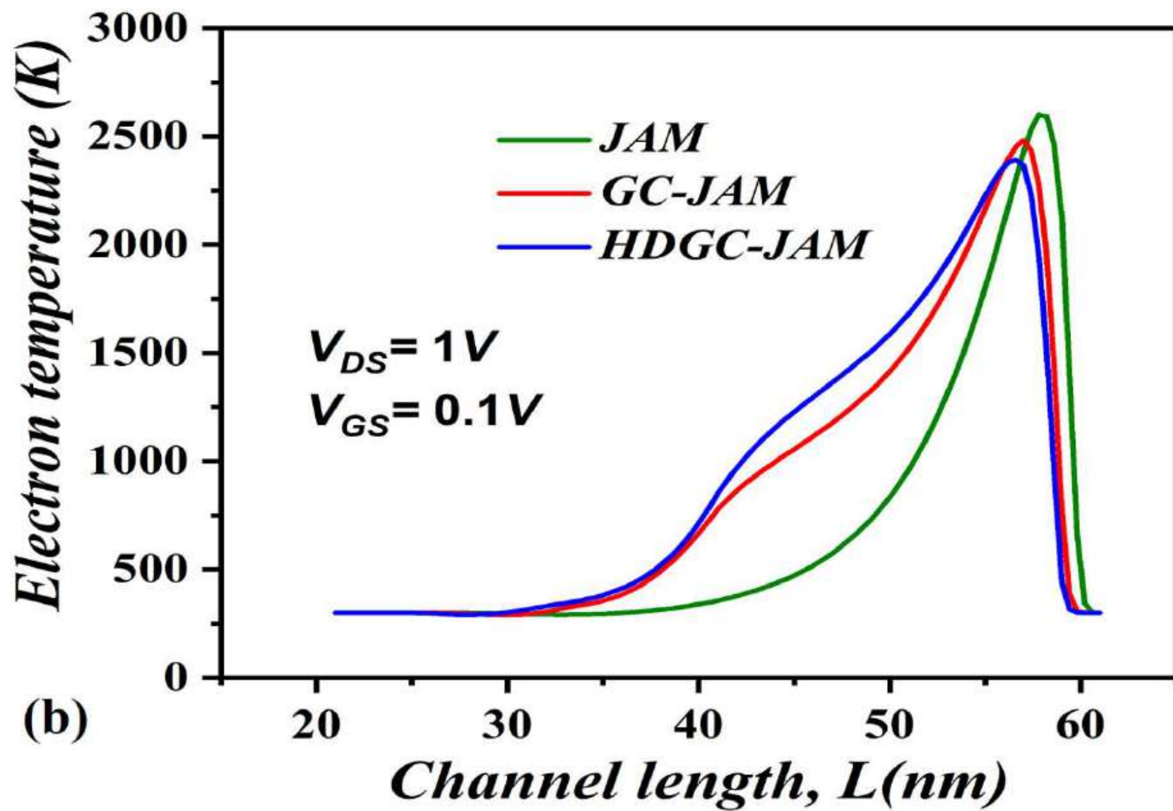

Fig. 3.4 : (a) Calibration of the simulation setup with the experimental results obtained in(Fan *et al.*, 2015); (b) Simulated carrier temperature variations against channel length for all compared devices.

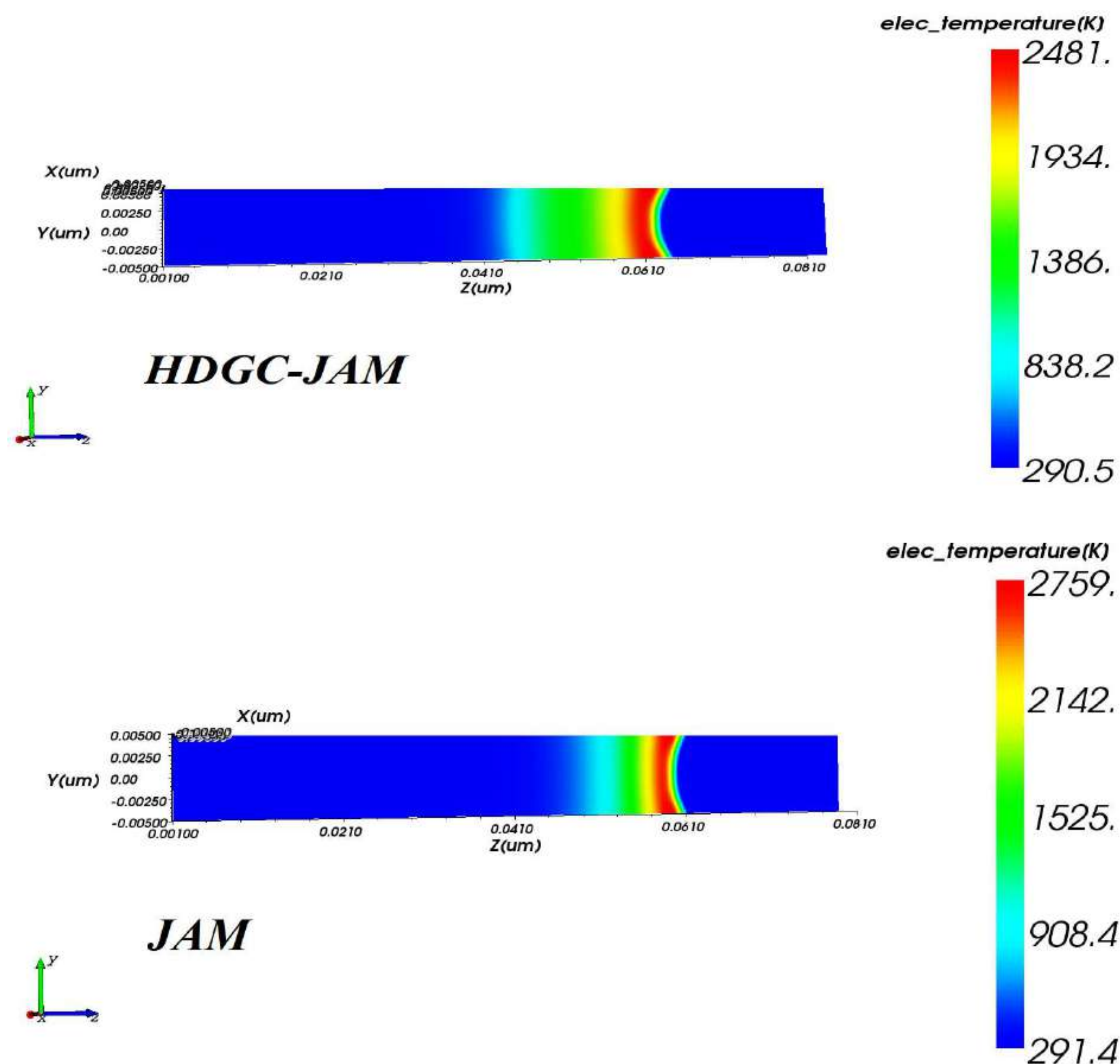

Fig. 3.5: Contour plot of carrier temperature against device length for HD-GC-JAM and JAM MOSFET.

with the L_1:L_2 ratio implies an increase in the threshold voltage and hence the improvement (i.e., decrease) in the SCEs. Further, the shifting of the minimum central potential position towards the drain with the increase in L_1:L_2 ratio implies a poor immunity to drain voltage variations (Mitra, Goswami and Bhowmick, 2016). Thus, the performance of the proposed device can be optimized for a suitable value of L1:L2 ratio. Fig. 3.9 shows the lateral electric field variation with channel lengths (L=20 nm and 40 nm) for all three different device structures under consideration at V_{GS}=0.1 V and V_{DS}=0.1 V (low electric field), V_{DS}=1 V (high

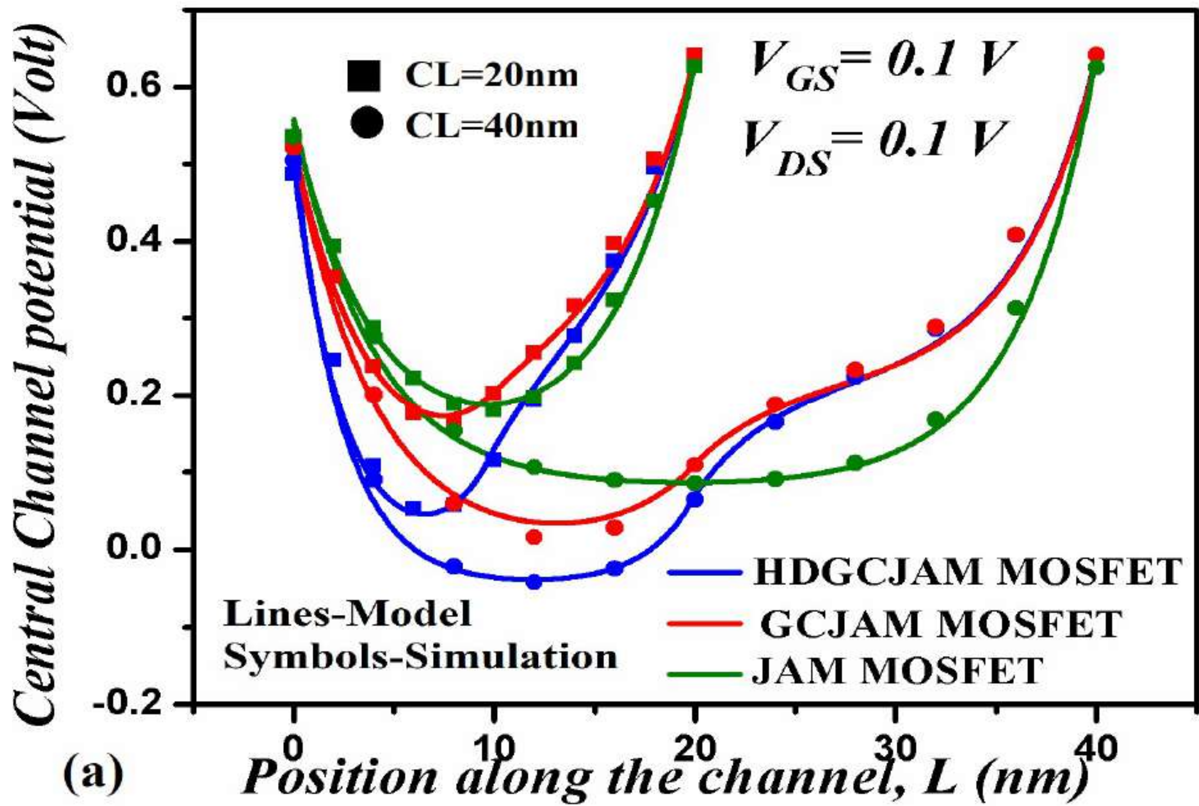

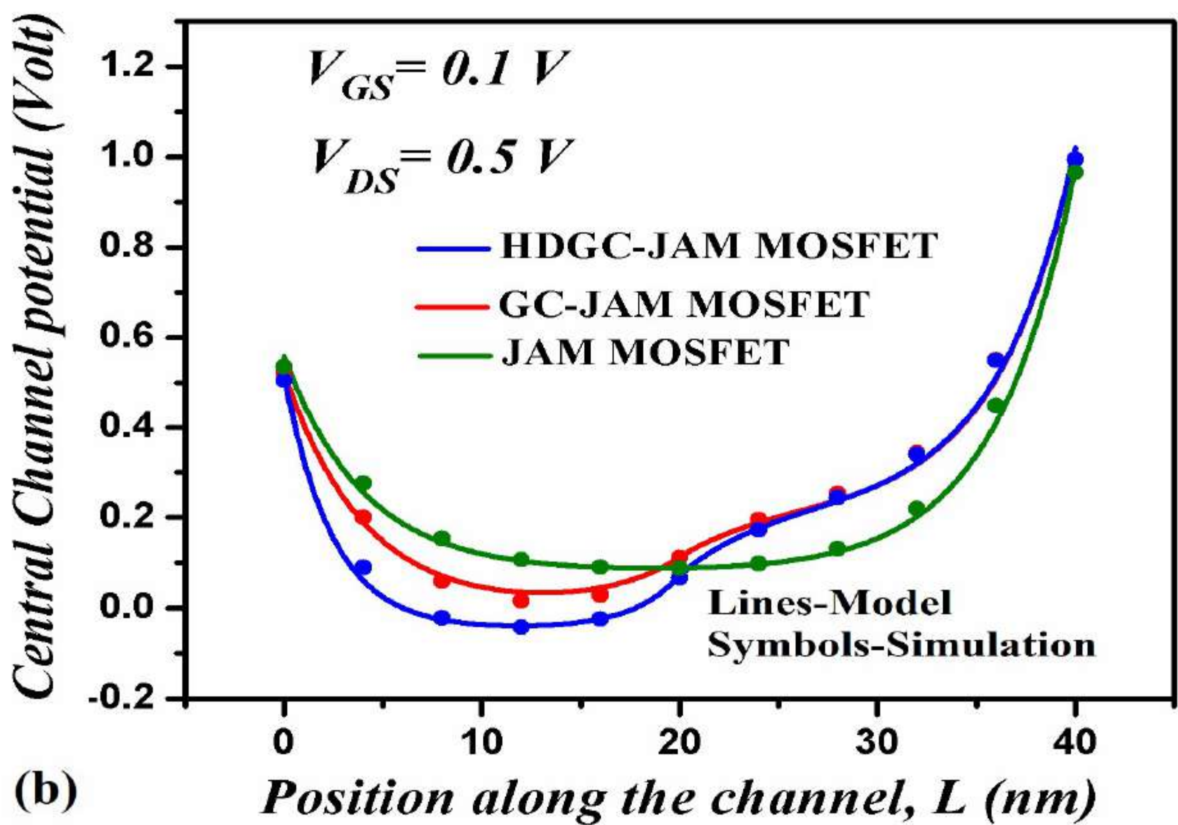

Fig. 3.6: Central channel potential along the channel length (a) for L=40 nm, L=20 nm at V_{DS}=V_{GS}=0.1 V; (b) L=40 nm at V_{GS}=0.1 V, V_{DS}=0.5 V for three different devices structures.

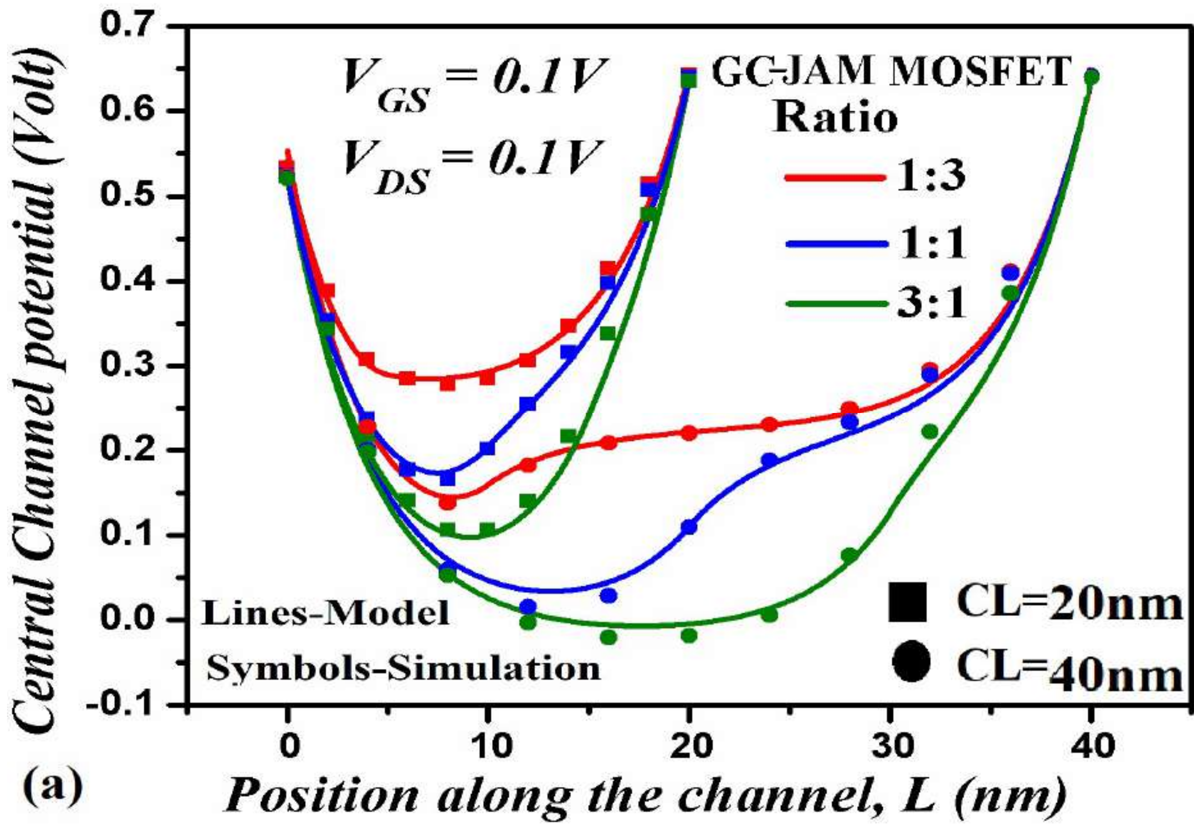

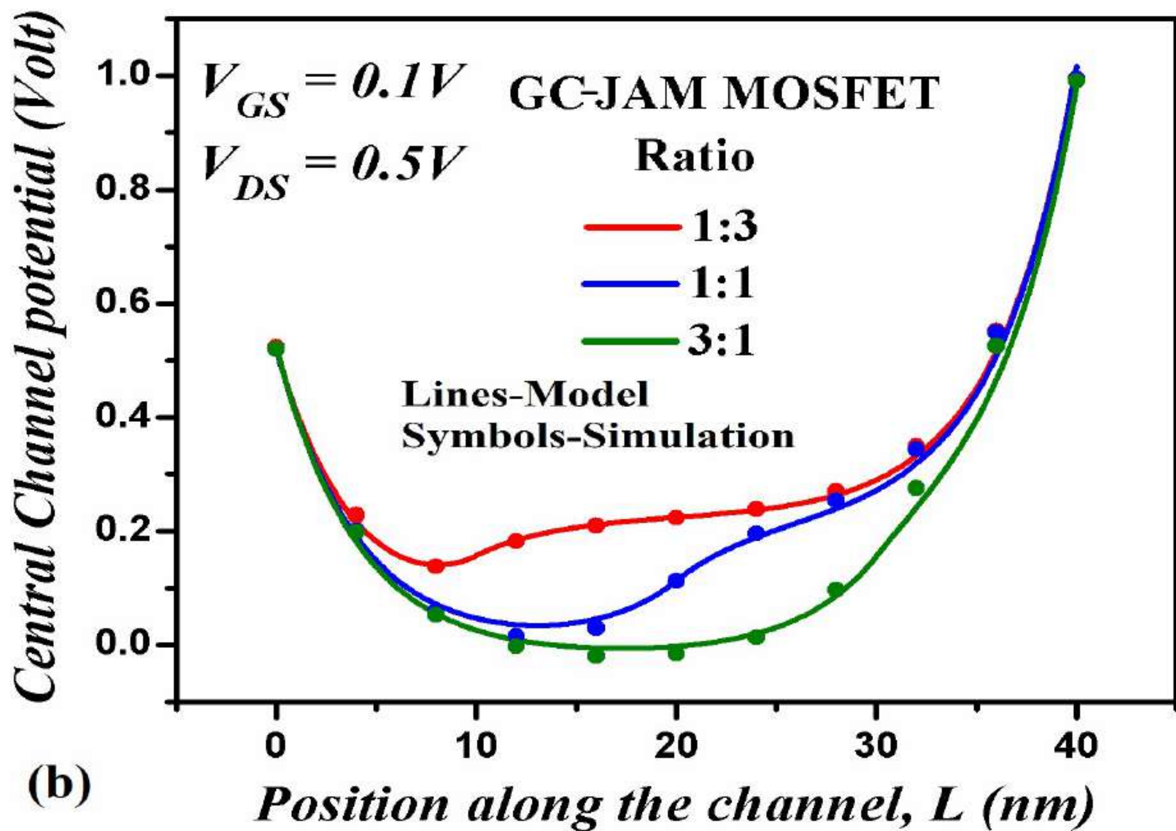

Fig. 3.7: Central channel potential along the channel length for different L_1:L_2 (a) L=40 nm, L=20 nm at V_{DS}=V_{GS}=0.1 V; (b) L=40 nm at V_{GS}=0.1 V, V_{DS}=0.5 V of GC-JAM MOSFET.

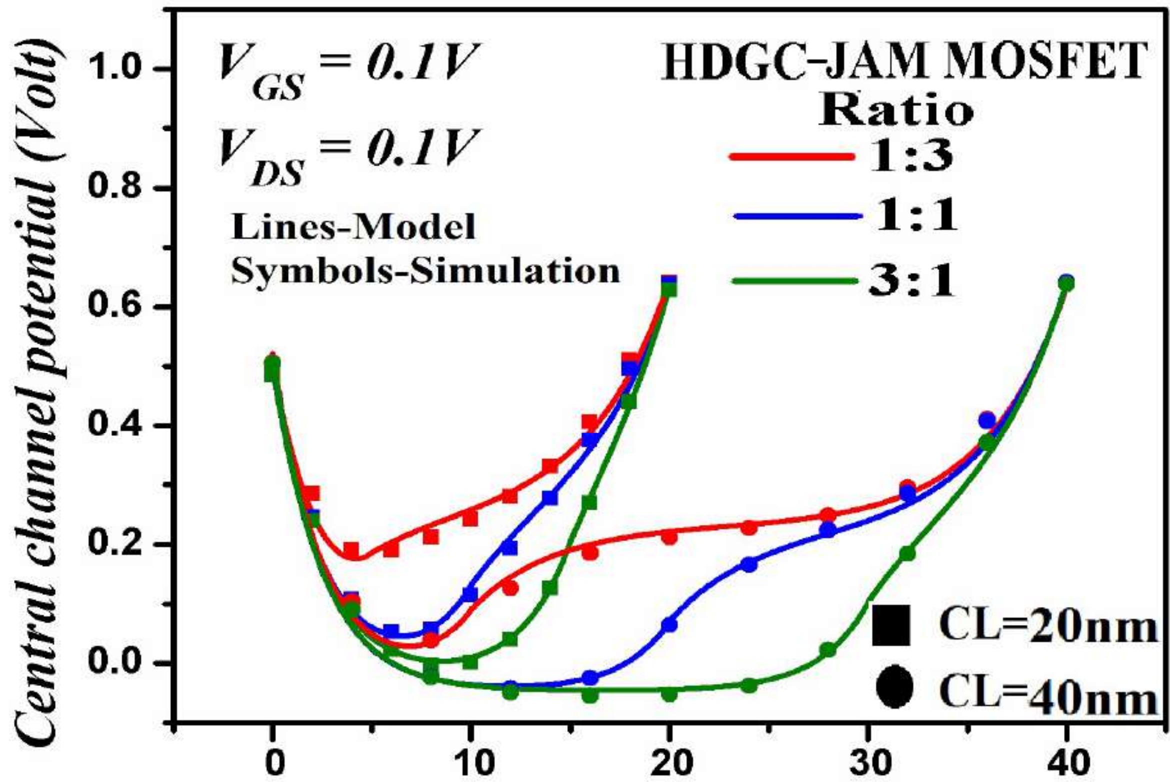

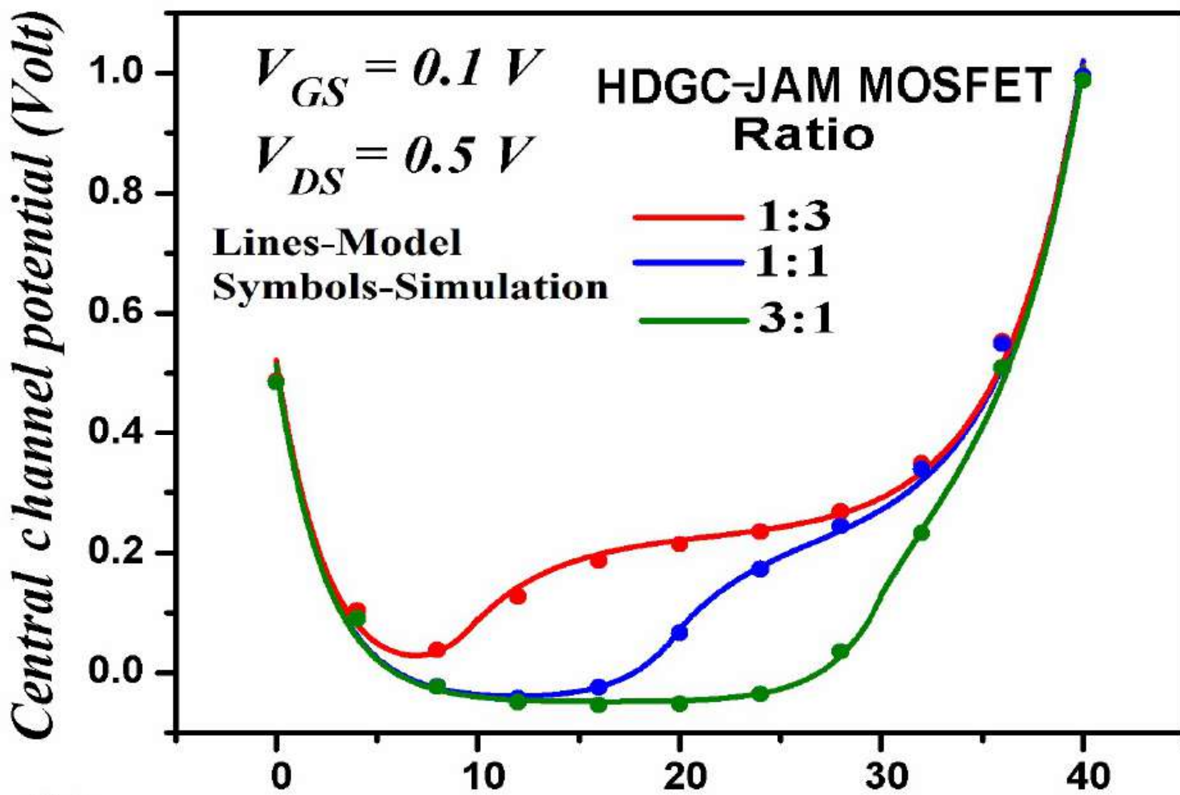

Fig. 3.8: Central channel potential along the channel length for L_1:L_2 (a) L=40 nm, L=20 nm at V_{DS}=V_{GS}=0.1 V; (b) L=40 nm at V_{GS}=0.1 V, V_{DS}=0.5 V, of HD-GC-JAM MOSFET.

electric field), It is observed that both GC-JAM and HD-GC-JAM MOSFETs have much lower electric fields than the uniformly doped JAM MOSFET at the drain end of the channel. This shows that GC-JAM and HD-GC-JAM MOSFETs have higher immunity to hot carrier effects (HCEs) and subthreshold leakage currents than the conventional JAM MOSFETs. However, the peak electric field of the GC-JAM and HD-GC-JAM MOSFETs at the middle of the channel ensures a higher average electric field in the channel to provide greater carrier transport efficiency than the JAM-MOSFETs (Mitra, Goswami and Bhowmick, 2016; Goel *et al.*, 2016). It may also be noted that the HD-GC-JAM structure has higher peak electric field near the source side than other two devices. This ensures a higher carrier transport efficiency in HD-GC-JAM MOSFET than the other two structures. Fig. 3.10 shows the lateral electric field variations with channel lengths for different L_1:L_2 ratios of GC-JAM and HD-GC-JAM MOSFETs respectively. The increased L_1:L_2 ratio shifts the peak of the electric field towards the drain side of the channel which implies larger effects of drain voltage on the performance of both the HD-GC-JAM and GC-JAM MOSFETs. Fig. 3.11 shows the variation of the threshold voltage and roll-off as a function of channel lengths for 0.1 V, 0.5 V and 1 V values of V_{DS}. The threshold voltage variability with channel length is the lowest for HD-GC-JAM MOSFET and the highest for JAM MOSFET. The higher threshold voltage of GC-JAM MOSFET can be attributed to lower accumulation than the conventional JAM MOSFET due to higher source-channel barrier resulted from the lower channel doping concentration at the source side. The highest threshold voltage in the HD-GC-JAM MOSFET among the three structures is attributed to the increased source-channel potential barrier due to high-*k* oxide near the source side. Fig. 3.12 compares the threshold voltage variations with channel lengths for different L_1:L_2 ratios (1:3, 1:1 and 3:1) of HD-GC-JAM MOSFET and GC-JAM MOSFET respectively. With the increase in L_1:L_2 ratio, the threshold voltage is increased due to the

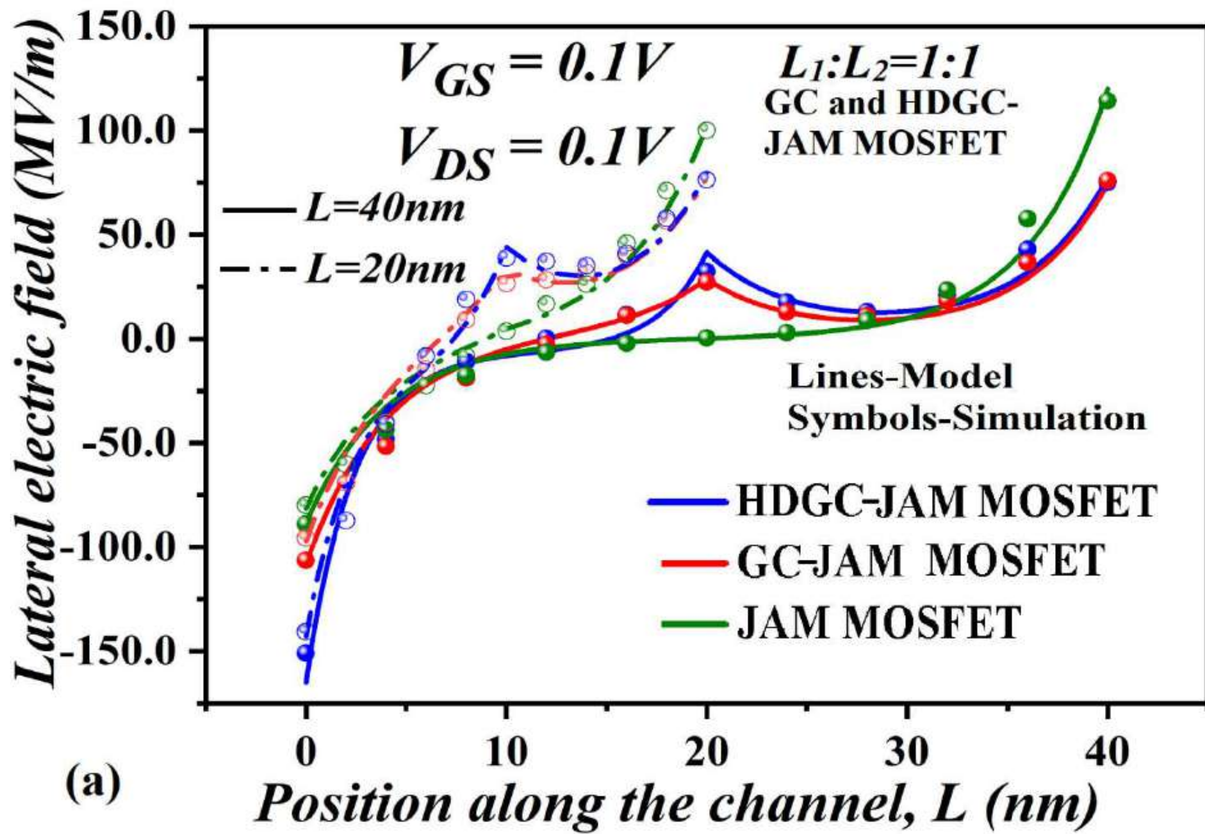

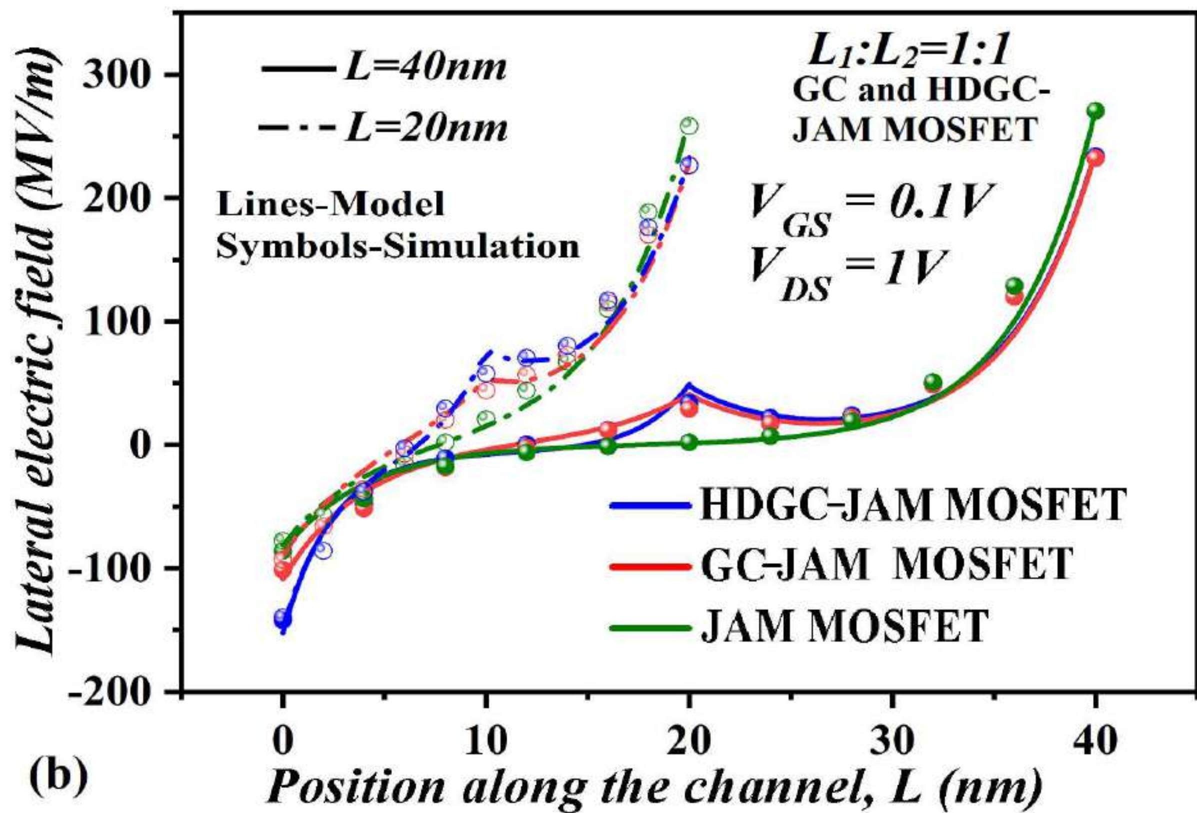

Fig. 3.9: Lateral electric field along the channel (V_{DS}=V_{GS}=0.1 V) for HD-GC-JAM, GC-JAM, and JAM MOSFETs, (*L=20 nm and 40 nm*) at (a) V_{DS}=0.1 V; (b) V_{DS}=1 V.

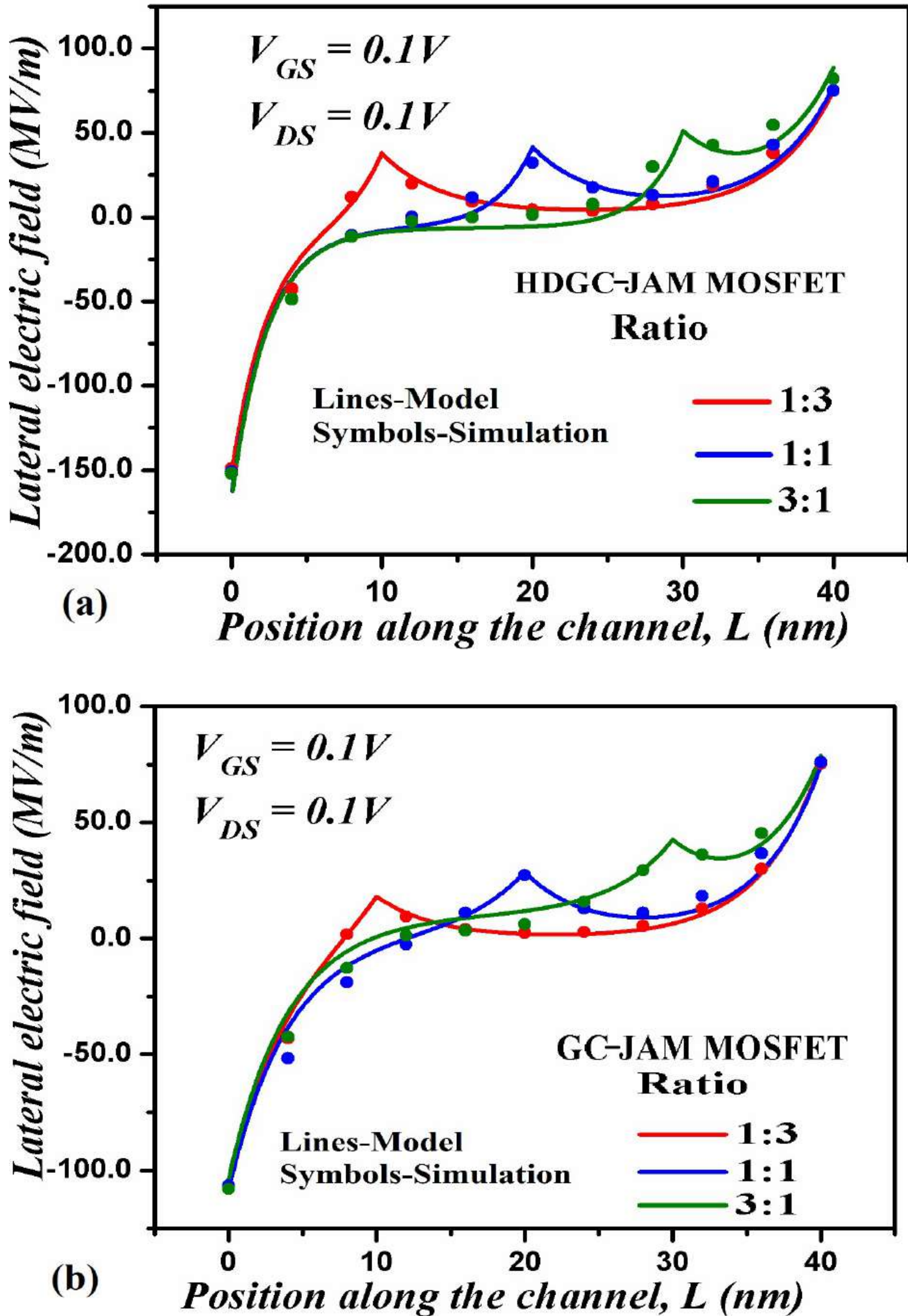

Fig. 3.10: Lateral electric field along the channel (V_{DS}=V_{GS}=0.1 V) with L_1:L_2 ratio (1:3, 1:1 and 3:1) for (a) HD-GC-JAM; (b) GC-JAM.

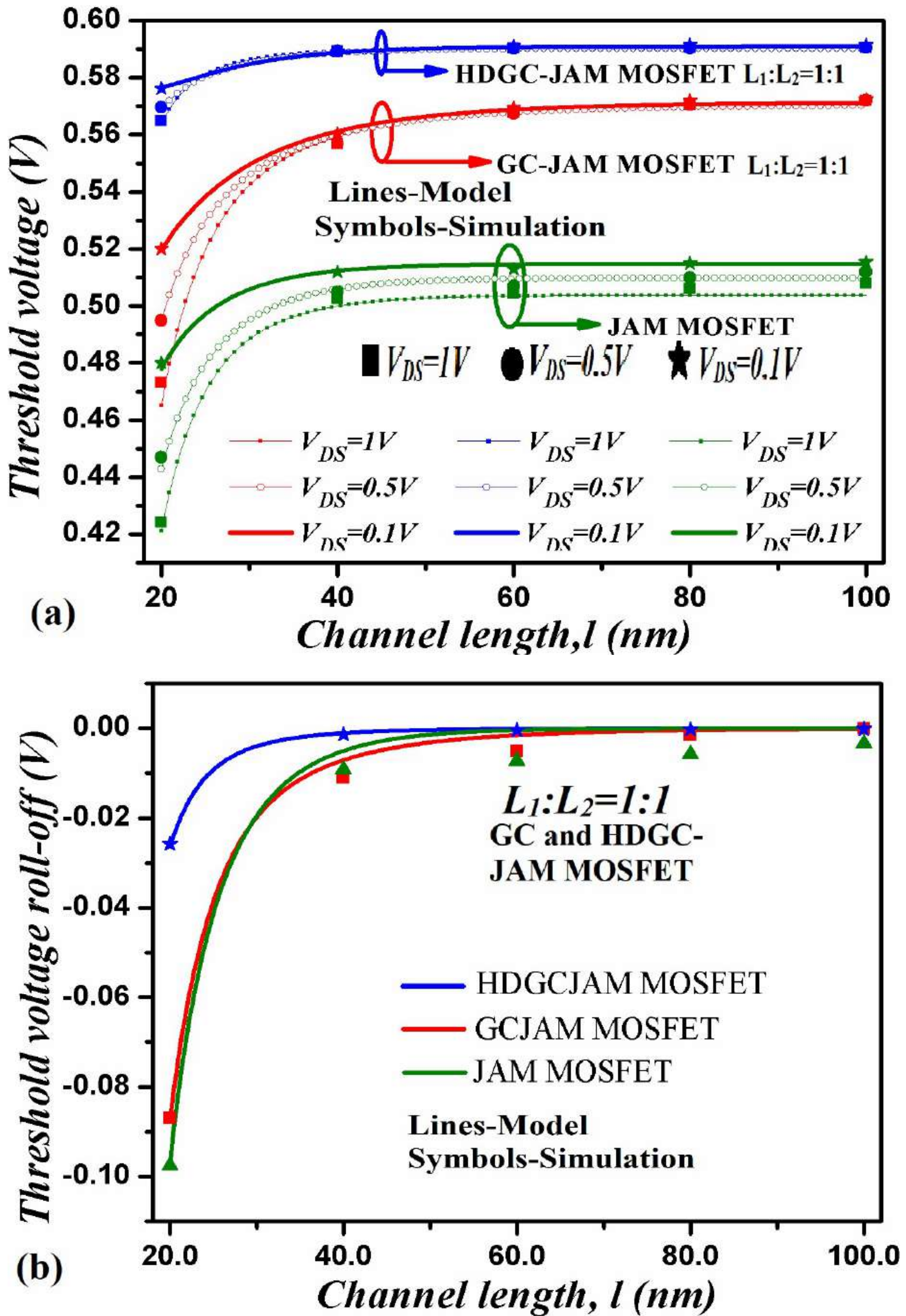

Fig. 3.11: (a) Threshold voltage variations with the variation of channel length, (V_{DS}=0.1 V, 0.5 V and 1 V); (b) roll-off for HD-GC-JAM, GC-JAM, and JAM MOSFETs.

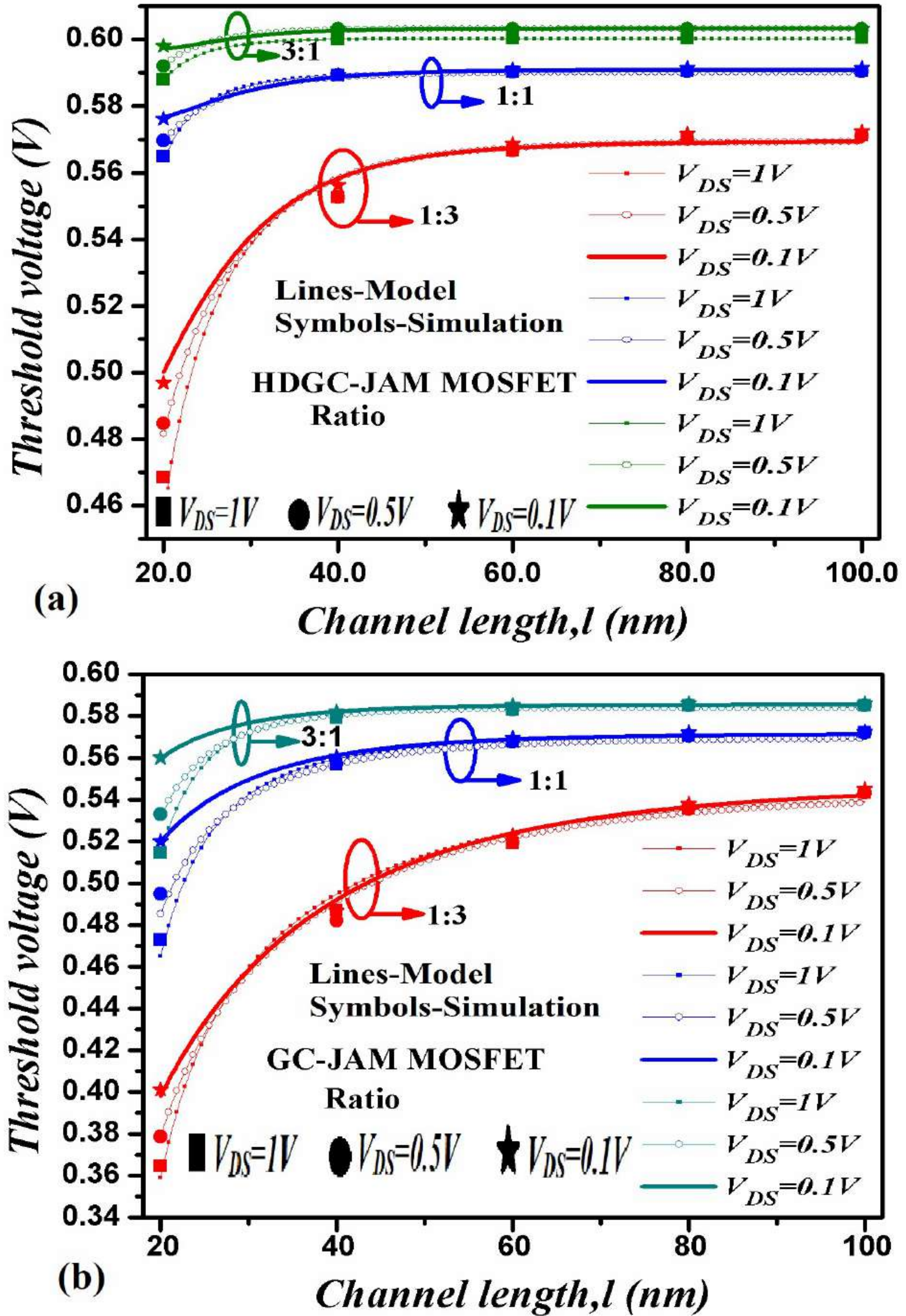

Fig. 3.12: Threshold voltage variations with variation of channel length, (V_{DS}=0.1 V, 0.5 V and 1 V) for (a) HD-GC-JAM; (b) GC-JAM, with L_1:L_2 ratio (1:3, 1:1 and 3:1).

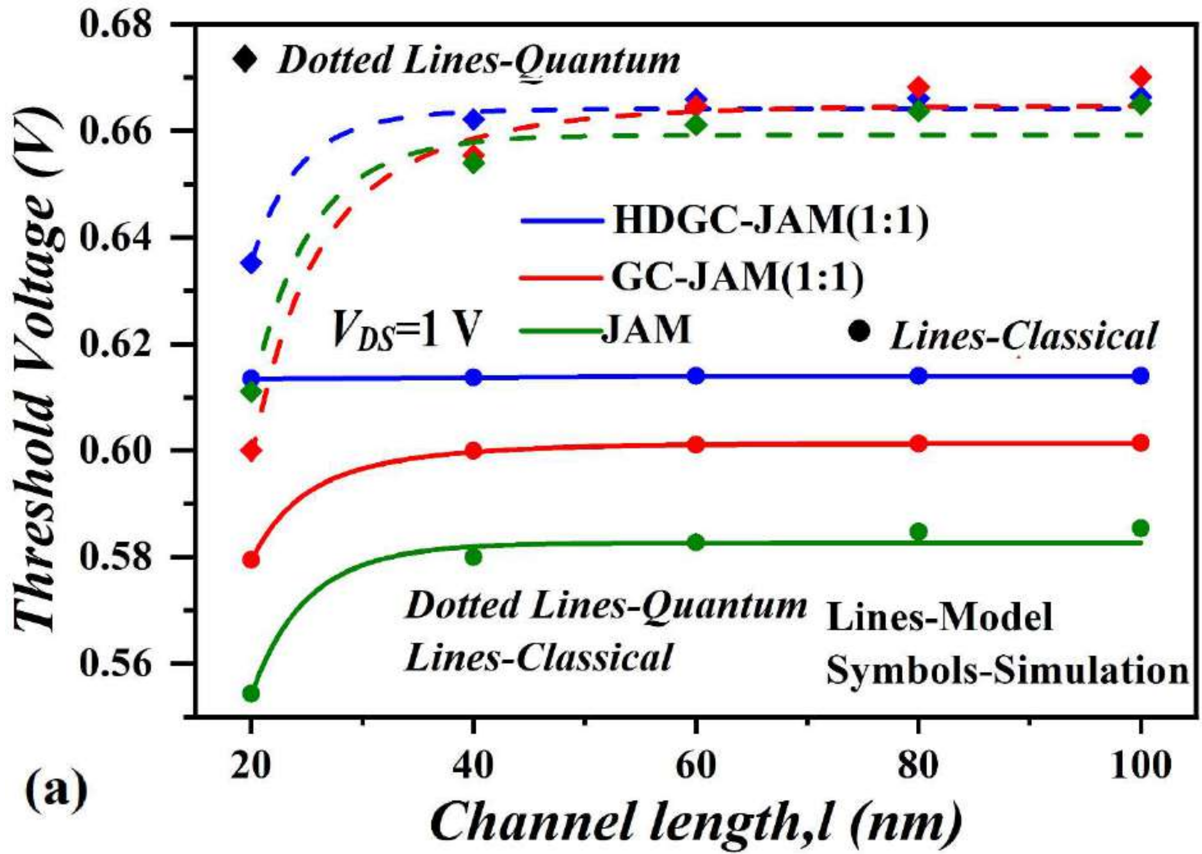

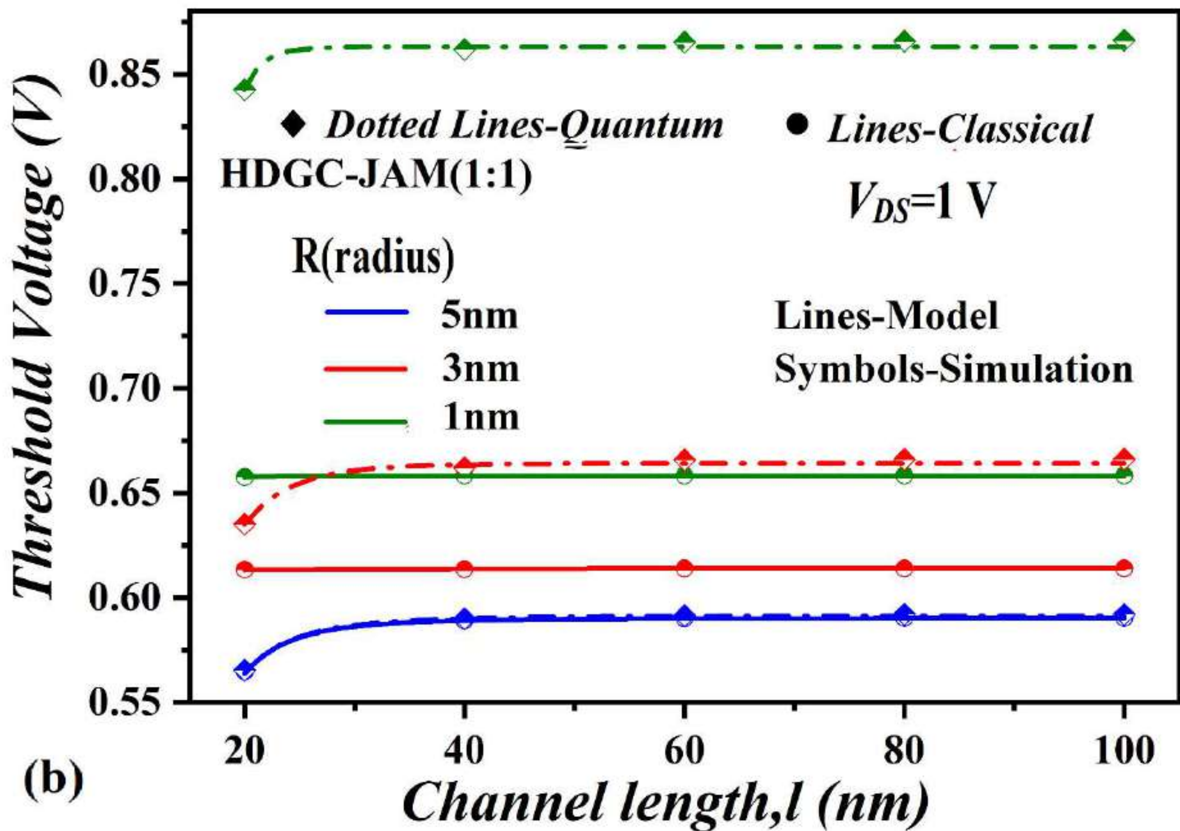

Fig. 3.13: Threshold voltage variation with channel length in QM and CL for (a) HD-GC-JAM, GC-JAM and JAM MOSFETs (R=3 nm); (b) HD-GC-JAM (L_1:L_2=1:1) for (R=1 nm, 3 nm, and 5 nm).

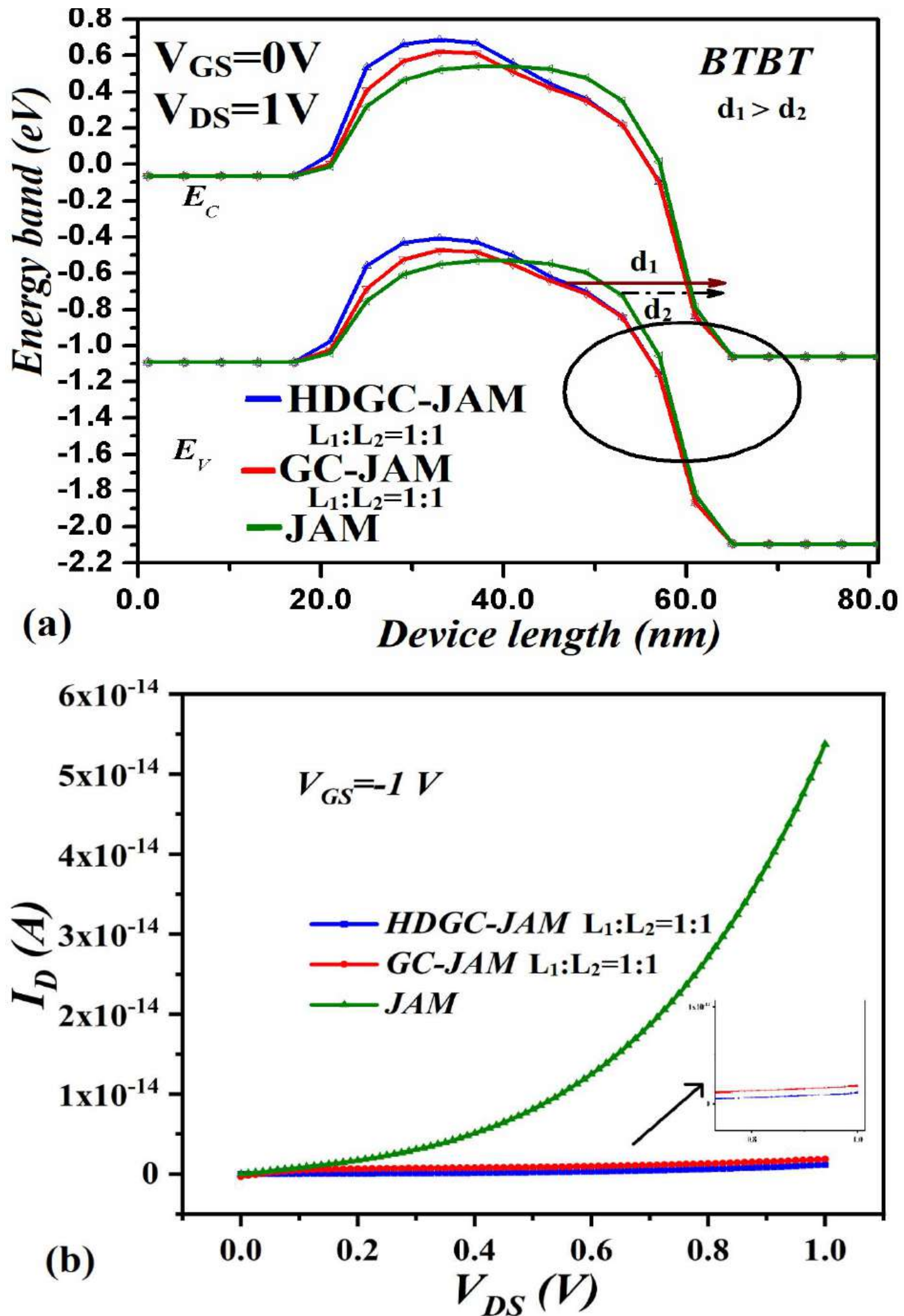

Fig. 3.14: (a) Simulated energy band diagram for all compared devices; (b) GIDL against drain voltage variations at (at V_{GS}=-1 V) for all devices considered for comparison in Table 3.1.

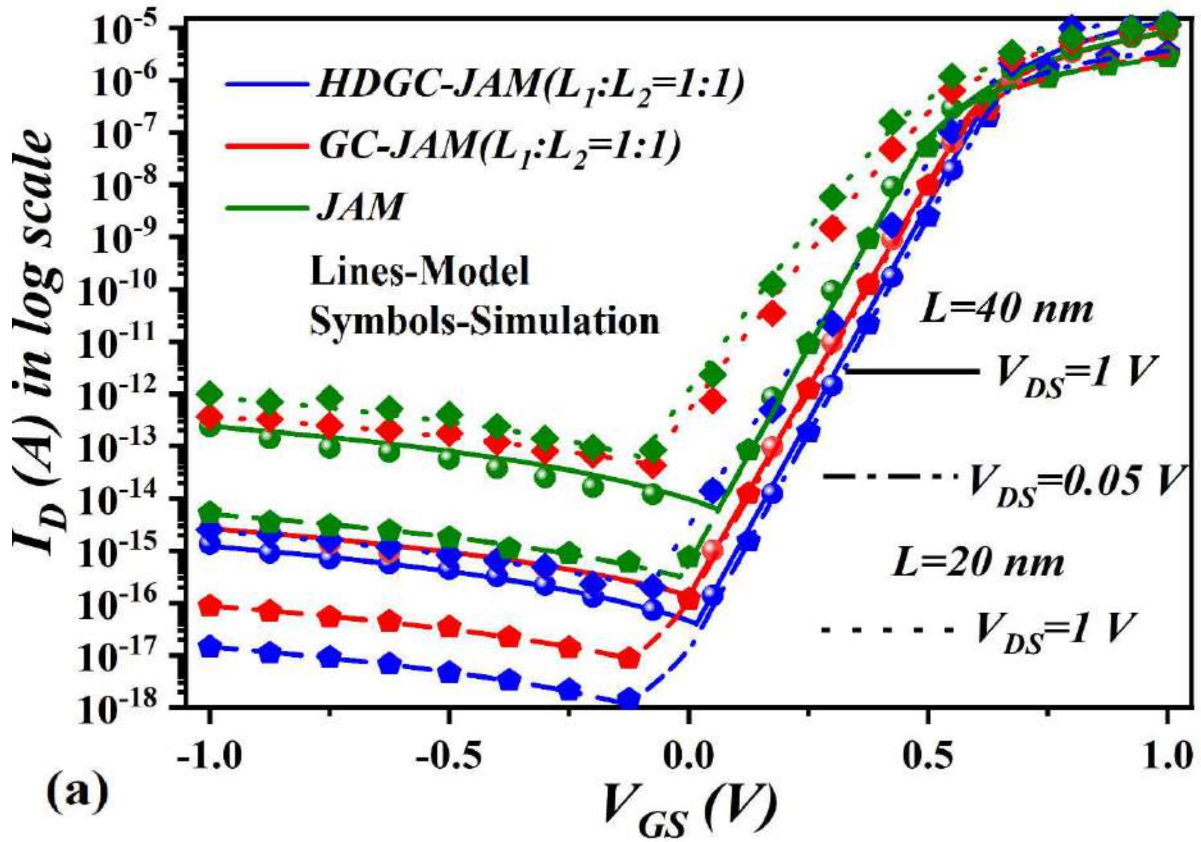

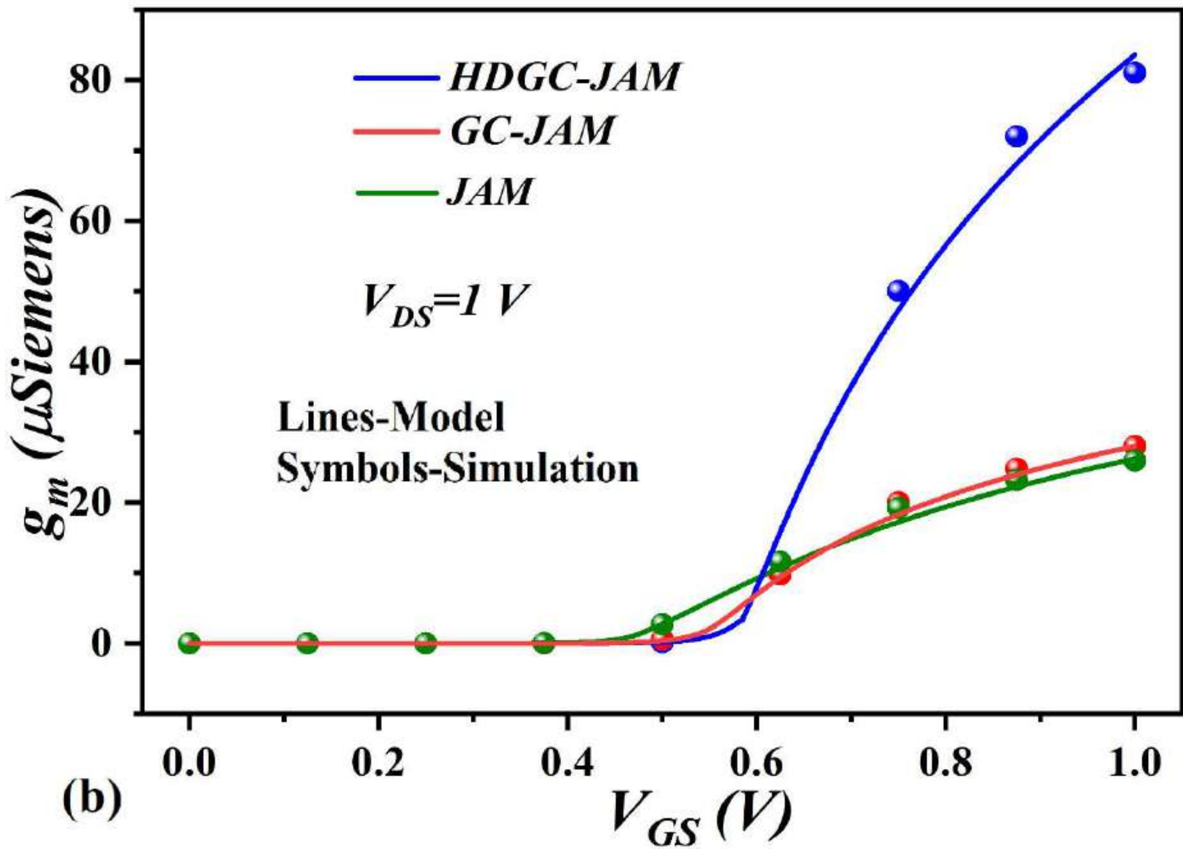

Fig. 3.15: (a) Drain current (logarithmic scale) considering GIDL against gate voltage variations at (V_{DS}=1 V, L=20 nm and V_{DS}=1 V, V_{DS}=0.05 V, L=40 nm); (b) g_m at V_{DS}=1 V; for all compared devices.

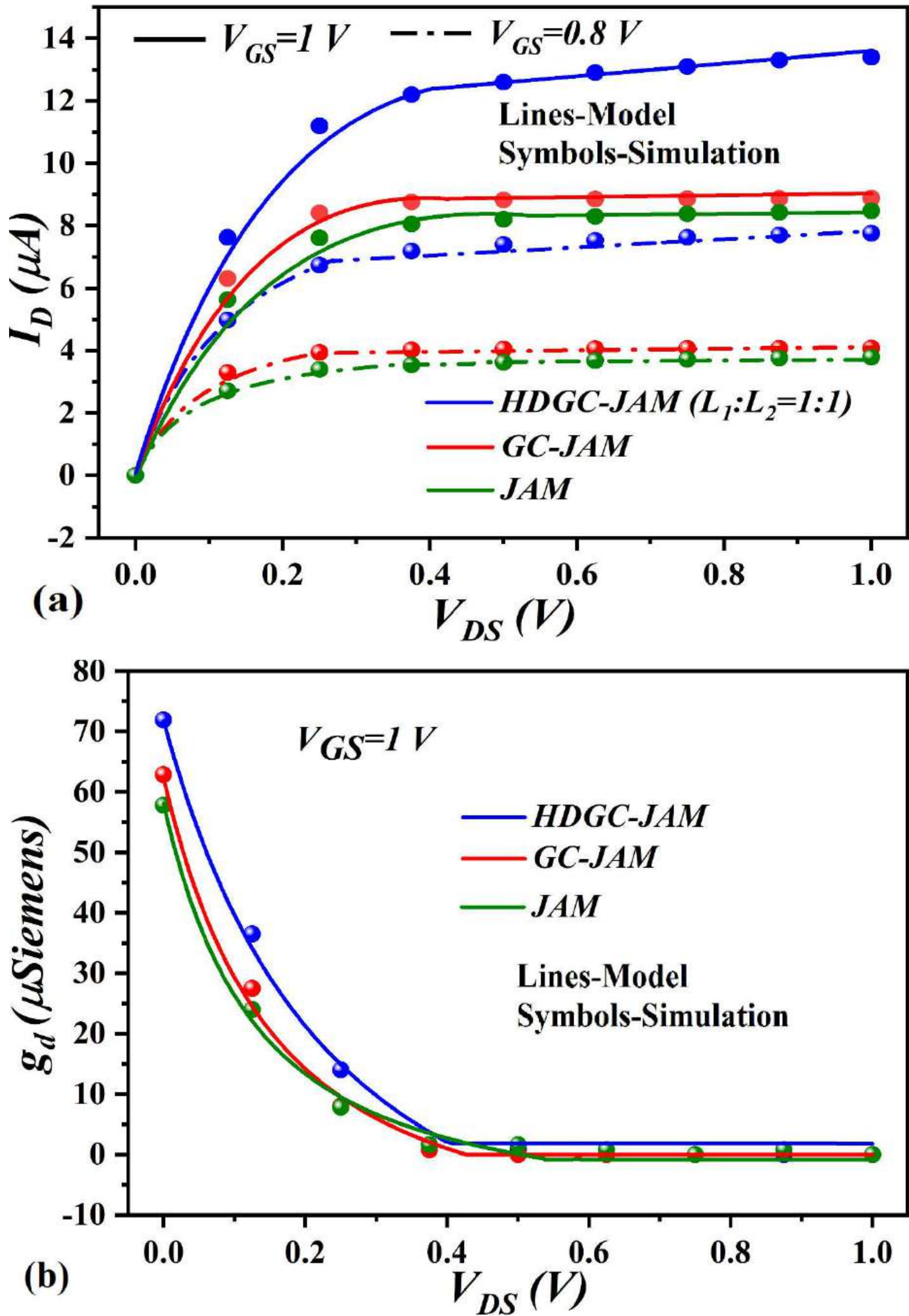

Fig. 3.16: (a) Drain current against drain voltage at V_{GS}=1 V, V_{GS}=0.8 V and L=40 nm; (b) g_d at V_{GS}=1 V; for all compared devices.

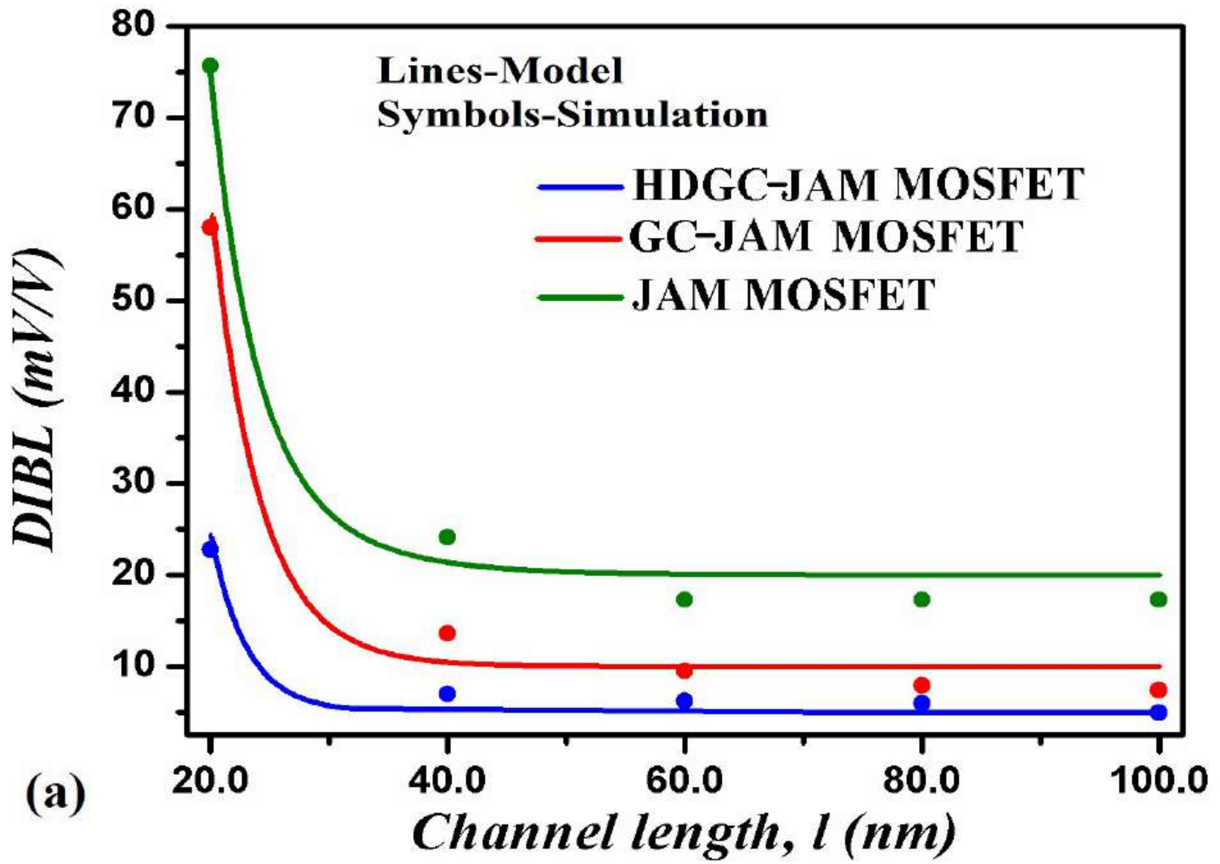

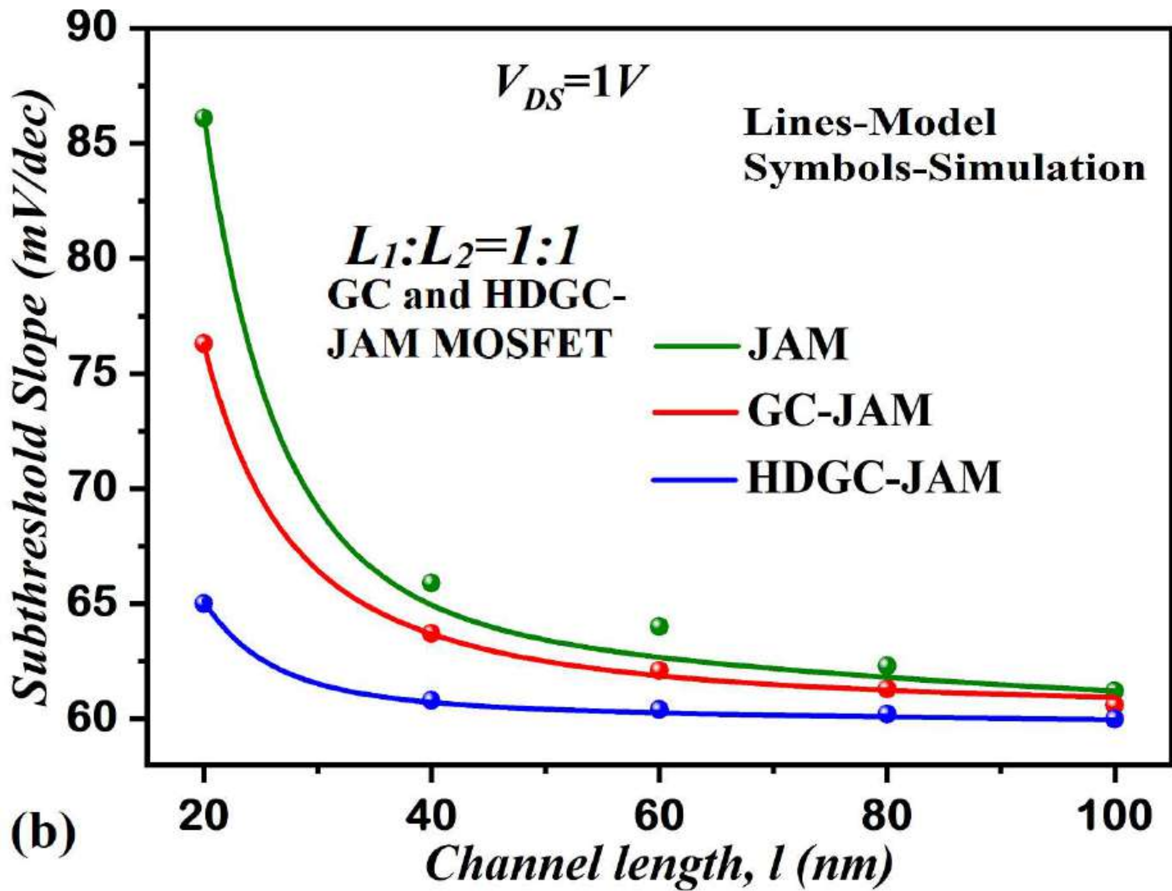

Fig. 3.17: (a) DIBL: (b) SS with variation in channel length for HD-GC-JAM, GC-JAM and JAM MOSFETs.

increase in the source-channel barrier. The larger source-to-channel barrier in the HD-GC-JAM MOSFET also results in smaller variation of the threshold voltage than the GC-JAM MOSFET. Fig. 3.13(a) compare the threshold voltage, (QM) and threshold voltage, (CL) of all three compared device structures (R=3 nm), it is seen that HD-GC-JAM has the least variability of threshold voltage considering QM confinement. In fig. 3.13 (b) threshold voltage QM and CL are compared for HD-GC-JAM (L_1:L_2=1:1) for (R=1, 3 and 5 nm), it could be observed that at a channel radius of 5 nm there is negligible change in QM and CL threshold voltage, this difference increase as the channel radius is reduced below 5 nm (Wang, 2006; Tsormpatzoglou *et al.*, 2009). Fig. 3.14(a) shows the energy band diagrams of all the three MOS structures under study. It is observed that the lateral BTBT width is the maximum in HD-GC-JAM MOSFET, which implies the smallest BTBT current (*i.e.,* the smallest GIDL) at negative gate voltage. Fig 3.14(b) shows simulated GIDL current against drain voltage at a negative gate voltage of V_{GS}=1 V. It could be observed that GIDL leakage is highest for JAM followed by GC-JAM and HD-GC-JAM MOSFET respectively. Fig. 3.15(a) shows drain current variations against V_{GS} at various channel length (L=40 nm, 20 nm) and at different V_{DS} (V_{DS}=1 V, V_{DS}=0.05 V). It could be observed that both GIDL leakage current and I_{OFF} are minimum for HD-GC-JAM MOSFET, further it could also be observed that both I_{ON} and I_{ON}/I_{OFF} ratio are also best for the same device. It is to be noted that for memory application V_{GS}=-V_{DD}=-1 V is a critical point, since lower leakage current at this point is better for information retention for the memory device. Thus, our proposed HD-GC-JAM MOSFET is best in this aspect. Fig. 3.15(b) demonstrates transconductance g_m for all the proposed devices. It could be seen that g_m for HD-GC-JAM is highest which attests its better analog performance. Fig. 3.16(a) shows I_D against V_{DS} for different V_{GS} (1 V, 0.8V). Fig. 3.16(b) shows g_d for V_{GS}=1 V. It could be observed that both the drain current I_D and output conductance g_d are best for HD-GC-JAM MOSFET. Fig. 3.17 compares the DIBL and SS variations for different channel lengths of all

the three JAM structures respectively. DIBL is a prominent effect found in short channel devices, which manifests itself as the change in threshold voltage with the change in drain voltage (V_{DS}). The minimum value of DIBL can be found for HD-GC-JAM MOSFET which can also be corroborated from Fig. 3.11(a). Device corresponding to lower SS value indicates faster transition between off and on state and therefore, has more power efficiency. A lower value of SS in the HD-GC-JAM MOSFET confirms its superior performance over the other two devices under comparison. Similarly, the smaller values DIBL and SS parameters in GC-JAM MOSFET ensures that the device has better performance than the conventional JAM MOSFET.

3.4 Conclusion

A 2-D analytical model of the surface potential, lateral electric field, threshold voltage, roll-off, DIBL, total drain current with GIDL and SS for short-channel ultrathin nanowire halo doped HD-GC-JAM has been reported in this chapter. The superiority of the device has been shown by comparing the results with the cylindrical GC-JAM and JAM MOS structures. The dependence of various device electrical characteristics on the channel length, drain voltage (V_{DS}), and control gate length to screening gate length ratio (i.e., L_1:L_2 ratio) has been studied in details. It has been shown that the proposed HD-GC-JAM MOSFET gives the best performance in terms of SCEs, drain voltage variations, roll-off, DIBL, HCEs, GIDL and I_{ON} among the three JAM structures under comparison. In addition, QM corrections for threshold voltage at ($R<5$ nm) have also been included in this work. It is shown that difference between CL and QM threshold voltages increases with the decrease in R. The proposed model has been validated by comparing the model results with the simulation data obtained by using the commercially available COGENDA^{TM} 3-D Visual TCAD.

A 2-D Compact DC Model for Engineered CG- JAM-MOSFETs Valid for All Operating Regimes

4.1 Introduction

We have observed in Chapter-2 and Chapter-3 that graded channel engineering (Goel *et al.*, 2016a; Banerjee and Sarkar, 2019), dual-material (DM) engineering and laterally stacked HfO_2/SiO_2 gate-oxide structure (Pratap *et al.*, 2014a) can improve the drive current, reduce the GIDL and gate leakage currents, and reduces the SCEs and HCEs of the JAM MOSFETs. However, we have considered only the depletion charges in the 2D Poisson equation in the previous two chapters and hence they are not valid for the accumulation/inversion regime of operation of the JAM MOSFETs. In fact, most of the 2-D compact models reported in the literature are valid either for only depletion regime (i.e., by considering only depletion charges) (Li *et al.*, 2014; Pratap *et al.*, 2014a; Goel *et al.*, 2016a; Trivedi, Kumar, Haldar, S. S. Deswal, *et al.*, 2016; Banerjee and Sarkar, 2019) or only for accumulation/inversion regime (i.e., by considering only free mobile charges) (El Hamid, Iñíguez and Roig Guitart, 2007; Ray and Mahapatra, 2008) of operation as summarized in table 4.1. A compact model is an analytical set of equations and works much faster than numerical simulators. Thus, a comprehensive 2-D compact analytical DC model for the engineered JAM MOSFETs could be of interest to the researchers. Therefore, the present chapter considers the development of a continuous 2-D potential based DC compact model for the short channel stacked hetero-dielectric (SHD) graded channel (GC) dual-material (DM) JAM MOSFET (SHD-GC-DM-JAM) by considering both the depletion and doped (accumulation) charges.

TABLE 4.1: Comparison of different 2-D models

Model support and operation / ***Comparison of various models***	***Accumulation/ inversion region***	***Depletion region***	***Device engineering***
Ref: (Trivedi, Kumar, Haldar, S. S. Deswal, et al., 2016)	No	Yes	No
Ref: (Li et al., 2014; Pratap et al., 2014a; Goel et al., 2016a; Banerjee and Sarkar, 2019)	No	Yes	Yes
Ref: (El Hamid, Iñíguez and Roig Guitart, 2007; Ray and Mahapatra, 2008)	Yes	No	No
Our Model	Yes	Yes	Yes

Section 4.2 presents the proposed 2-D analytical continuous model for the CG SHD-GC-DM JAM MOSFET. Models for the threshold voltage and complete drain current (including GIDL) have been developed for the JL/JAM MOSFET. Various electrical characteristics such as roll-off, DIBL, and SS have also been modeled. Further, interface trapped charges, mobility and bandgap variation with temperature and quantum confinement effects for channel radius

(R) below 5 nm have also been considered in the proposed model. Some important results obtained and related discussions have been presented in Sec. 4.3. Sec. 4.4 describes the simulation setup for 3-D TCAD. Finally, Sec. 4.5 concludes the present chapter.

4.2 Analytical model formulation

Fig. 4.1 depicts 2-D cross-section of CG-SHD-GC-DM-JAM nanowire MOSFET. Here $L=L_1+L_2$, where L_1 and L_2 are the lengths of control and screen gate represented by region Region-1 (R_1) and Region-2 (R_2) respectively. The entire channel region is wrapped by 1 nm of SiO_2 followed by vertical stacking of 2 nm layer of horizontally stacked high-k and low-k over region R1 and R2 respectively. Gate material with work-function φ_{m1} and φ_{m2} is deposited over region R_1 and R_2, where $\varphi_{m1}>\varphi_{m2}$. Further, the channel has graded doping with N_1 in R_1 and N_2 in R_2, where $N_2>N_1$. The channel is assumed to be fully depleted under zero bias condition, the extension of the depletion region in source and drain have been considered negligible as the doping is high compared to that of the channel ($N_{S/D}=10^{20} >> N_1$ and N_2), structural and electrical quantum confinement effects have been considered for channel radius below 5 nm (Omura *et al.*, 1993), oxide interface trapped charges of $N_f=10^{12}$ cm^{-2} has been considered at oxide interface above R_2 (Pratap *et al.*, 2015; Kumar *et al.*, 2016) and effective mobility and bandgap change with temperature have also been accounted for in the proposed model. The proposed device could be fabricated by using an extra halo implant step for the graded channel (Vasi *et al.*, 2002). As for the stacked hetero-dielectric ALD could be used for HfO_2 deposition over SiO_2 followed by selective wet etching by HF for the formation of vacuum dielectric in place of HfO_2 (Lowalekar and Raghavan, 2004). It should be noted that the same mask used for halo doping could be used for wet etching. Dual work function material could be formed by passing nitrogen over Molybdenum (Lin *et al.*, 2002). A

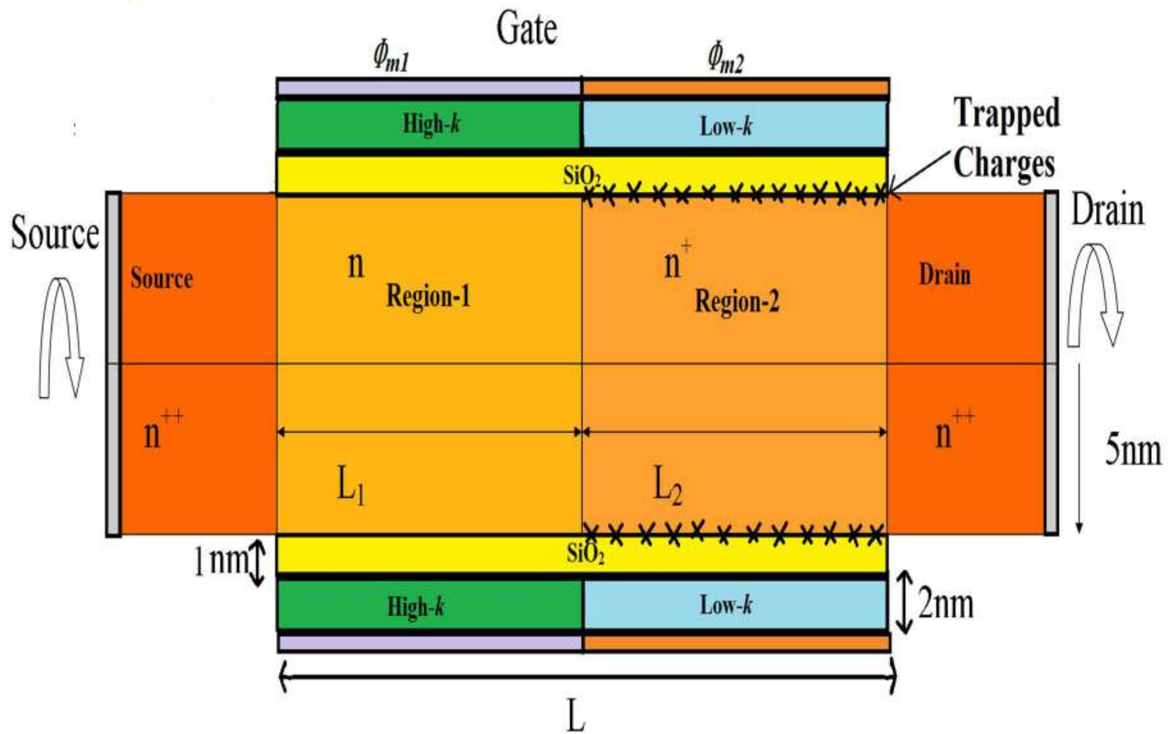

Fig. 4.1: A 2-D cross-sectional view of CG-SHD-GC-DM-JAM MOSFET.

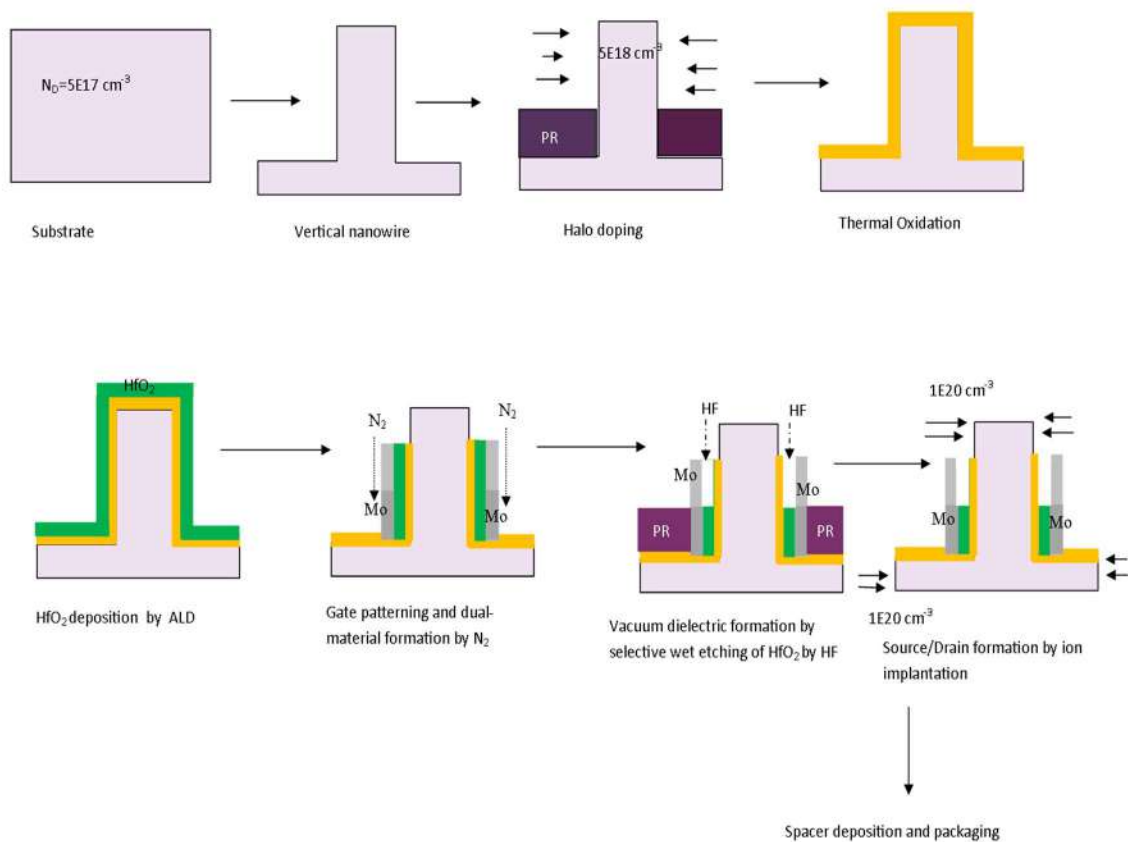

Fig. 4.2: A schematic of SHD-GC-DM-JAM MOSFET fabrication steps.

schematic of vertical CG HDGCDM JAM MOSFET fabrication process flow is shown in fig. 4.2.

4.2.1 Modeling of device potential

Potential inside a CG device is invariable with θ. Let the potential be $\psi_1(r,z)$ and $\psi_2(r,z)$ in region R_1 and R_2 with length L_1 and L_2 at doping of N_1 and N_2 respectively. Thus, the 2-D potential distribution $\Psi_i(r,z)$ in the channel region R_i (i=1, 2) can be obtained by solving the following Poisson's equations:

$$\frac{d^2\psi_i(r,z)}{dz^2}+\frac{1}{r}\frac{d}{dr}r\frac{d\psi_i(r,z)}{dr}=-\frac{qN_i}{\varepsilon_{Si}}\left[1-exp\left[\frac{\psi_i(r,z)-V_{f,i}}{V_T}\right]\right] for \text{ JAM}$$

$$\frac{qN_i}{\varepsilon_{Si}}\left[1-\left(\frac{ni}{N_i}\right)^2 exp\left[\frac{\psi_i(r,z)-V_{f,i}}{V_T}\right]\right] for \text{ MOSFET} \tag{4.1}$$

where V_T is the thermal voltage of 25.9 mV and $V_{f,i}$ is the quasi-fermi level for the region given by$V_{f,i}=V_T\, ln\left({N_i}/{ni}\right)$where $ni$is the intrinsic carrier concentration (Liu and Li, 2012). Appling superposition technique to solve the Poisson's equation of (4.1) for (JAM) by separating them into 1-D Poison's equation, $\phi_i(r)$ and 2-D Laplace equation, $v_i(r,z)$ and can be expressed as (El Hamid, Iñíguez and Roig Guitart, 2007; Yu *et al.*, 2007a; Ray and Mahapatra, 2008a; Cho *et al.*, 2008; Jin *et al.*, 2013; Jazaeri, Barbut and Sallese, 2014; Li *et al.*, 2014; Goel *et al.*, 2016a; Trivedi, Kumar, Haldar, S. S. Deswal, *et al.*, 2016; Banerjee and Sarkar, 2019):

$$\psi_i(r,z)=v_i(r,z)+\phi_i(r) \tag{4.2}$$

$$\frac{1}{r}\frac{d}{dr}r\frac{d\phi_i(r)}{dr}=-\frac{qN_i}{\varepsilon_{Si}}\left[1-exp\left[\frac{\phi_i(r,z)-V_{f,i}}{V_T}\right]\right] \tag{4.3}$$

$$\frac{d^2v_i(r,z)}{dz^2}+\frac{1}{r}\frac{d}{dr}r\frac{dv_i(r,z)}{dr}=0 \tag{4.4}$$

4.2.1.1 Effect of band gap narrowing and device temperature

In general, the bandgap in Si starts narrowing for a doping concentration above 10^{17} cm^{-3} (Pratap *et al.*, 2015; Trivedi, Kumar, Haldar, S. S. Deswal, *et al.*, 2016). Device temperature also affects the bandgap of the semiconductor (Pratap *et al.*, 2015). Since the channel doping considered here is >10^{17} cm^{-3} the effect of these should be considered for improving the accuracy of the model. Thus, these two effects have been incorporated into our present model in terms of the following equations:

$$\Delta E_{g,i} = \beta_E\left(ln(N_i/\beta_N) + \sqrt{ln(N_i/\beta_N)^2 + \beta_C}\right) \tag{4.5}$$

$$E_{g,i}^{eff}{}_{CL} = E_g - \Delta E_{g,i} + E_{g\alpha}\left(\frac{300}{300 \quad g\beta} - \frac{T^2}{T+E_{g\beta}}\right) \tag{4.6}$$

$$\chi_i^{eff} = \chi + \Delta E_{g,i}/2 \tag{4.7}$$

where, $\beta_E = 6.92 \times 10^{-3}$eV, $\beta_N = 1.3 \times 10^{17}$cm^{-3}and $\beta_C = 0.5$ are some empirical constants at room temperature; $E_{g\alpha}$=4.63×10-4 eV/K, $E_{g\beta}$=636 K, E_g and $\chi$are the energy bandgap and electron affinity, $E_{g,i}^{eff}{}_{CL}$ and $\chi_i^{eff}$are the effective energy bandgap for classical modeling and electron affinity of the channel material after incorporating the above model in R_1 and R_2 regions respectively (Pratap *et al.*, 2015; Trivedi, Kumar, Haldar, S. S. Deswal, *et al.*, 2016).

4.2.1.2 Effect of structural and electrical quantum confinement

The effects of quantum and electrical confinements should be considered while considering the channel radius below 5 nm. In the subthreshold region with negligible mobile charges, the Poisson-Schrödinger could be solved in a decoupled manner. Further, considering the quantum confinement in the transverse direction we could write as (Wang, 2006; Dura *et al.*, 2011):

$$-\frac{\hbar^2}{2m_e}\left[\frac{d^2}{dr^2} + \frac{1}{r^2}\frac{d}{dr} + \frac{1}{r^2}\frac{d^2}{d\theta^2}\right]\lambda(r,\theta) + (U-E)\lambda(r,\theta) = 0 \tag{4.8}$$

where, m_e is the effective carrier mass; $\lambda(r, \theta)$ is the wave function; E is the discretized energy of the conduction band and $\left(\hbar = \frac{h}{2\pi}\right)$ is the modified Plank's constant, and $U(r, \theta)$ is the cylindrical potential well defined as:

$U(r,\theta) = \begin{cases} U, 0 < r < R \\ \infty, Otherwise \end{cases}$ where U is the potential at the bottom of the well and represent the minima of the conduction band as (Kumar and Tiwari, 2018).

Using the separation of variables method, the solution of (8) could be written as (Dura *et al.*, 2011; Kumar and Tiwari, 2018):

$$\lambda(r,\theta) = C_1 J_l\left(\kappa_{l,n}\frac{r}{R}\right) \quad (4.9)$$

where, $C_1 = \frac{1}{\int_0^{2\pi} d\theta \int_0^R r|\lambda(r,\theta)|^2 dr}$, l and n are the angular and radial quantum number, respectively; $\kappa_{l,n}$ is the nth zero of the lth order Bessel's function; $\kappa_{l,n}$ can be found by following boundary condition (Kumar and Tiwari, 2018):

$$\lambda(R,\theta) = 0 \quad (4.10)$$

Further, each electron corresponds to six different ellipsoidal surfaces of constant energy with an effective mass of m_l=0.97m_0 and m_t=0.19m_0 along the longitudinal and transverse direction, where m_0=9.1x10^{-31} Kg is mass of the free electron. The confinement mass of electron in transverse valleys could be approximated as cylindrical mass $m_c = \frac{2m_t m_l}{m_t + m_l} = 0.315m_0$ and for longitudinal valleys as m_t=0.19m_0 (Dura *et al.*, 2011). Due to quantum confinement, the continuous energy band takes discrete values and there is a widening of bandgap given as (Chiang and Liou, 2013):

$$\Delta E_c = \frac{\hbar^2 \kappa^2{}_{l,n}}{2R^2 m_e} \quad (4.11)$$

where $\frac{1}{m_e} = \frac{1}{m_c} + \frac{1}{m_t}$ applying this quantum correction factor and accounting for bandgap widening [25]:

$$E_{g,i}^{eff}{}_{QM} = E_{g,i}^{eff}{}_{CL} + \Delta E_c + \gamma(N_i)\left(\frac{\varepsilon_{si}}{4qkT}\right)^{1/3}(E_S)^{0.63} + \sigma(N_i) \quad (4.12)$$

where, $\gamma(N_i) = 8.45 \times 10^{-8}/\left(1 + \frac{N_i}{2\times10^{19}}\right)$ and $\sigma(N_i)$ varies logarithmically from 10 meV to 0 eV for doping of 10^{18} to 10^{19} as given in (Hareland *et al.*, 1998). $E_S$is given as (Trevisoli *et al.*, 2012).

4.2.1.3 Solving 1-D Poisson's equation

The 1-D (i.e., long channel) potential $\phi_i(r)$ can be obtained by solving Eq. 3. The solution of which can be given as (Yu *et al.*, 2007a; Cho *et al.*, 2008; Jin *et al.*, 2013; Jazaeri, Barbut and Sallese, 2014). The 1-D potential can be further divided into three parts constant central, variable depletion and variable accumulation as (Cho *et al.*, 2008; Jin *et al.*, 2013)

$$\phi_i(r) = \phi_{C,i} + \phi_{D,i}(r) + \phi_{A,i}(r) \quad (4.13)$$

Boundary conditions to solve Eq. 3 are:

$$\phi_{D,i}(r)\Big|_{r=0} = 0,\ \varepsilon_{Si}\frac{d\phi_{D,i}(r)}{dr}\Big|_{r=0} = 0 \quad (4.14)$$

$$\phi_{A,i}(r)\Big|_{r=0} = 0,\ \varepsilon_{Si}\frac{d\phi_{A,i}(r)}{dr}\Big|_{r=0} = 0 \quad (4.15)$$

Let t_{ox11} and t_{ox12} be the thickness of SiO_2 and horizontally stacked high-*k*/low-*k* layer respectively. While ε_{ox}, $\varepsilon_{ox,1}$, $\varepsilon_{ox,2}$ be the dielectric constants of SiO_2, high-*k* and low-*k* layer respectively.

$$C_{ox,i}(V_{GS} - V_{fb,i} - \phi_i(r))\Big|_{r=R} = \varepsilon_{Si}\left(\frac{d\phi_i(r)}{dr}\right)\Big|_{r=R} \quad (4.16)$$

where $C_{ox,i} = \varepsilon_{ox}/t_{ox,i'}$, $t_{ox,i'} = R\,ln\left(1 + t_{ox,i}/R\right)$,$t_{ox,1} = {}^{\varepsilon_{ox} t_{ox12}}/_{\varepsilon_{ox,1}} + t_{ox11}$ and

$t_{ox,2} = {}^{\varepsilon_{ox} t_{ox12}}/_{\varepsilon_{ox,2}} + t_{ox11}$

$$V_{fb,1} = \varphi_{m1} - \varphi_{s1} \text{ and } V_{fb,2} = \varphi_{m2} - \varphi_{s2} \pm \frac{qN_f}{C_{ox,2}} \quad (4.17)$$

$$\varphi_{s,i} = \chi_i^{eff} + E_{g,i}^{eff}{}_{CL/QM}/2q - V_{f,i} \quad (4.18)$$

Since the region near drain has a high electric field density, hot-carrier induced damage may create trap charges in that region. Consequently, the oxide/channel interface trap charge density is assumed to be a step profile centered at the middle of the channel with 0 at R_1 and N_f at the interface of R_2 (Pratap *et al.*, 2015; Kumar *et al.*, 2016).

Depletion potential can be given as:

$$\phi_{D,i}(r) = \frac{-qN_i r^2}{4\varepsilon_{Si}} \quad (4.19)$$

Accumulation potential can be expressed as (Ray and Mahapatra, 2008)

$$\phi_{A,i} = -2V_T\,ln\left[1 - \frac{\delta_i r^2}{8} exp\left({}^{\phi_{C,i} - V_{f,i}}/_{V_T}\right)\right] \quad (4.20)$$

where, $\delta_i = \frac{qN_i}{\varepsilon_{Si} V_T}$

now combining Eq. 19 and 20 we get:

$$\phi_i(r) = V_{f,i} - \frac{qN_i r^2}{4\varepsilon_{Si}} + V_T\,ln\left[\frac{-8B_i}{\delta(1+B_i r^2)}\right] \quad (4.21)$$

$$B_i = \frac{-\delta_i}{8} exp\left[\frac{(\phi_{C,i} - V_{f,i})}{V_T}\right] \quad (4.22)$$

$$\phi_i(r) = V_{f,i} - \frac{qN_i r^2}{4\varepsilon_{Si}} - 2V_T\,ln\left[\frac{R}{2\alpha_i L_{D,i}}\left(1 - \frac{\alpha_i^2 r^2}{R^2}\right)\right] \quad (4.23)$$

Where, $L_{D,i} = \sqrt{\frac{2}{\delta_i}}$ and $0 < \alpha_i << 1, 0 \leq \frac{r}{R} \leq 1$

$$1 - \alpha_i^2 = 1 + B_i R^2 \tag{4.24}$$

$\alpha_i$could be found explicitly from Eq. 4.16 and 4.23 or implicitly as (Yu *et al.*, 2007).

4.2.1.4 Solving 2-D Laplace's equation

Using separation of variables the solution of Eq. 4 can be obtained as (Trivedi, Kumar, Haldar, S S Deswal, *et al.*, 2016):

$$v_i(r,z) = \sum_1^{\infty} J_0\left(\frac{\beta_{n,i}\, r}{R}\right)\left[C_{n,i}\, e^{\frac{\beta_{n,i} z}{R}} + D_{n,i}\, e^{\frac{-\beta_{n,i} z}{R}}\right] \tag{4.25}$$

$C_{n,i}$ and $D_{n,i}$ are arbitrary constants for the region $R_i(i = 1,\ 2)$, which can be calculated from Eq. 4.23 and 4.25 with boundary conditions below:

$$\varepsilon_{Si} \frac{dv_{(i)}(r,z)}{dr}\bigg|_{r=R} = C_{ox(i)}[v_i(r,z)] \tag{4.26}$$

$$\psi_1(r,0) = V_{bi,1} \quad \text{and} \quad \psi_2(r,L) = V_{bi,2} + V_{DS} \tag{4.27}$$

where $V_{bi,(1,2)} = V_T\, ln\left(N_{S,D}/N_i\right)$

$$\psi_1(r,L_1) = \psi_2(r,L_1) \ \text{ and } \ \frac{d\psi_1(r,L_1)}{dz} = \frac{d\psi_2(r,L_1)}{dz} \tag{4.28}$$

From Eq. 4.24 and 4.25 we get the eigenvalues $\beta_{n,i}$ obtained by solving the following equation:

$$J_0(\beta_{n,i}) = -\frac{\varepsilon_{Si}\beta_{n,i}}{C_{ox,i}R} J_1(\beta_{n,i}) \tag{4.29}$$

where J_0 and J_1 are the Bessel's function of order 0 and 1, respectively; Now $C_{n,i}$ and $D_{n,i}$ $(i = 1,\ 2)$ can be expressed as

$$\begin{pmatrix} \boldsymbol{C_{n,1}} \\ \boldsymbol{D_{n,1}} \end{pmatrix} = \frac{1}{\Delta_1}\begin{pmatrix} \mathbf{1} & P_{11} \\ \mathbf{-1} & P_{12} \end{pmatrix} \begin{pmatrix} A_{11} + Q_{11} \\ D_{11} \end{pmatrix} \tag{4.30}$$

$$\begin{pmatrix} \boldsymbol{C_{n,2}} \\ \boldsymbol{D_{n,2}} \end{pmatrix} = \frac{1}{\Delta_2}\begin{pmatrix} exp(-\beta_{n,2}L/R) & P_{21} \\ -exp(\beta_{n,2}L/R) & P_{22} \end{pmatrix}\begin{pmatrix} A_{12}+Q_{12} \\ D_{12} \end{pmatrix} \tag{4.31}$$

where, $P_{11} = \left[\frac{\beta_{n,1}}{\beta_{n,2}}\boldsymbol{sinh}\left(\frac{\beta_{n,2}\boldsymbol{L_2}}{\boldsymbol{R}}\right) - \boldsymbol{cosh}\left(\frac{\beta_{n,2}\boldsymbol{L_2}}{\boldsymbol{R}}\right)\right]\exp\left(\frac{-\boldsymbol{\beta_{n,1}L_1}}{\boldsymbol{R}}\right)$ (4.32)

$$P_{12} = \left[\frac{\beta_{n,1}}{\beta_{n,2}}\boldsymbol{sinh}\left(\frac{\beta_{n,2}\boldsymbol{L_2}}{\boldsymbol{R}}\right) + \boldsymbol{cosh}\left(\frac{\beta_{n,2}\boldsymbol{L_2}}{\boldsymbol{R}}\right)\right]\exp\left(\frac{\boldsymbol{\beta_{n,1}L_1}}{\boldsymbol{R}}\right) \tag{4.33}$$

$$P_{21} = -\left[\frac{\beta_{n,2}}{\beta_{n,1}}\boldsymbol{sinh}\left(\frac{\beta_{n,1}\boldsymbol{L_1}}{\boldsymbol{R}}\right) + \boldsymbol{cosh}\left(\frac{\beta_{n,1}\boldsymbol{L_1}}{\boldsymbol{R}}\right)\right]\exp\left(\frac{-\boldsymbol{\beta_{n,2}L_1}}{\boldsymbol{R}}\right) \tag{4.34}$$

$$P_{22} = \left[\boldsymbol{cosh}\left(\frac{\beta_{n,1}\boldsymbol{L_1}}{\boldsymbol{R}}\right) - \frac{\beta_{n,2}}{\beta_{n,1}}\boldsymbol{sinh}\left(\frac{\beta_{n,1}\boldsymbol{L_1}}{\boldsymbol{R}}\right)\right]\exp\left(\frac{\boldsymbol{\beta_{n,2}L_1}}{\boldsymbol{R}}\right) \tag{4.35}$$

$$Q_{11} = \boldsymbol{cosh}\left(\frac{\beta_{n,2}\boldsymbol{L_2}}{\boldsymbol{R}}\right)(\boldsymbol{B_{11}} + \boldsymbol{C_{11}}) \tag{4.36}$$

$$Q_{12} = \boldsymbol{cosh}\left(\frac{\beta_{n,1}\boldsymbol{L_1}}{\boldsymbol{R}}\right)(\boldsymbol{B_{12}} + \boldsymbol{C_{12}}) \tag{4.37}$$

$u_i = \frac{\beta_{n,i}^2[J_0{}^2(\beta_{n,i})+J_1{}^2(\beta_{n,i})]}{2}$ and $w_i = \beta_{n,i}J_1(\beta_{n,i})$ (4.38)

$$V_i = [\beta_{n,i}J_1(\beta_{n,i}) - 2J_2(\beta_{n,i})] \tag{4.39}$$

Since, $ln\left(1-\alpha_i^2\frac{r^2}{R^2}\right) = -\alpha_i^2\frac{r^2}{R^2} - \frac{(\alpha_i^2)^2}{2}\left(\frac{r^2}{R^2}\right)^2 - \ldots = -\alpha_i^2\frac{r^2}{R^2}$ neglecting higher values from conditions of Eq. 4.23

$$b_i = \frac{-qN_iR^2}{4\varepsilon_{Si}} - 2V_T\alpha_i^2,\ a_i = \left[V_{f,i} - 2V_T\ ln\left(\frac{R}{2L_{D,i}\alpha_i}\right)\right] \tag{4.40}$$

$$\Delta_2 = -2\left[cosh\left(\frac{\beta_{n,1}L_1}{R}\right)sinh\left(\frac{\beta_{n,2}L_2}{R}\right) + \frac{\beta_{n,2}}{\beta_{n,1}}sinh\left(\frac{\beta_{n,1}L_1}{R}\right)cosh\left(\frac{\beta_{n,2}L_2}{R}\right)\right] \tag{4.41}$$

$$\Delta_1 = 2\left[cosh\left(\frac{\beta_{n,2}L_2}{R}\right)sinh\left(\frac{\beta_{n,1}L_1}{R}\right) + \frac{\beta_{n,1}}{\beta_{n,2}}sinh\left(\frac{\beta_{n,2}L_2}{R}\right)cosh\left(\frac{\beta_{n,1}L_1}{R}\right)\right] \tag{4.42}$$

$$A_{11} = \frac{w_1(V_{bi,2}+b_2V_2-w_2a_2+V_{DS})}{u_1w_2},\ B_{11} = \frac{w_2b_1V_1-w_1b_2V_2}{w_2u_1} \tag{4.43}$$

$$C_{11} = \frac{w_1(a_2-a_1)}{u_1}, \quad D_{11} = \frac{V_{bi,1}+b_1V_1-w_1a_1}{u_1} \tag{4.44}$$

$$A_{12} = \frac{w_2(V_{bi,1}+b_1V_1-w_1a_1)}{u_2w_1}, \quad B_{12} = \frac{w_1b_2V_2-w_2b_1V_1}{w_1u_2} \tag{4.45}$$

$$C_{12} = \frac{w_2(a_1-a_2)}{u_2}, \; D_{12} = \frac{V_{bi,2}+V_{DS}+b_2V_2-w_2a_2}{u_2} \tag{4.46}$$

4.2.1.5 Modelling of lateral electric field

The electric field could be defined as a gradient of potential and can be expressed as:

$$E_{z,i} = -\frac{d\psi_i(r,z)}{dz}\bigg|_{(i=1,\,2)} = \sum_1^{\infty} J_0\left(\frac{\beta_{n,i}r}{R}\right)\frac{\beta_{n,i}}{R}\left[C_{n,i}\,exp(\,\beta_{n,i}z/R) - D_{n,i}\,exp(\,-\beta_{n,i}z/R)\right] \tag{4.47}$$

4.2.2 Formulation of threshold voltage

The threshold voltage (V_{th}) is an important parameter for any MOS device. It can be defined as the gate-to-source voltage at which the minimum central potential is equal to the intrinsic Fermi potential for a junctionless device (Gupta, 2015). Since the region R_1 has lower doping than the region R_2, the minimum potential will lie in the R_1 region. The location of the minimum central potential can be obtained by solving

$$\frac{d\psi_i(r,z)|}{dz}\bigg|_{r=0,z=z_{min}} \text{ which, gives } z_{min} = \frac{R}{2\beta_{n,i}}\,ln\left(\frac{D_{n,i}}{C_{n,i}}\right) \tag{4.48}$$

At threshold accumulation charges are 0 (by depletion approximation). Therefore $\phi_{A,i}(r) = 0$, From Eq. 4.20, 4.22 and 4.24 we get $\alpha_i^2 = 0$, putting its value in Eq 4.40 we get

$$b_i = \frac{-qN_iR^2}{4\varepsilon_{Si}} = b_{1,i} \tag{4.49}$$

From Eq. 16, 23 and 41 we get:

$$a_i = \left[V_{f,i} - 2V_T\,ln\left(\frac{R}{2L_{D,i}\alpha_i}\right)\right] = V_{f,i} + V_{GS} - V_{fb,i} - V_{f,i} + \frac{qN_1R^2}{4\varepsilon_{Si}} + \frac{qN_1R}{2C_{ox,i}} = a_{1,i} \tag{4.50}$$

$$\psi_{min}(r, z_{min}) = V_{GS} + a_{01,i}\sqrt{C_{n,j}D_{n,j}} \tag{4.51}$$

where, $a_{01,i} = a_{1,i} - V_{GS}$.

Now, equating the minimum potential to the Fermi potential ($\varphi_{fi} = V_{f,i}$) and changing V_{GS} to V_{th}, the threshold voltage, V_{th}, can be obtained as (Gupta, 2015):

$$\psi_{min}(r, z_{min})|_{V_{GS}=V_{th}} = \varphi_{fi} \tag{4.52}$$

which gives

$$\left(V_{GS} + 2\sqrt{C_{n,i}D_{n,i}}\right)\Big|_{V_{GS}=V_{th}} = V_{tL}\,, V_{tL} = \varphi_{fi} - a_{0i} \tag{4.53}$$

where V_{tL} is the long channel threshold voltage

Since the minimum central potential lies in the R_1 region, it can be written as (Cong *et al.*, 2014; Pratap *et al.*, 2014a):

$$A_{11} = E_{12} - F_{12}V_{th} \text{ and } D_{11} = E_{11} - F_{11}V_{th} \tag{4.54}$$

$$\text{where, } C_{n,1}D_{n,,1} = G_1 + G_2V_{th} + G_3{V_{th}}^2 \tag{4.55}$$

Now, the threshold voltage can be expressed as:

$$\partial_1{V_{th}}^2 + \partial_2V_{th} + \partial_3 = 0 \tag{4.56}$$

$$E_{11} = \frac{1}{u_1}\left[V_{bi,1} + b_{1,1}V_1 - w_1a_{01,1})\right], \qquad F_{11} = \frac{w_1}{u_1} \tag{4.57}$$

$$E_{12} = \frac{1}{u_2w_2}\left[w_1\left(V_{bi,2} + b_{1,2}V_2 - w_2a_{01,2} + V_{DS}\right)\right], \quad F_{12} = \frac{w_1}{u_2} \tag{4.58}$$

$$G_1 = M_{11}M_{21}, G_2 = M_{11}M_{22} + M_{12}M_{21}, G_3 = M_{12}M_{22} \tag{4.59}$$

$$\partial_1 = 4G_3 - 1, \partial_2 = 4G_2 + 2V_{tL}, \partial_3 = 4G_1 - {V_{tL}}^2 \tag{4.60}$$

$$M_{11} = \frac{1}{\Delta_1}\left[E_{12} + N_{11} - E_{11}[N_{13} - N_{12}]exp\left(\frac{-\beta_{n,1}L_1}{R}\right)\right] \tag{4.61}$$

$$M_{12} = \frac{1}{\Delta_1}\left[F_{11}[N_{13} - N_{12}]exp\left(\frac{-\beta_{n,1}L_1}{R}\right) - F_{12}\right] \tag{4.62}$$

$$M_{21} = \frac{1}{\Delta_1}\left[-E_{12} - N_{11} + E_{11}[N_{13} + N_{12}]exp\left(\frac{\beta_{n,1}L_1}{R}\right)\right] \quad (4.63)$$

$$M_{22} = \frac{1}{\Delta_1}\left[F_{12} - F_{11}[N_{13} + N_{12}]exp\left(\frac{\beta_{n,1}L_1}{R}\right)\right] \quad (4.64)$$

$$N_{11} = cosh\left(\frac{\beta_{n,2}L_2}{R}\right)[B_{11} + C_{11}] \quad (4.65)$$

$$N_{12} = cosh\left(\frac{\beta_{n,2}L_2}{R}\right),\ N_{13} = \frac{\beta_{n,1}}{\beta_{n,2}}sinh\left(\frac{\beta_{n,2}L_2}{R}\right) \quad (4.66)$$

$$V_{th} = \frac{-\partial_2 \pm \sqrt{(\partial_2{}^2 - 4\partial_1\partial_3)}}{2\partial_1} \quad (4.67)$$

Since threshold voltage of a Junctionless MOSFET is always positive, the positive sign has been considered in Eq. 4.67.

4.2.2.1 Modelling of threshold voltage roll-off and DIBL

The threshold voltage roll-off can be defined as the difference in threshold voltage between the short channel and long channel device and can be expressed as (Cong *et al.*, 2014; Pratap *et al.*, 2014a):

$$V_{roll-off} = V_{th}|_{short-channel} - V_{tL} \quad (4.68)$$

The drain induced barrier lowering (DIBL) can be expressed as (Pratap *et al., 2014a;* Goel *et al.,* 2016a) or difference of minimum central potential in the model:

$$DIBL = -\frac{V_{th}|_{V_{DS}=0.05\text{V}} - V_{th}|_{V_{DS}=1\text{V}}}{V_{DS}(0.05\text{V}) - V_{DS}(1\text{V})}\ \text{mV/V} \quad (4.69)$$

4.2.3 Total drain current modelling with GIDL

Drain current of a device is an important parameter for switching purposes. Higher the ratio of I_{ON}/I_{OFF} higher is the noise tolerance of the device. A complete drain current model for various regions is expressed as (Pratap *et al.*, 2014a; Trivedi, Kumar, Haldar, S. S. Deswal, *et al.*, 2016);

$$I_D = \begin{bmatrix} I_{btbt} for - 1V \leq V_{GS} \leq 0V \\ I_{sub} for 0V < V_{GS} \leq V_{th} \\ I_{sat} for V_{th} < V_{GS} \leq V_{DS} + V_{th} \\ I_{lin} for V_{DS} + V_{th} < V_{GS} \leq V_{DD} = 1V \end{bmatrix} \tag{4.70}$$

For I_D- V_{DS} analysis when, $V_{GS} > V_{th}$

$$I_D = \begin{bmatrix} I_{lin} for V_{DS} < V_{GS} - V_{th} \\ I_{sat} for V_{DS} \geq V_{GS} - V_{th} \end{bmatrix} \tag{4.71}$$

I_{btbt} could be defined as the gate induced drain leakage due to band-to-band tunneling in the overlap region near the drain junction. BTBT generation rate could be defined as (Bouhdada *et al.*, 1997; Sachdeva, Vashishath and Bansal, 2018);

$$BTBT_{gen} = A \times E^2{}_{tot}\, exp\left(\frac{-B}{E_{tot}}\right) \tag{4.72}$$

where, $A = \frac{q^2 m_r{}^{0.5}}{18\pi h^2 E_{g,2}{}^{0.5}}$ and $B = \frac{\pi m_r{}^{0.5} E_{g,2}{}^{0.5}}{2\sqrt{2}qh} = 2.13MV/m$

$$E^2{}_{tot} = E^2{}_{si} + E^2{}_h \tag{4.73}$$

$$I_{btbt} = 2\pi R^2 \Delta L \times BTBT_{gen} \tag{4.74}$$

$$E_{si} = \frac{qN_{D,S}}{\varepsilon_{si}} \sqrt{\frac{2\varepsilon_{si}\psi_{si}}{qN_{D,S}}},\, E_h = V_{DS} - V_{GS} / \left(\frac{\varepsilon_{si}}{\varepsilon_{ox}} t_{ox} \varpi\right)^2 \tag{4.75}$$

$$\psi_{si} = (V_{DS} - V_{GS}) - V_{fb,2} + \frac{qN_{D,S} t_{ox}^2 \varepsilon_{si}}{\varepsilon_{ox}^2} \times$$

$$\left[\sqrt{\left[\frac{qN_{D,S} t_{ox}^2 \varepsilon_{si}}{\varepsilon_{ox}^2} + (V_{DS} - V_{GS}) - V_{fb,2}\right]^2 - \left((V_{DS} - V_{GS}) - V_{fb,2}\right)^2}\right] \tag{4.76}$$

$$\varpi = \frac{10^{-4} R^{2/3} L^{2/5}}{t^{3/4}{}_{ox}},\, \Delta L = \sqrt{\frac{2\varepsilon_{si}\psi_{si}}{qN_{D,S}}} \tag{4.77}$$

where, ΔL is the length of the overlapped area, m_r=0.37m_0 where m_0 is mass of electron at rest, E_{si} and E_h are vertical and horizontal field respectively inside the band overlapped area and h

is the Plank constant (Chen, Wong and Wang, 2001). The vertical field is the field in the depleted band overlapped area and is calculated as (Chen, Wong and Wang, 2001).

$$I_{sub} = 2\pi R^2 \mu_{ef,1f} q V_T n_{i,1} \left(\frac{1 - exp\left(\frac{-V_{DS}}{V_T}\right)}{\int_0^L \frac{1}{\int_0^R exp\left(\frac{\psi_{min}(r, z_{min})}{V_T}\right) dr} dz} \right) \tag{4.78}$$

$$I_{sat} = \frac{2\pi R \mu_{ef,2f} C_{ox,2}}{\left(1+\frac{V_{Dsat}}{E_C L}\right)(L-L_{sat})} \begin{bmatrix} \rho(V_{GS} - V_{ths})^{\gamma} V_{Dsat} - \frac{\theta_s V^2{}_{Dsat}}{2} \\ +V_T \theta_s (1 + exp\left(\frac{V_{DS}-V_{Dsat}}{V_T}\right) \end{bmatrix} \tag{4.79}$$

$$\theta_s = 0.1 \Big/ \left. \frac{\partial \psi_{min}(0, z_{min})}{\partial V_{GS}} \right|_{V_{GS}=V_{th}} \tag{4.80}$$

$$V_{ths} = V_{th}(1 - \theta_s), E_C = \frac{2V_{sat}}{\mu_{eff,2}} \tag{4.81}$$

$$V_{Dsat} = \frac{V_{GS}-V_{th}}{1+\frac{(V_{GS}-V_{th})\mu_{eff,2}}{LV_{sat}}} \tag{4.82}$$

$$L_{sat} = \lambda\, ln \left(\frac{V_{DS}-V_{Dsat}}{E_C L + \sqrt{1+\left(\frac{V_{DS}-V_{Dsat}}{E_C L}\right)^2}} \right) \tag{4.83}$$

In Eq. 4.78 I_{sub} could be calculated by the minimum potential method as (Li *et al.*, 2014; Pratap *et al.*, 2014a, 2015); As the minimum potential is highest for region-1, only region-1 is taken for the calculation (Li *et al.*, 2014; Goel *et al.*, 2016a)

For Eq. 4.79 γ is a fitting parameter varying between 0.5 to 1.5, γtaken here is 1.3 (Trivedi, Kumar, Haldar, S. S. Deswal, *et al.*, 2016). L_{sat} is the characteristics length, whereas $\rho$is a fitting

parameter depending on technology varying between 0 and 1; the value of ρ taken is 0.72, E_C is critical field V_{sat} is critical velocity. λ is also a fitting parameter whose value depends on permittivities and thickness of semiconductor and gate oxide, given by-$\varepsilon_{ox}t_{Si}/\varepsilon_{Si}t_{ox}$. V_{sat} is the saturation velocity assumed as 1.03×10^7cm/s (Pratap *et al.*, 2015; Trivedi, Kumar, Haldar, S. S. Deswal, *et al.*, 2016). Current in the linear region could be calculated as below:

$$I_{lin} == \frac{2\pi R\mu_{eff,1}C_{ox,1}}{(E_C L+V_{DS})(L-L_{sat})}\left[(V_{GS}-V_{ths})^{\gamma/2}V_{DS}-\frac{\theta_S {V_{DS}}^2}{2}\right] \tag{4.84}$$

$$\mu_e(N_f) = 1000\times\left(3\times10^{11}/_{N_f}\right)\left(^{T}/_{80}\right) \tag{4.85}$$

$$^1/_{\mu_{eff,1}} = {^1/_{\mu_e}} + {^1/_{\mu_{e,1}(T)}}, {^1/_{\mu_{eff,2}}} = {^1/_{\mu_e}} + {^1/_{\mu_{e,2}(T)}} + {^1/_{\mu_e(N_f)}} \tag{4.86}$$

$$\mu_{e,i}(T) = \mu_{\min} + \frac{\mu_{\max}\left(^T/_{300}\right)^{\tau 1} - \mu_{\min}}{1+\mu_{\max}\left(^T/_{300}\right)^{\tau 2}\left(^{N_i}/_{N_{ref}}\right)^{\tau 3}} \tag{4.87}$$

$$\mu_{max}=1330,\ \ \mu_e = 1400,\ \ \mu_{min}=65\ \text{cm}^2/\text{Vs} \tag{4.88}$$

$$N_{ref}=8.5\times10^{16}/\text{cm}^3,\ \tau 1 = -2.3, \tau 2 = -3.8 \text{ and } \tau 3 = 0.73 \tag{4.89}$$

Transconductance g_m is given by $g_m = \partial I_D/\partial V_{GS}$ (4.90)

Output-conductance g_d is given by $g_d = \partial I_D/\partial V_{DS}$ (4.91)

4.2.3.1 Subthreshold Slope modelling

Subthreshold slope (SS) is an essential parameter and important for switching characteristics of the device. SS could be formulated as below (Pratap *et al.*, 2014a; Trivedi, Kumar, Haldar, S. S. Deswal, *et al.*, 2016).

$$SS = \frac{dV_{GS}}{d\,log(I_{sub})} \tag{4.92}$$

4.3 Simulation setup

In this section, we have calibrated the simulation setup and validated our model with different reported analytical models. The calibration of the TCAD tool has been done by comparing the simulation data with the experimental results of a known device structure. After validation of the TCAD data, our proposed model results will be validated by comparing them with the simulation data in the next section. For fair comparisons, the arithmetic mean of doping N_1, N_2 (graded channel) and workfunction φ_{m1}, φ_{m2} (dual material) have been taken for the uniformly doped simple JAM MOSFET (Li *et al.*, 2014; Pratap *et al.*, 2014b). Further thickness of SiO_2 for JAM MOSFET is taken as 3 nm. Various parameters used for the computations are given in table 4.2. The analytical results have been validated by comparing them with the 3-D TCAD (Visual TCAD, 2017) simulation data. The *Fermi-Dirac*, *Lucent mobility* and *BGN,* models have been used for the carrier statistics, mobility and bandgap narrowing in the device, respectively. The *HotCarrier* model has been enabled in the TCAD simulator to account for the hot carrier effects. *DDML1* and *QDDM* solvers have been used for simulating the classical device (CL) with R≥5 nm and quantum-confined (QM) for devices R<5 nm respectively. Fig. 4.3(a) shows the calibration of the simulation setup with the experimental results of (Choi *et al.*, 2011) at V_{GS}=1 and 0.1 V, in both linear and logarithmic scale. Fig 4.3(b) demonstrates validation of our proposed model with that of the device model proposed for JLAMSG MOSFET in (Trivedi, Kumar, Haldar, S. S. Deswal, *et al.*, 2016), JLDMCSG MOSFET in (Li *et al.*, 2014) and Circular GCDMG MOSFET in (Banerjee and Sarkar, 2019). Therefore, our numerical simulations match well with experimental results and our proposed analytical model matches well with other reported analytical models.

TABLE 4.2: Specifications of Different Structures

MOSFET Type	*Source/ Drain Doping (N_S/N_D) (cm^{-3})*	*Channel Doping (cm^{-3}) N_1/N_2*	*Dielectric Gate-oxide*	*Gate Work-function (eV) $\varphi_{m1}/\varphi_{m2}$*	I_{on}/I_{off}
SHD-GC-DM-JAM	**10^{20}**	**5×10^{17}/ 5×10^{18}**	**SiO_2, 1 nm/(HfO_2-Air), 2 nm**	**4.9/4.7**	**1.24 $\times10^{12}$**
JAM	**10^{20}**	**1×10^{18}**	**SiO_2, 3 nm**	**4.8**	**1.4 $\times10^{9}$**

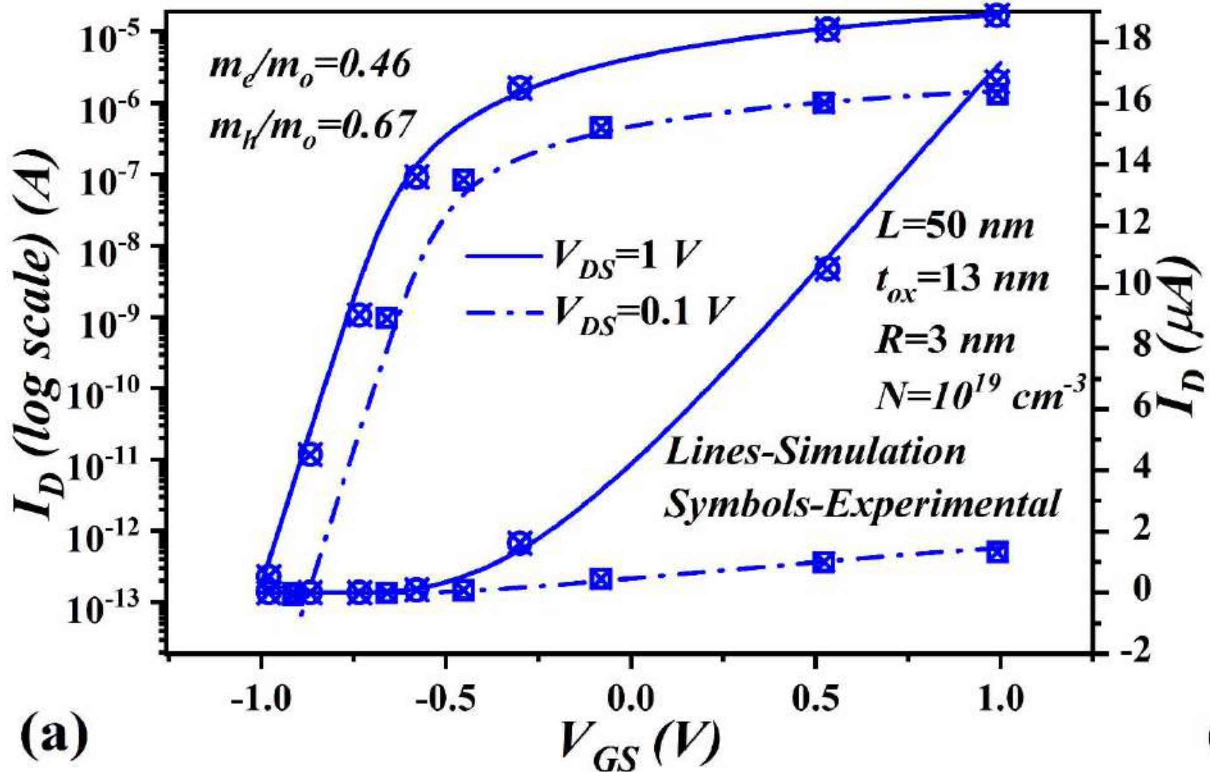

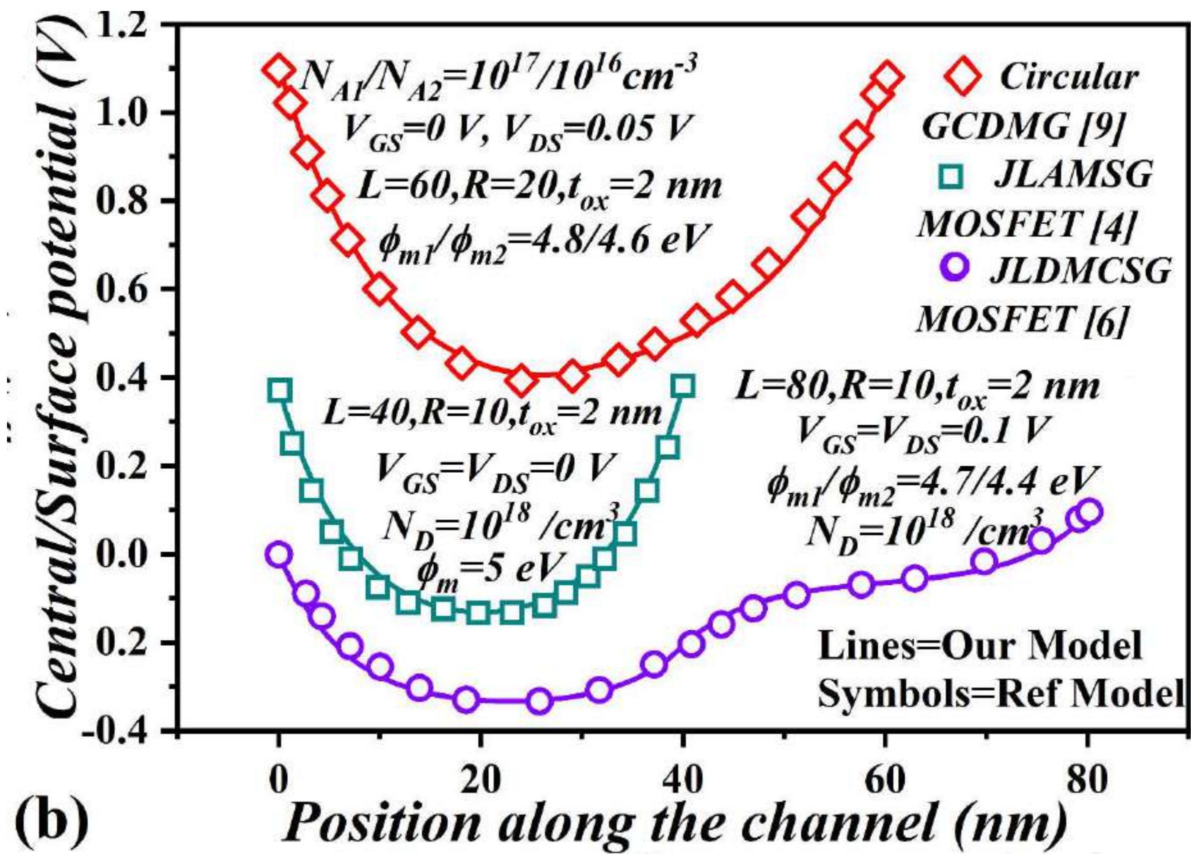

Fig. 4.3: (a) Calibration of the simulation setup with experimental results in [33] (b) Validity of our model with modeled results of (Li *et al.*, 2014[6]; Trivedi, Kumar, Haldar, S. S. Deswal, *et al.*, 2016[4]; Banerjee and Sarkar, 2019[9]) Electron ($m_e=0.46m_0$) and hole ($m_h=0.67m_0$) masses have been adjusted to match the experimental data in (Choi *et al.*, 2011).

4.4 Result and discussion

In this section, we have compared and analyzed our model results of our proposed SHD-GC-DM-JAM and simple JAM MOSFETs (Trivedi, Kumar, Haldar, S. S. Deswal, *et al.*, 2016). We have also validated our model results with those obtained from the commercially available TCAD simulation data to show the accuracy of our proposed analytical model. Fig. 4.4 (a) demonstrates the position of the minimum central potential shifting towards the drain side for all values of V_{GS} with an increase in L_1: L_2, thus increasing the effect of the drain on the channel. It could also be observed that the value of minimum central potential or depletion decreases with an increase in V_{GS}. For fig. 4.4(b) it could be observed that the electric field at drain end increases with L_1: L_2, (increase in HCEs). Therefore, SCEs decreases and HCEs

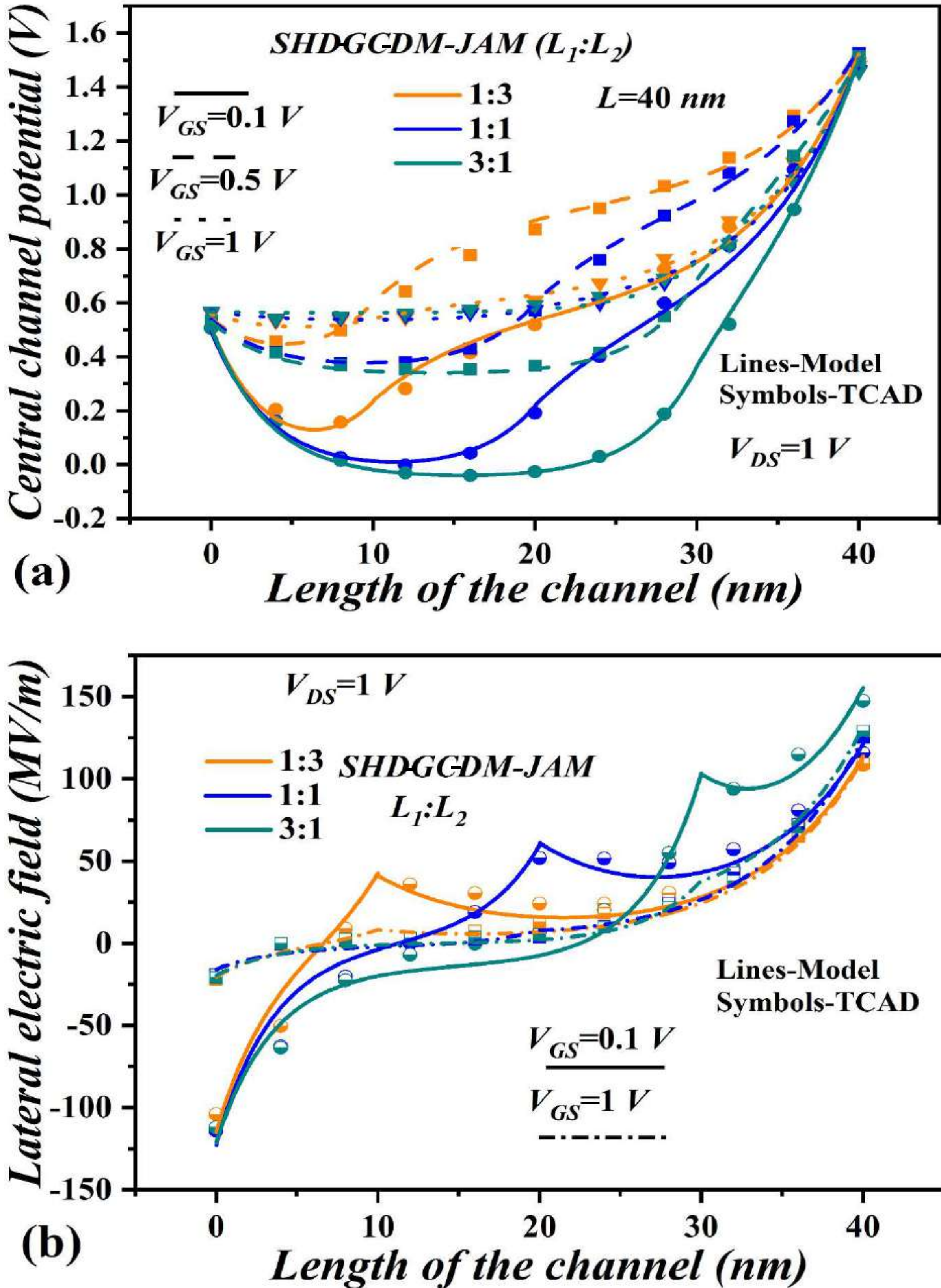

Fig. 4.4: (a) Central potential variation at V_{GS} (0.1, 0.5, 1 V) (b) Lateral electric field variation at V_{GS} (0.1, 1 V); against length of the channel for (L_1:L_2=1:3, 1:1, 3:1) at for SHD-GC-DM-JAM.

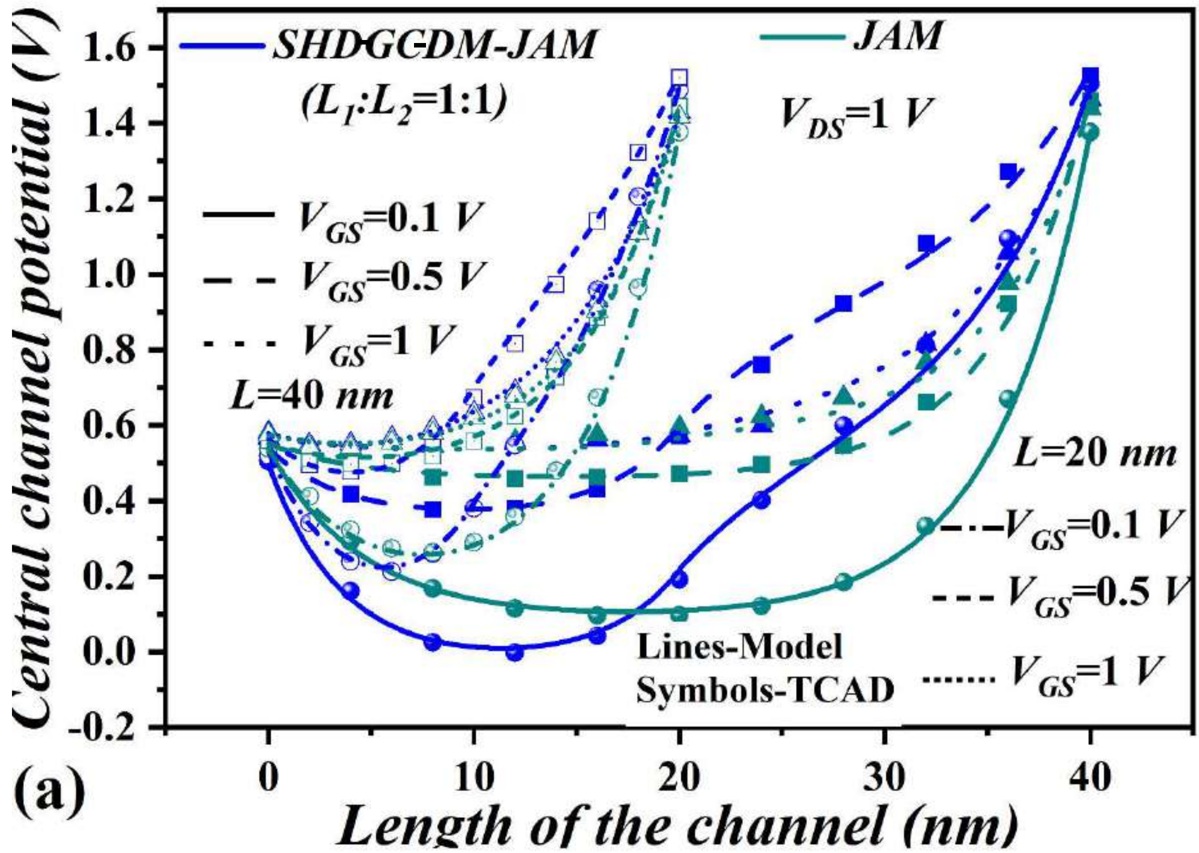

SHDGCDM-JAM
(L1:L2=1:1)
JAM
VDS=1 V
VGS=0.1 V
VGS=0.5 V
VGS=1 V
L=40 nm
L=20 nm
VGS=0.1 V
VGS=0.5 V
VGS=1 V
Lines-Model
Symbols-TCAD
Central channel potential (V)
Length of the channel (nm)
(a)

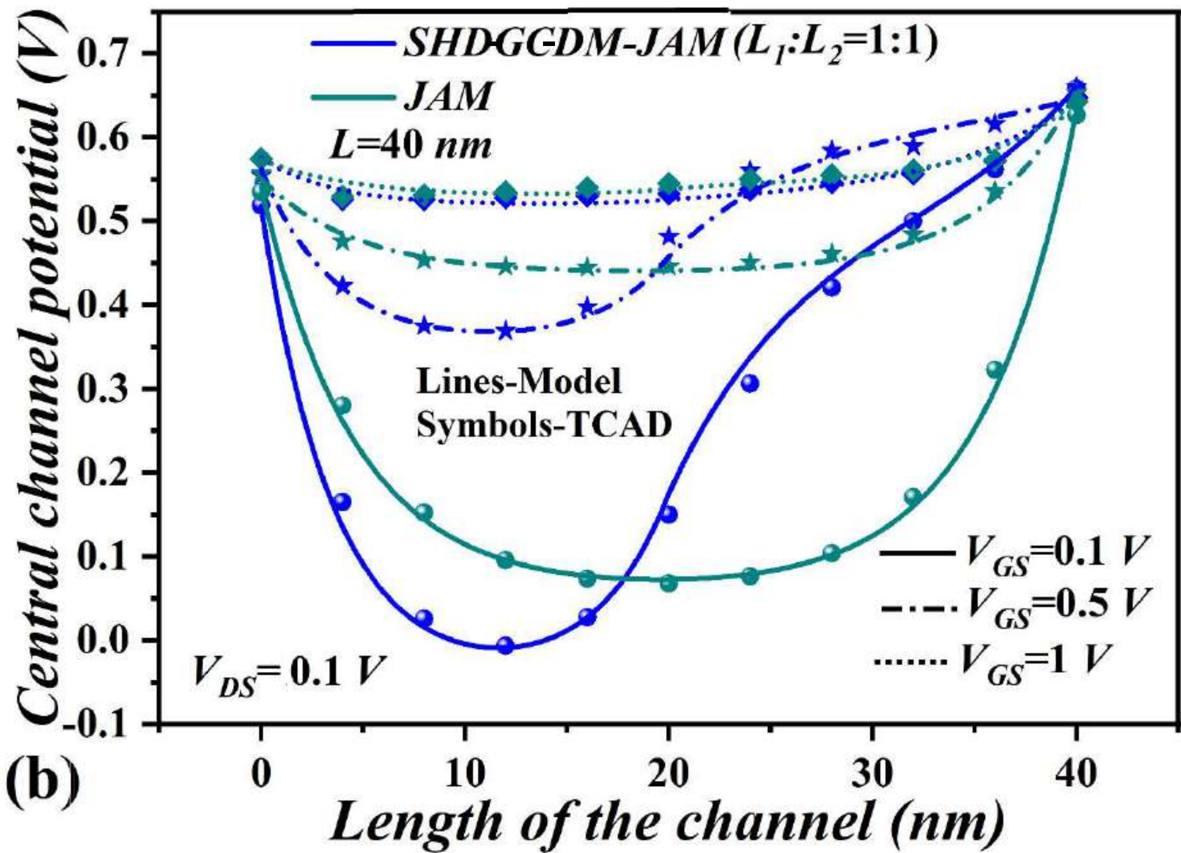

SHDGCDM-JAM (L1:L2=1:1)
JAM
L=40 nm
Lines-Model
Symbols-TCAD
VGS=0.1 V
VGS=0.5 V
VGS=1 V
VDS= 0.1 V
Central channel potential (V)
Length of the channel (nm)
(b)

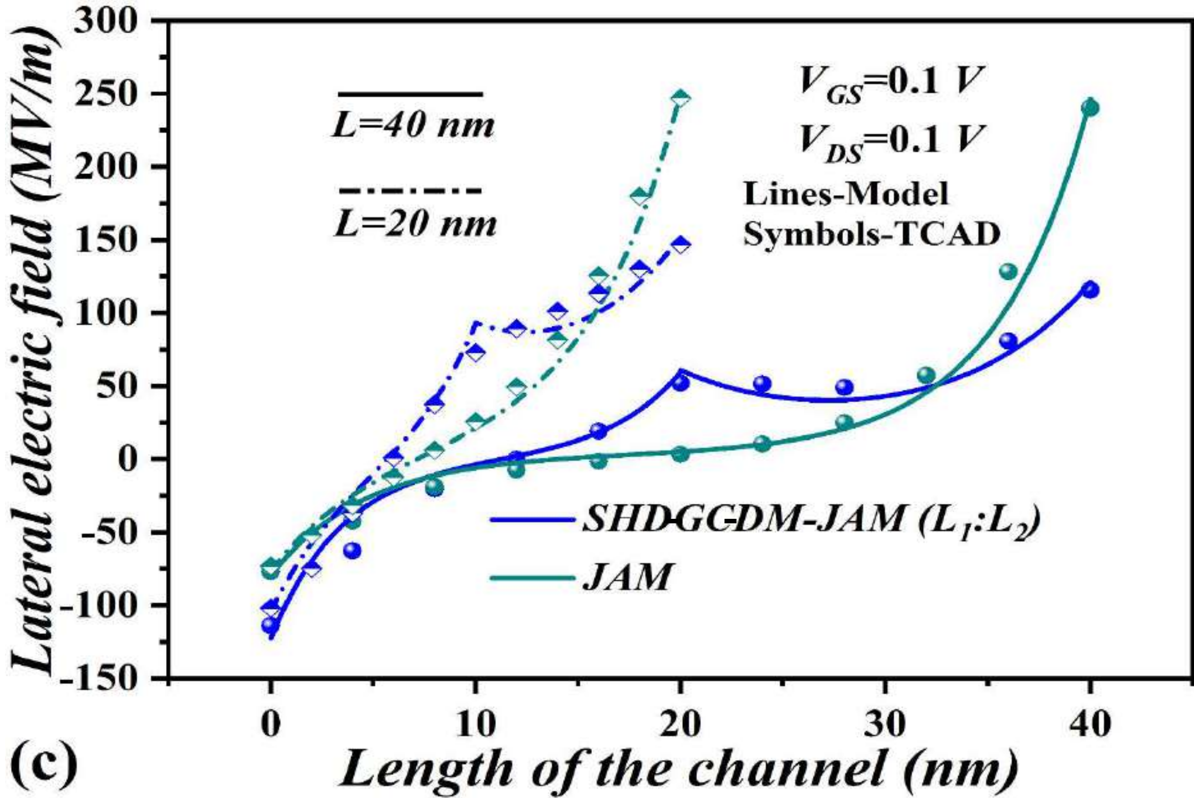

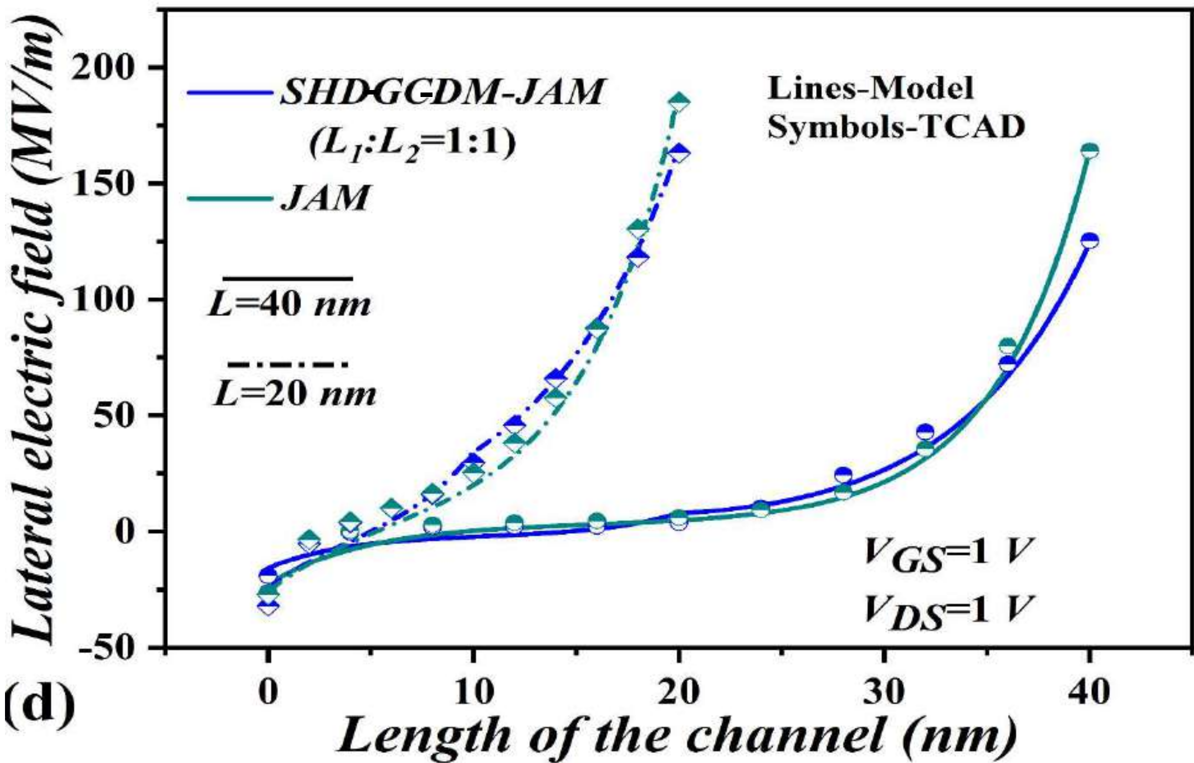

Fig. 4.5: Central potential variation vs length of the channel (a) V_{DS}=1 *V* (b) V_{DS}=0.1 *V*; for L=20 nm and 40 nm at (V_{GS}=0.1, 0.5, 1 *V*). Lateral electric field vs length of the channel (c) V_{DS}=0.1 *V*, V_{GS}=0.1 *V* (d) V_{DS}=1 *V*, V_{GS}= 1 *V;* at *L*=20 nm and 40 nm for JAM and SHD-GC-DM-JAM MOSFET.

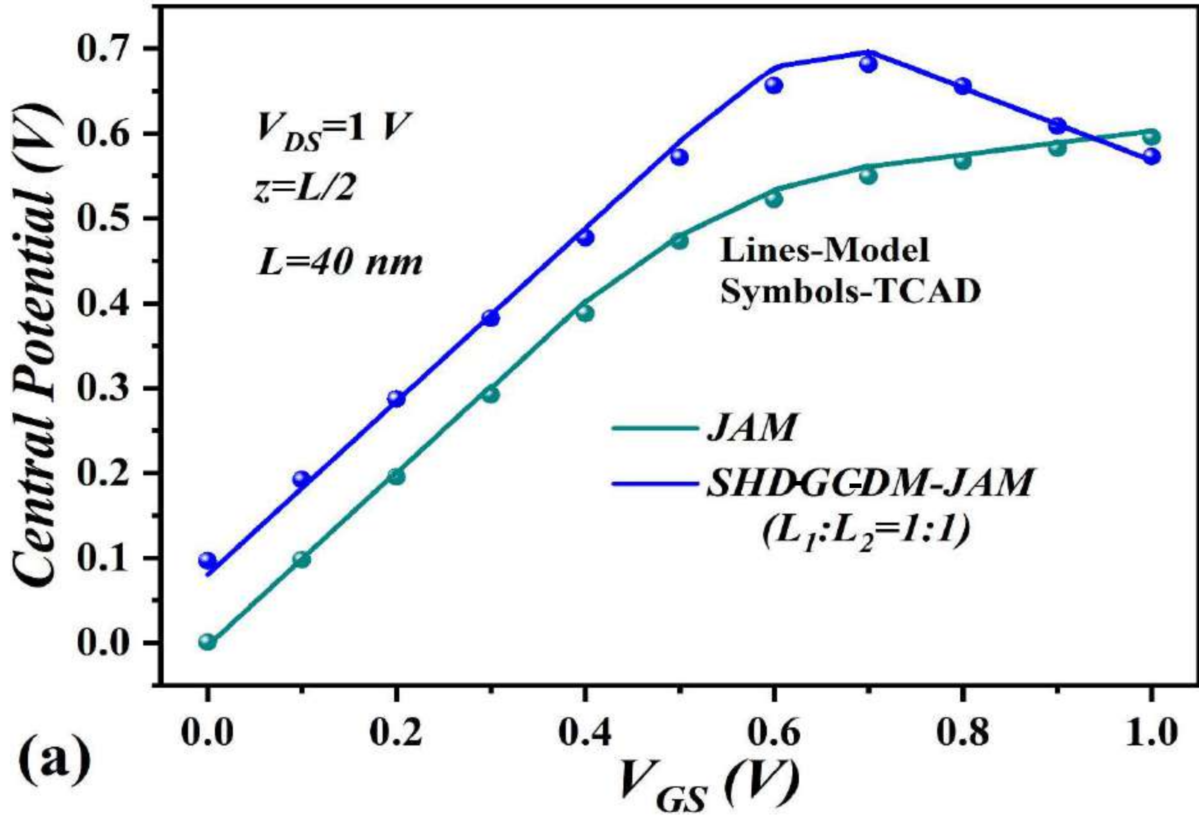

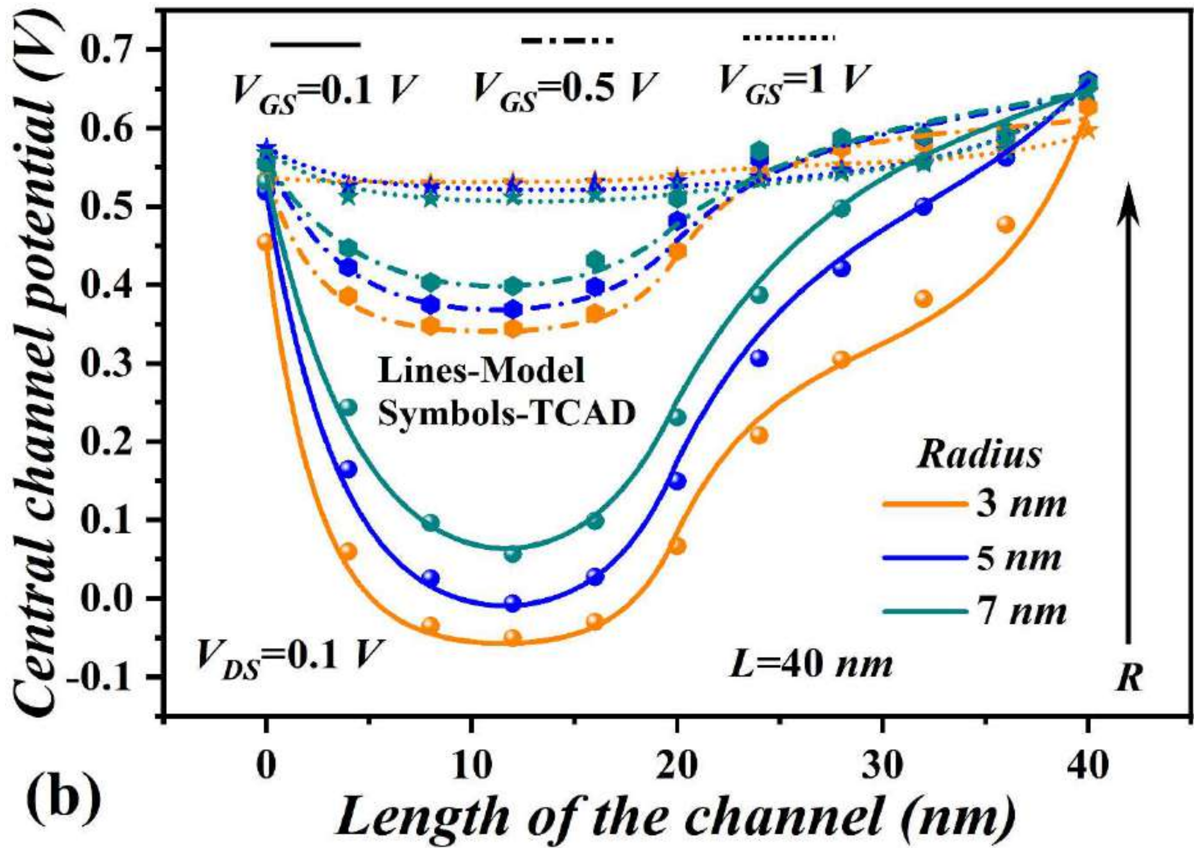

Fig. 4.6: (a) Central potential vs V_{GS} at z=L/2 and L=40 nm for JAM and SHD-GC-DM-JAM MOSFET (b) Central Potential variation vs length of the channel for SHD-GC-DM-JAM (R=3, 5, 7 nm) at (V_{GS}=0.1, 0.5, 1 V).

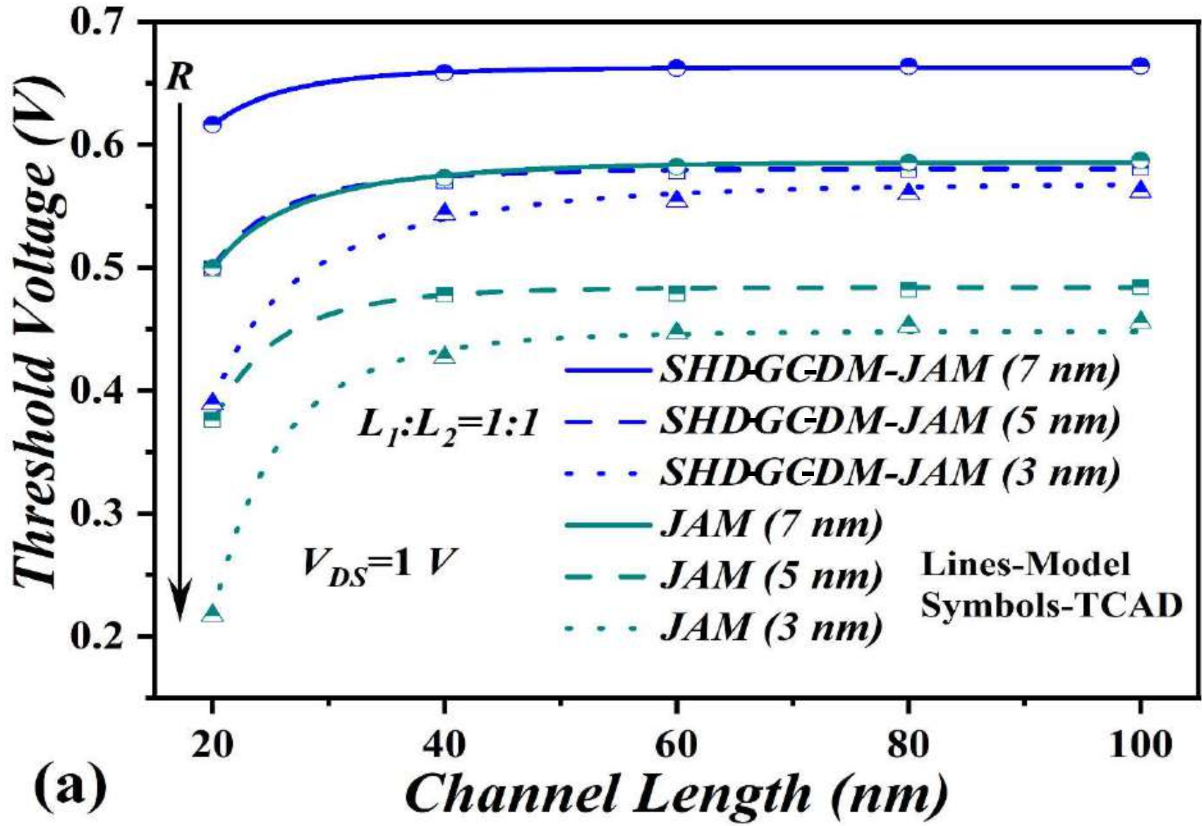

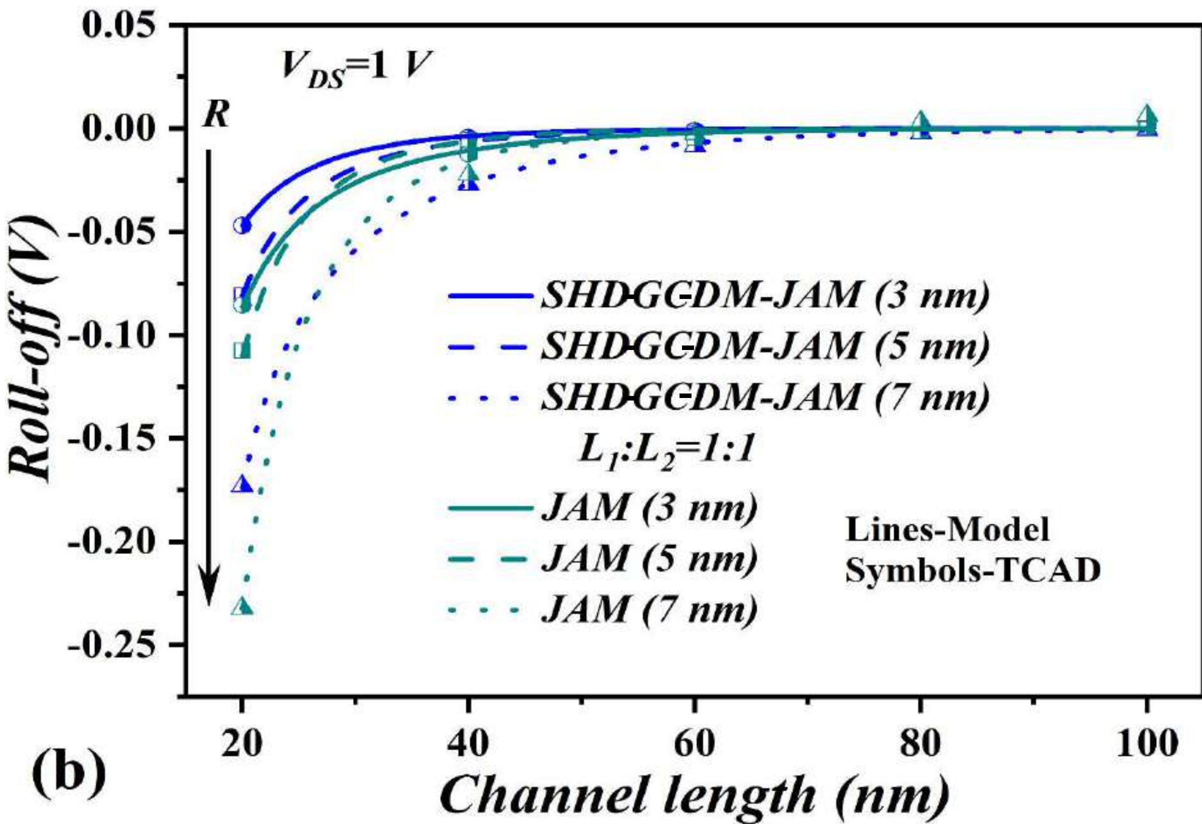

Fig. 4.7: (a)Threshold voltage (b) Roll-off; vs channel lengths at V_{DS}=1 V for SHD-GC-DM-JAM and JAM MOSFET (R=3, 5, 7 nm).

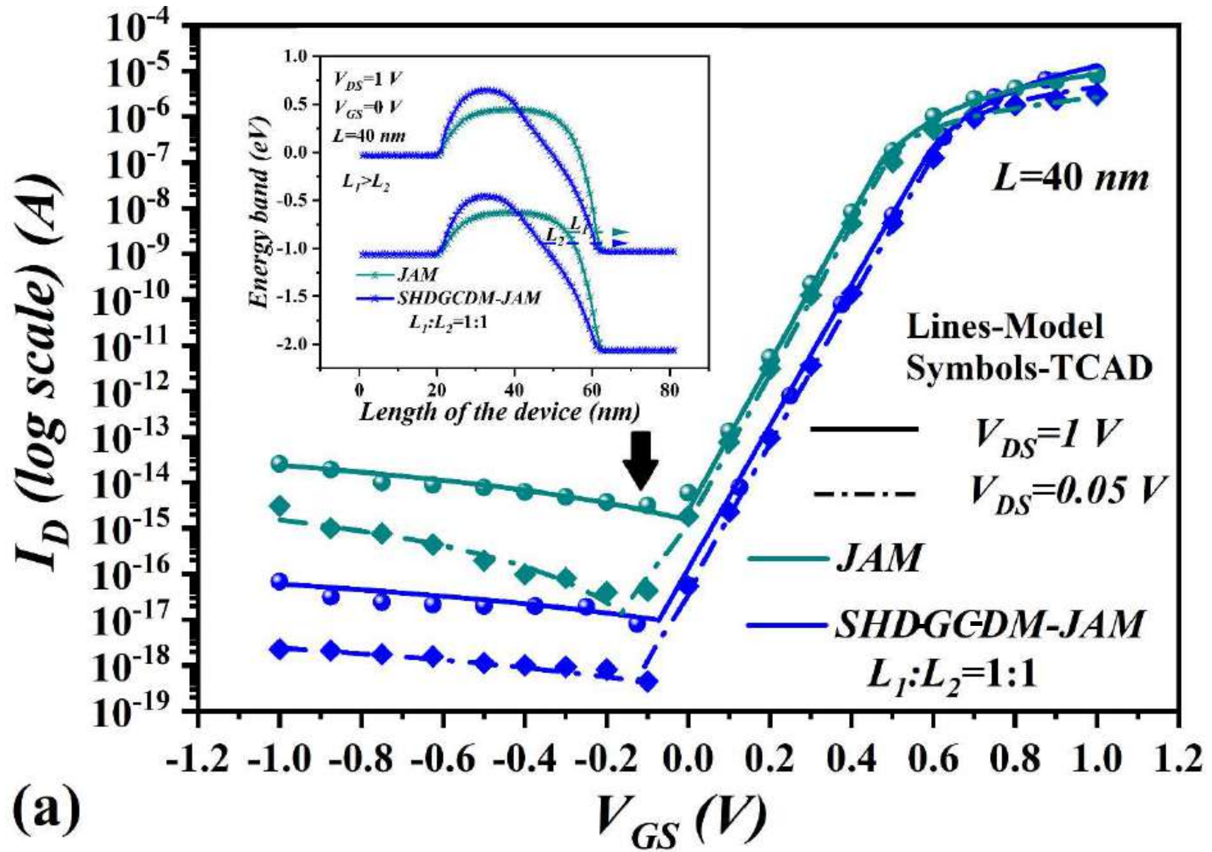
L=40 nm
Lines-Model
Symbols-TCAD
V_{DS}=1 V
V_{DS}=0.05 V
JAM
SHDGCDM-JAM
L_1:L_2=1:1
I_D (log scale) (A)
V_{GS} (V)
(a)
V_{DS}=1 V
V_{GS}=0 V
L=40 nm
L_1>L_2
Energy band (eV)
Length of the device (nm)

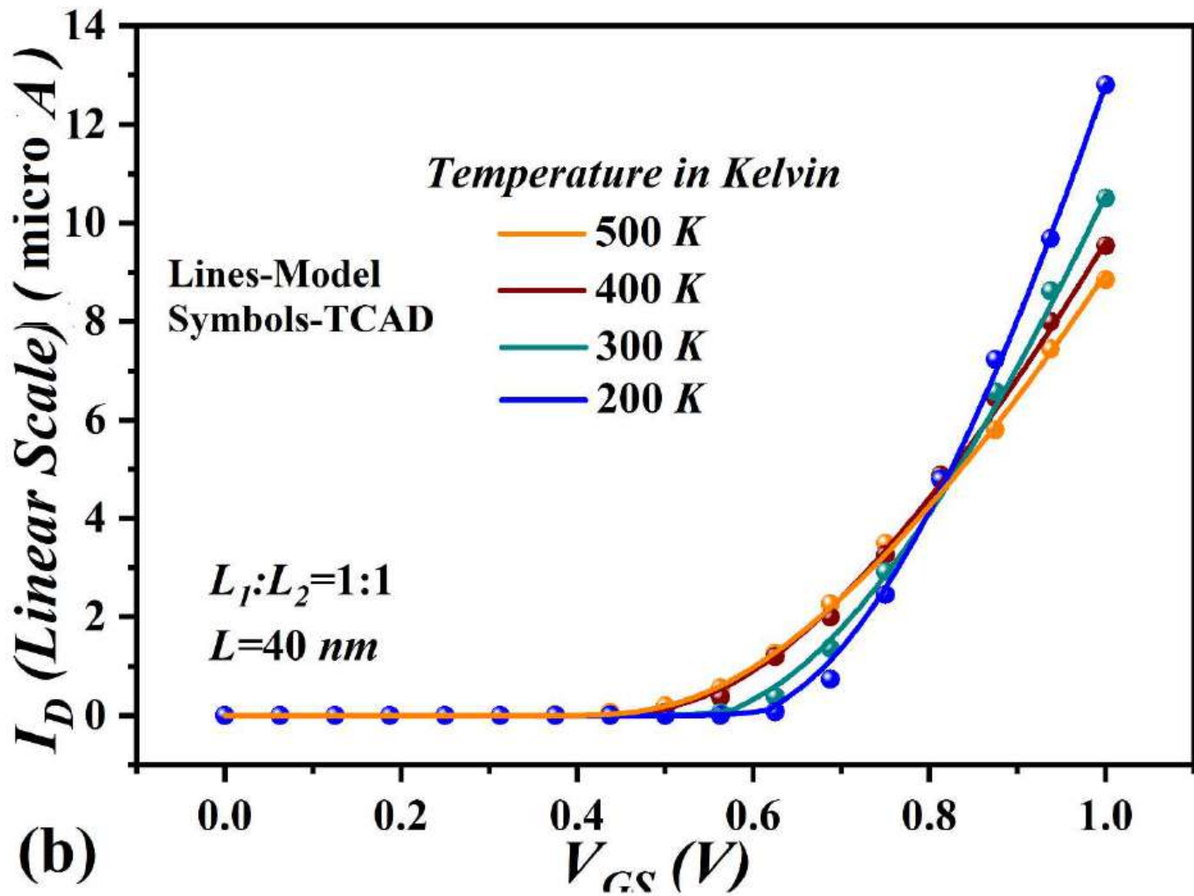
Temperature in Kelvin
500 K
400 K
300 K
200 K
Lines-Model
Symbols-TCAD
L_1:L_2=1:1
L=40 nm
I_D (Linear Scale) (micro A)
V_{GS} (V)
(b)

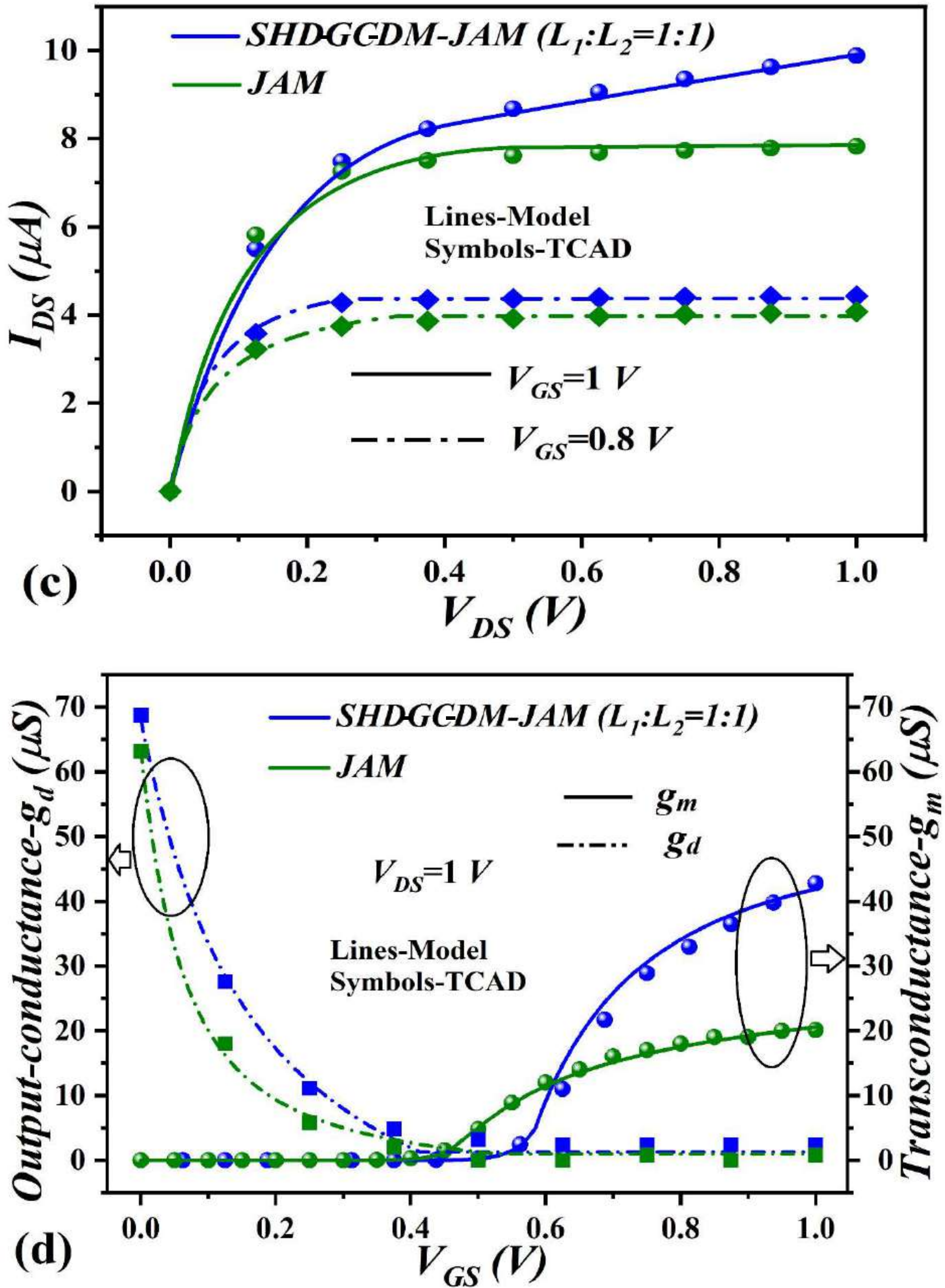

Fig. 4.8: (a) I_D vs V_{GS} (log scale) for JAM and SHD-GC-DM-JAM at (V_{DS}= 1 and 0.05 V; L=40 nm); inset –band diagram for devices(b) I_D vs V_{GS} (linear scale) for SHD-GC-DM-JAM at (V_{DS}=1 V; R=5 nm L=40 nm) and device temperature (T=200, 300, 400, 500 K) (c) I_D vs V_{DS} for (V_{GS}=1 and 0.8 V) (d) g_m at V_{DS}=1 V.

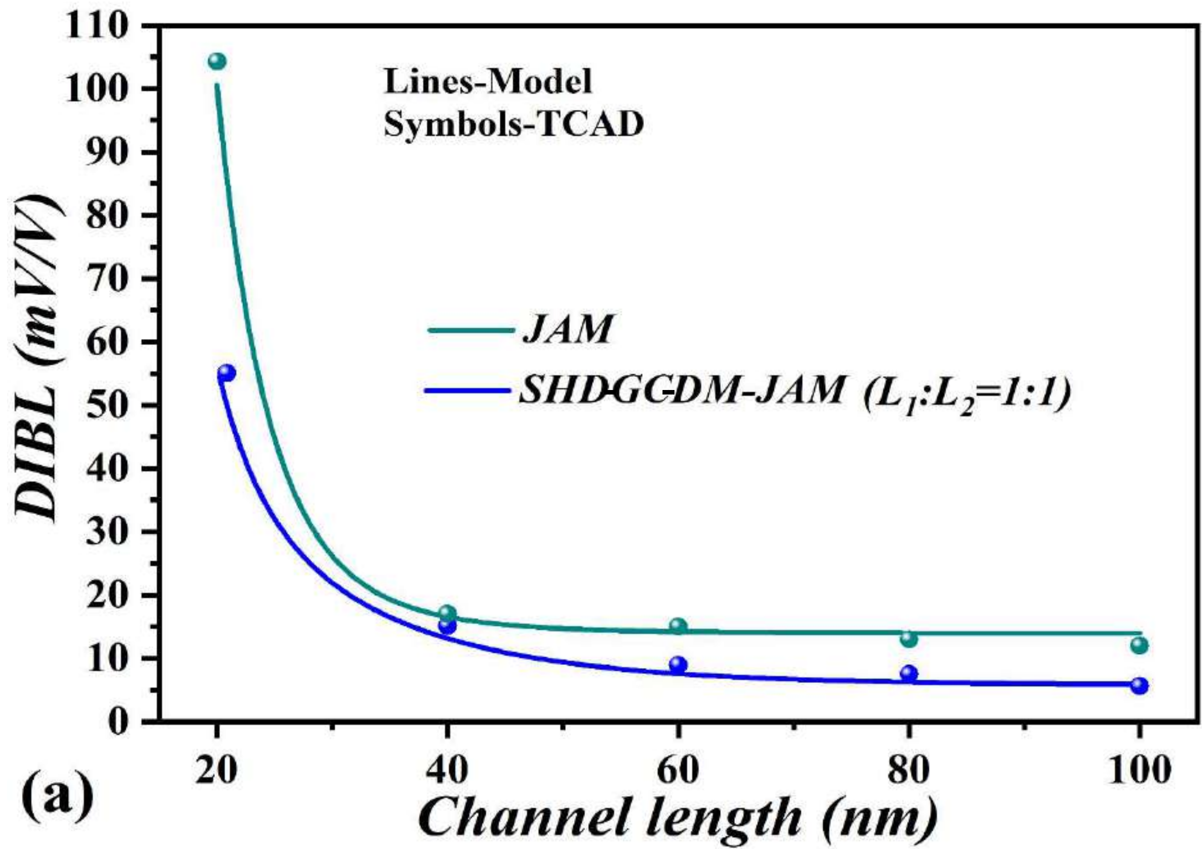

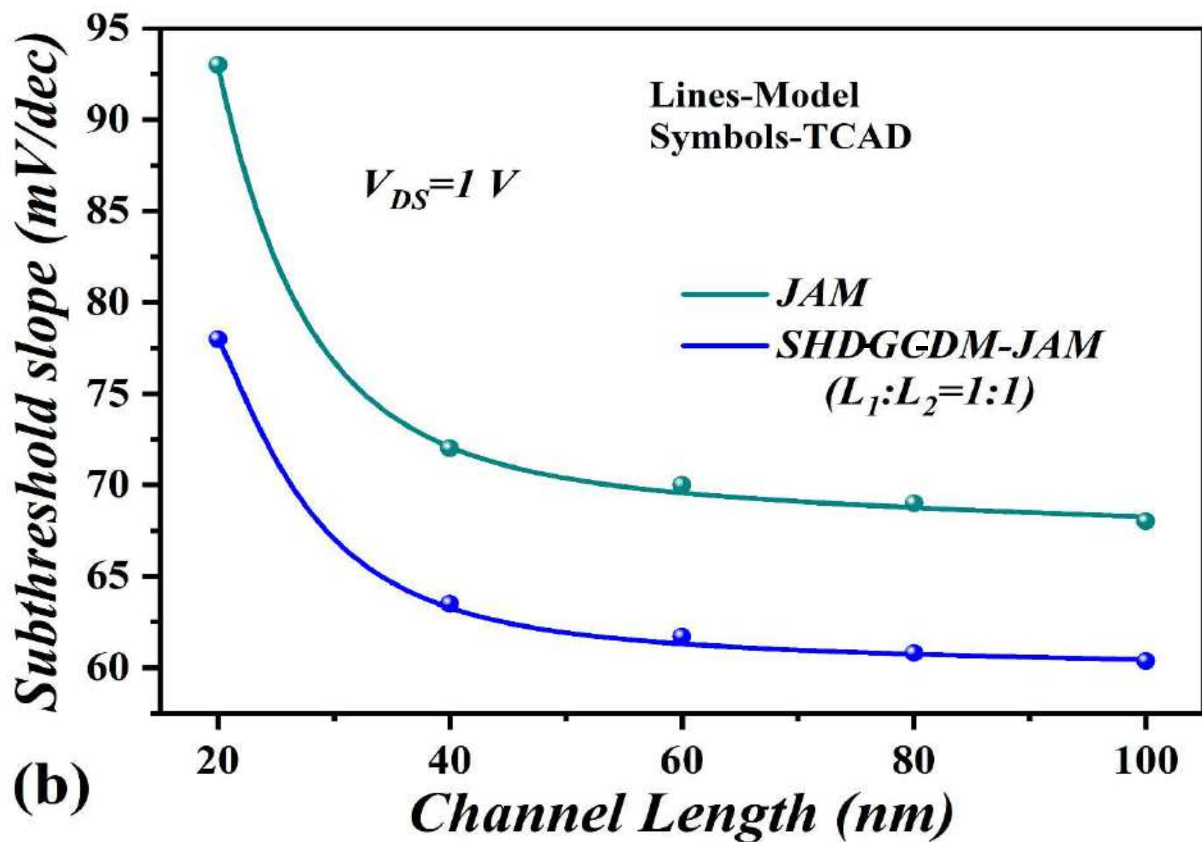

Fig. 4.9: (a) DIBL (b) SS (V_{DS}=1 V; R=1 nm); vs channel lengths for JAM and SHD-GC-DM-JAM.

increase with L_1:L_2 (Goel *et al.*, 2016b). Thus, for further comparisons, we have optimized L_1:L_2 to 1:1. Fig. 4.5(a) and (b) shows that the value of minimum central potential is greater and shifted towards the source side for SHD-GC-DM-JAM, therefore SHD-GC-DM-JAM has higher immunity towards SCEs. Fig. 4.5 (c) and (d) demonstrates SHD-GC-DM-JAM has a higher electric field at the source side and lower at the drain side (even at the high drain and low gate voltage), thus it is faster and less vulnerable to HCEs (Pratap *et al.*, 2014b). Fig. 4.6(a) shows the continuity of central potential with V_{GS} at z=L/2 for both JAM and SHD-GC-DM-JAM with our proposed model. From fig. 4.6(b) it could be observed that with the decrease of radius R (width) the value of minimum central potential increases (source-channel barrier) negatively for all V_{GS}. Therefore, SCEs decrease with an increase in R. Fig. 4.7(a) and (b) demonstrates that threshold voltage is higher and roll-off is lower for the SHD-GC-DM-JAM. Moreover roll-offs decrease with a reduction in R and almost negligible for R=3 nm (narrow channel effect). Fig. 4.8(a) shows that I_{ON} is higher for SHD-GC-DM-JAM at all V_{GS}. Further, it could also be observed that GIDL is least for SHD-GC-DM-JAM as BTBT width is largest for the device (inset). Fig. 4.8(b) shows a decrease in I_{ON} and V_{th} with an increase in temperature due to a decrease in μ and E_g. Fig. 4.8(c) and (d) show the modeling of I_D-V_{DS} (for different V_{GS}) and g_m, g_d respectively. It could be observed that both I_D, g_m and g_d are higher for SHD-GC-DM-JAM, thus better for analog performance. Fig. 4.9(a) and (b) shows both DIBL and SS are lower for SHD-GC-DM-JAM. Fig 4.10 shows the effect of positive and negative interface trapped charges (±ITC) at the oxide interface due to the high field and HCEs at the drain end of the channel (Pratap *et al.*, 2015; Kumar *et al.*, 2016). Fig. 4.10(a) shows that the difference between the values of minimum potential depth with ±ITC is higher and also shifted towards the drain side for JAM. Fig. 4.10(b) and (c) show that the threshold voltage variability with ±ITC density is higher for JAM. Fig 4.10(d) shows I_{ON}/I_{OFF} variability is larger for JAM

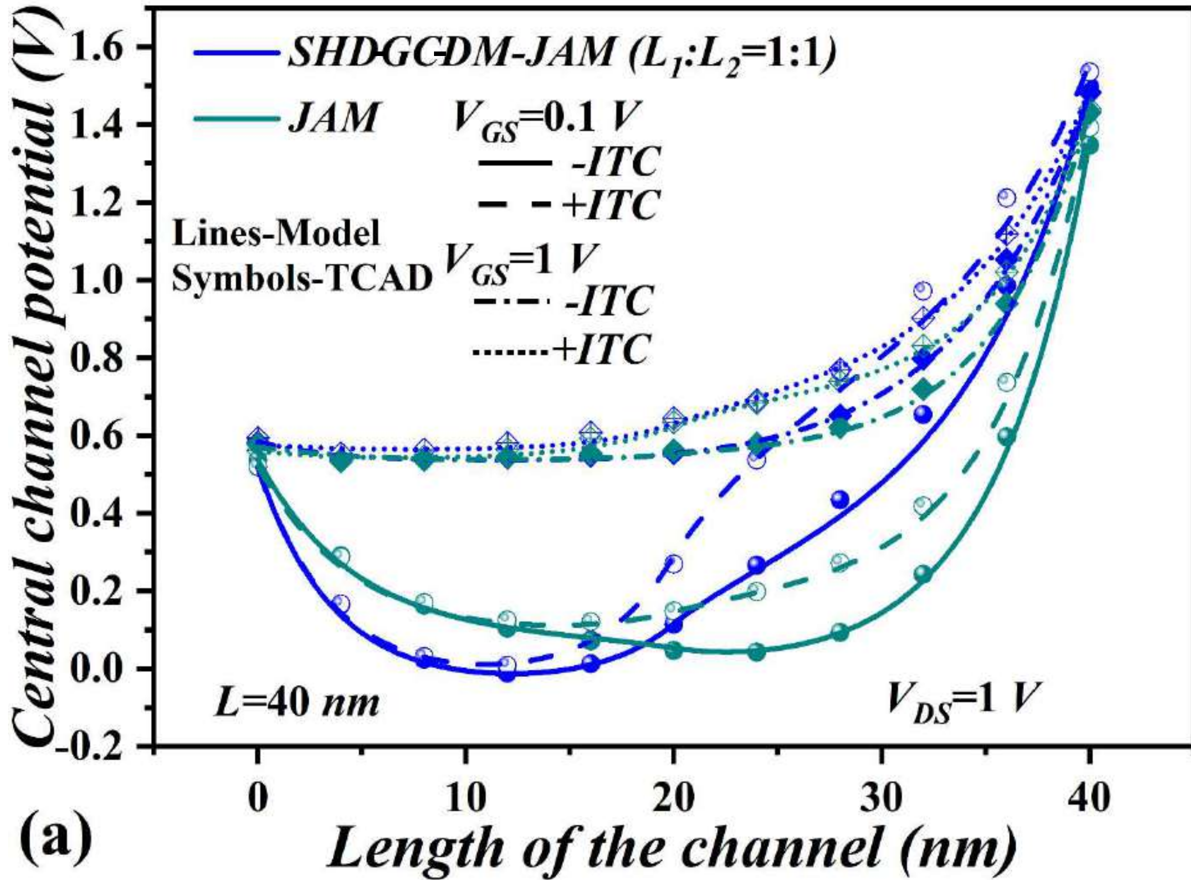
SHDGCDM-JAM (L_1:L_2=1:1)
JAM
V_{GS}=0.1 V
-ITC
+ITC
Lines-Model
Symbols-TCAD
V_{GS}=1 V
-ITC
+ITC
L=40 nm
V_{DS}=1 V
Central channel potential (V)
Length of the channel (nm)
(a)

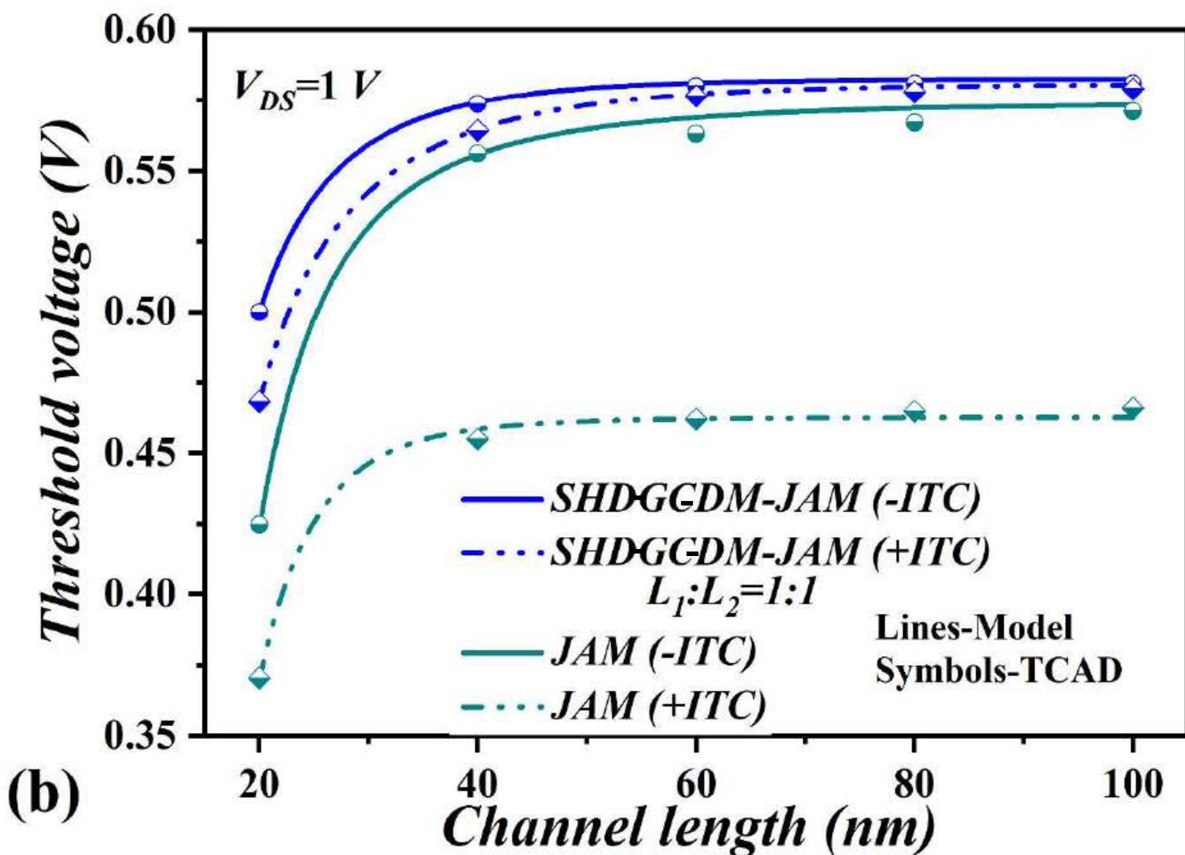
V_{DS}=1 V
SHDGCDM-JAM (-ITC)
SHDGCDM-JAM (+ITC)
L_1:L_2=1:1
JAM (-ITC)
JAM (+ITC)
Lines-Model
Symbols-TCAD
Threshold voltage (V)
Channel length (nm)
(b)

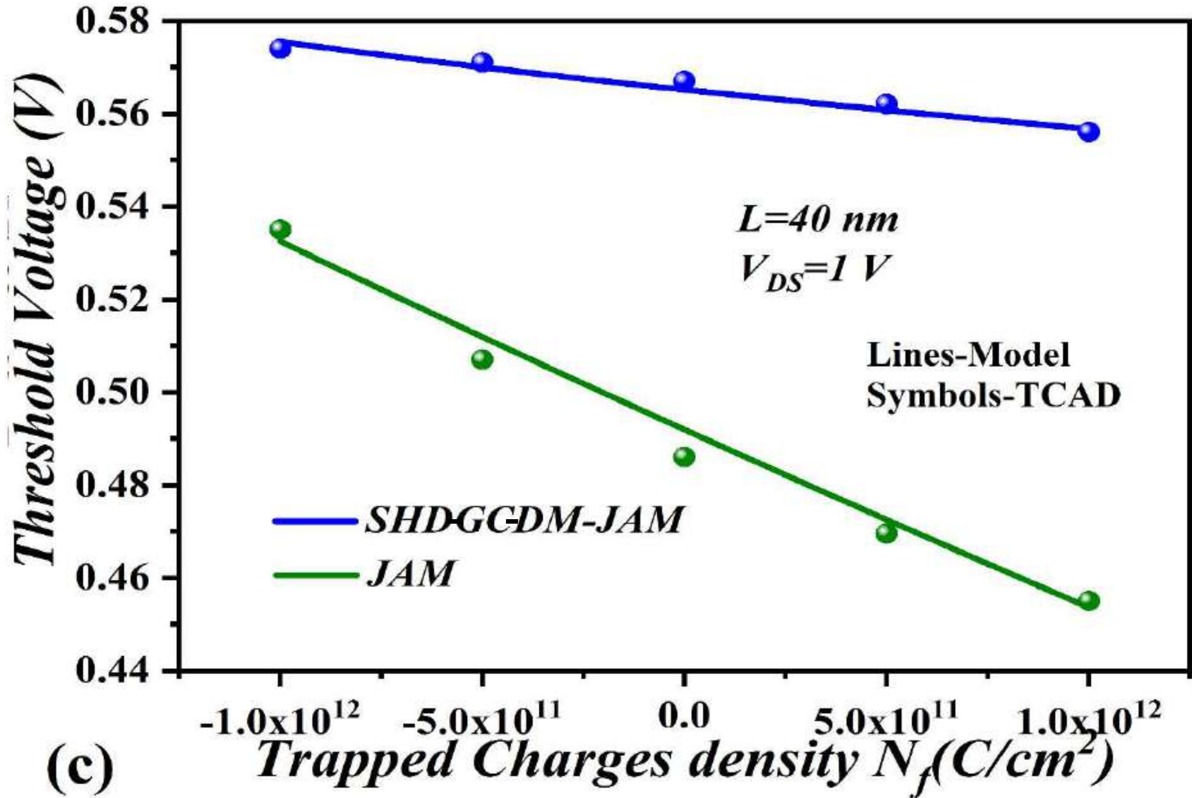

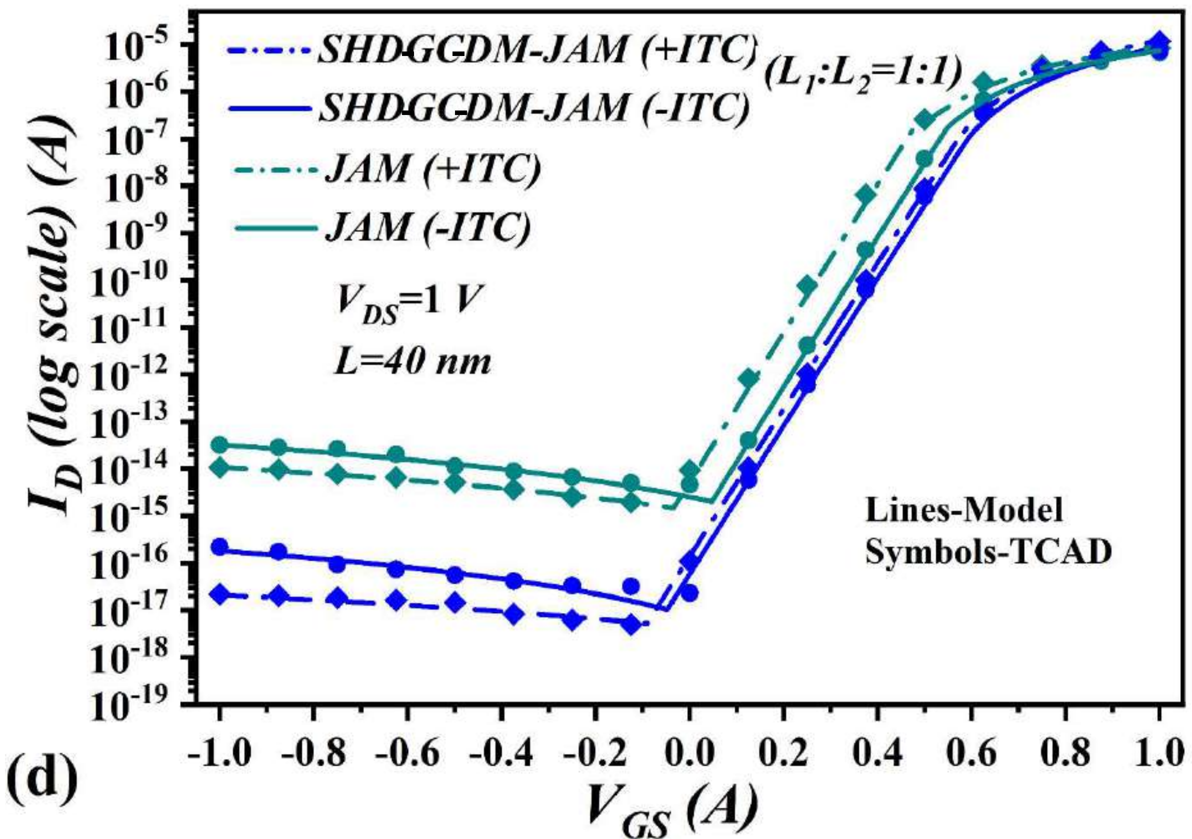

Fig. 4.10: (a) Central potential vs length of the channel at (V_{GS}=0.1 and 1 V) (b) Threshold voltage (c) threshold voltage vs trapped charges density (d) I_D (log scale) vs V_{GS}; at V_{DS}=1 V for SHD-GC-DM-JAM and JAM MOSFET with ± interface trapped charges at R_2.

with ±ITC. Thus CG-SHD-GC-DM-JAM is more immune to the effect of trapped oxide charges at the oxide interface.

The above discussions related to various results demonstrates that the engineered CG-SHD-GC-DM-JAM MOSFET structure shows better electrical characteristics and immunity to both the SCEs and interface trapped charges over the conventional JAM MOSFETs. The proposed model results match well with numerical simulation data thereby validating the analytical results. The proposed model also captures the variation of various DC electrical characteristics with length, radius, temperature, and trapped charges for JAM and engineered

JAM devices. Therefore, a full DC compact model for various JAM MOSFETs could be implemented with our proposed analytical model.

4.5 Conclusion

A 2-D continuous potential based compact DC model for short-channel CG-SHD-GC-DM JAM MOSFET has been proposed in this chapter for all possible operating regimes of the device. The threshold voltage, roll-off, drain current (including GIDL), DIBL and SS have also been formulated from the potential model. The model could also be extended for modeling the potential of device engineered inversion mode MOSFETs. Our proposed CG-SHD-GC-DM JAM structure has improved DC electrical characteristics and better immunity to interface trapped charges over the conventional JAM MOSFETs. However, the proposed model has assumed negligible depletion width in the source/drain extension region. The model is valid for the channel doping below or equal to $10^{19}/cm^3$ above which the series in Eq. 4.40 does not converge. Our proposed model can also be extended for any other engineered IM MOSFETs with suitable modifications.

A Unified 2-D Compact Quasi-Ballistic Model for CG- JAM and Inversion Mode MOSFET

5.1 Introduction

The ballistic transport phenomenon of channel carriers increases with the decrease in the gate length in the sub-40 nm regime. A fraction of channel carriers may then travel without undergoing through inelastic scattering (Curatola, Fiori and Iannaccone, 2004). As a result, the classical drift-diffusion transport model may not be valid and hence a quasi-ballistic transport model is required to describe the transport phenomenon of the carriers particularly when the channel length is equivalent to mean free career path (Natori, 2008). The quasi-ballistic transport models have been reported by many researchers for the conventional undoped inversion mode (IM) MOSFETs as discussed in Chapter-1 (Curatola, Fiori and Iannaccone, 2004; Fuchs *et al.*, 2005; Tsuchiya *et al.*, 2006; Martinie, Le Carval, *et al.*, 2008; Dura *et al.*, 2011), (Hoon, 2003). Huang *et. al.* proposed a surface potential based quasi-ballistic transport velocity model for IM MOSFETs (Huang *et al.*, 2015) but the proposed 2-D potential model was not continuous between the depletion and inversion regimes of operation. A complex quasi-2-D potential model was reported by Liu et al. (Liu and Li, 2012) for the cylindrical gate (CG) IM MOSFET. A unified model was proposed by Xiaoshi *et al.* (X. Jin *et al.*, 2013) proposed for both the DG JAM MOSFET and IM DG MOSFET. However, their proposed model was based on the 1-D potential function and hence is not fit for short-channel MOSFETs. In the previous chapter (i.e. Chapter-4), a DC compact model is presented for the JAM MOSFETs without considering the ballistic transport phenomenon. In the present chapter, we have attempted to develop a simple and unified 2-D continuous potential model for obtaining a surface potential based quasi-ballistic drain current model supporting both the JAM MOSFET

and IM MOSFET. We have considered a uniform channel doping in the JAM MOSFET to maintain the similarity of the analysis with the IM MOSFETs. The outline of the chapter is given below:

Section 5.2 presents a unified 2-D analytical model for CG JAM and IM MOSFET. A brief description of simulation setup is discussed in Sec. 5.3. Some important model results and related discussions have been presented in Sec. 5.4. Finally, Sec. 5.5 presents the major observations of the present chapter.

5.2 Formulation of the 2-D analytical model

In this present model channel length below 10 nm and radius below 5 nm have not been considered due to the complexity of quantum confinement effects. Potential in a cylindrical gate structure is invariable with θ. Considering the potential inside the channel region with length L be $\psi(r,z)$ with the doping of N_{ch}. Thus, the 2-D potential distribution $\psi(r,z)$ in the channel region can be obtained by solving the following Poisson's equations:

$$\frac{d^2\psi(r,z)}{dz^2}+\frac{1}{r}\frac{d}{dr}r\frac{d\psi(r,z)}{dr}=-\frac{qN_{ch}}{\varepsilon_{Si}}\left[1-exp\left[\frac{\psi(r,z)-V_f}{V_T}\right]\right] \text{ for JAM}$$

$$\frac{qN_{ch}}{\varepsilon_{Si}}\left[1-\left(\frac{ni}{N_{ch}}\right)^2 exp\left[\frac{\psi(r,z)-V_f}{V_T}\right]\right] \text{ for MOSFET} \quad (5.1)$$

where thermal voltage V_T = 0.0259 V and the quasi-fermi level for the channel region is given by V_f. Which is given by $V_f = V_T\, ln\left({N_{ch}}/{ni}\right)$ where ni is the intrinsic concentration (Li *et al.*, 2013). On application superposition principle to solve the unified Poisson's equation (5.1) for MOSFET and JAM by splitting them into 1-D Poison's equation, $\phi(r)$ and 2-D Laplace's equation, $\nu(r,z)$ and can be formulated as (El Hamid, Iñíguez and Roig Guitart, 2007; Ray and Mahapatra, 2008; Li *et al.*, 2013; Huang *et al.*, 2015; Trivedi *et al.*, 2016; Bae and Yun, 2019).

$$\psi(r,z)=\nu(r,z)+\phi(r) \quad (5.2)$$

$\frac{1}{r}\frac{d}{dr}\left(r\frac{d\phi(r)}{dr}\right) = \frac{qN_{ch}}{\varepsilon_{Si}}\left[1 - \left(\frac{ni}{N_{ch}}\right)^2 exp\left[\frac{\phi(r) - V_f}{V_T}\right]\right]$ for MOSFET

$= -\frac{qN_{ch}}{\varepsilon_{Si}}\left[1 - exp\left[\frac{\phi(r) - V_f}{V_T}\right]\right]$ for JAM, 1-D Poisson's equation (5.3)

$\frac{d^2 v(r,z)}{dz^2} + \frac{1}{r}\frac{d}{dr} r \frac{dv(r,z)}{dr} = 0$, 2-D Laplace equation (5.4)

Bandgap in silicon starts narrowing at doping of 10^{17} /cm^3. Since a doping level of $\geq 10^{17}$/cm^3 is considered, we have included the equations of bandgap narrowing in this present article.

$$\Delta E_g = \beta_E\left(ln(N_{ch}/\beta_N) + \sqrt{ln(N_{ch}/\beta_N)^2 + \beta_C}\right) \tag{5.5}$$

$$E_g^{eff} = E_g - \Delta E_g \tag{5.6}$$

$$\chi^{eff} = \chi + \Delta E_g/2 \tag{5.7}$$

where, $\beta_E = 6.92 \times 10^{-3}$eV, $\beta_N = 1.3 \times 10^{17}$cm^{-3}and $\beta_C = 0.5$ are some empirical

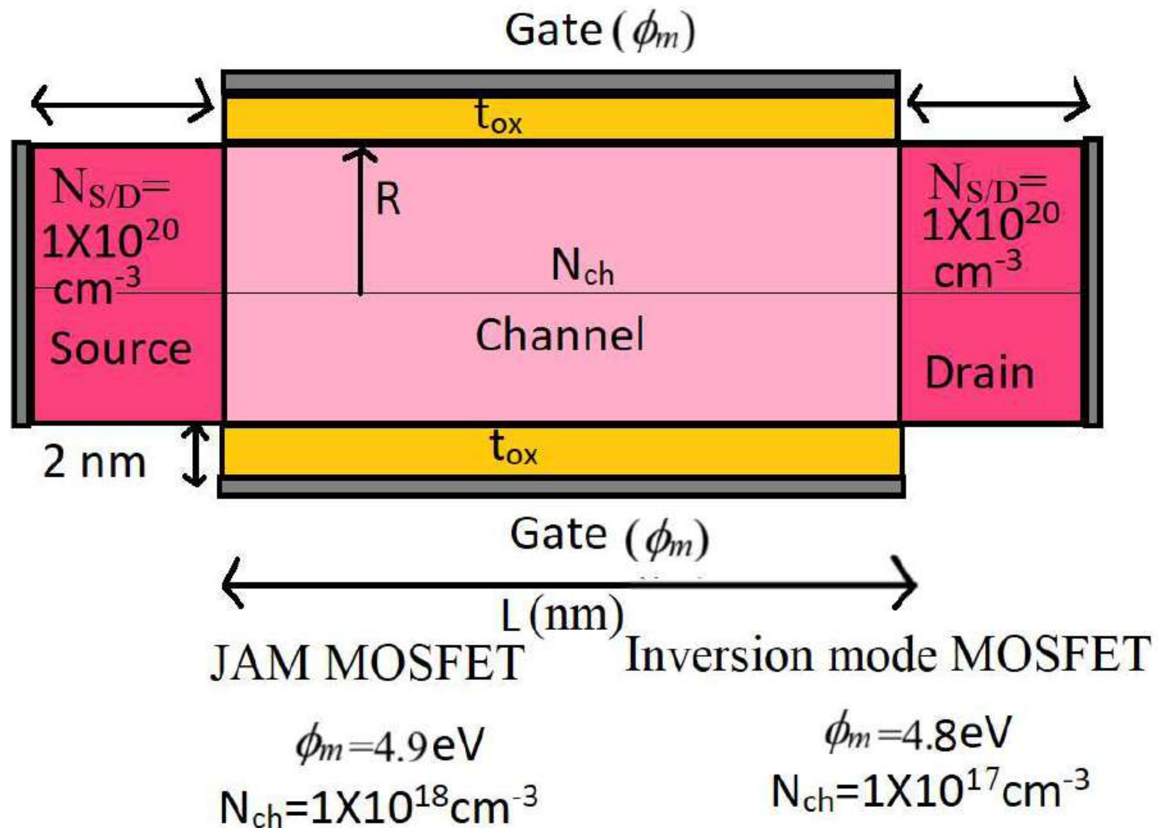

Fig. 5.1: A cross-sectional view of JAM and inversion mode MOSFET.

constants at room temperature, E_g and χ are the energy bandgap and electron affinity, E_g^{eff} and χ^{eff} are the effective energy bandgap and electron affinity of the Si inside the channel after integrating the model described by (5.5), (5.6) and (5.7) in the channel region (Huang *et al.*, 2015; Trivedi *et al.*, 2016).

5.2.1 The solution of 1-D Poisson's equation

Assuming the JAM and MOSFET to be undoped the initial solution for undoped approximation be [9]-[15]

$$\phi(r) = V_f + V_T ln\left(\frac{8(1-\gamma)V_T\epsilon_{Si}}{qN_{ch}(R^2-(1-\gamma)r^2)^2}\right) \text{ for JAM}$$

$$V_f + V_T ln\left(\frac{8(1-\gamma)V_T\epsilon_{Si}}{q^{ni^2}/_{N_{ch}}(R^2-(1-\gamma)r^2)^2}\right) \text{for MOSFET} \quad (5.8)$$

Where, V_f and V_T are quasi-fermi level and thermal voltage whose expressions are given before. R is the radius of the cylindrical device, ni and N_{ch} are the intrinsic fermi level and channel doping of the device respectively. γ is a constant whose value could be extracted from (5.8) as (Jiménez *et al.*, 2004; Yu *et al.*, 2007).

In all expressions throughout the manuscript, the upper row of signs is for MOSFET and the lower row is for JAM respectively.

Now proceeding as (Lee *et al.*, 2013; X. Jin *et al.*, 2013; X. S. Jin *et al.*, 2013) and substituting (5.8) back into (5.3) we get

$$\frac{d^2\phi(r)}{dr^2} + \frac{1}{r}\frac{d\phi(r)}{dr} = \frac{q}{\epsilon_{Si}}\left[\pm N_{ch} \mp \left(\frac{8V_T\epsilon_{Si}}{qR^2}\right)\left(\frac{\alpha}{1-\alpha^2r^2/_{R^2}}\right)^2\right] \quad (5.9)$$

Where $1-\gamma = \alpha^2$

The value of α could be extracted implicitly from (8) as (Yu *et al.*, 2007). The value lies as $0 < \alpha \ll 1$ as (Yu *et al.*, 2007).

Solving (9) as [14]-[15] we get

$$\phi(r) = \pm\frac{qN_{ch}r^2}{4\epsilon_{Si}} \mp 2V_T ln\left(1-\frac{\alpha^2r^2}{R^2}\right) + C \quad (5.10)$$

where C is constant. The boundary conditions needed to solve (5.10) are

$$\left.\frac{d\phi(r)}{dr}\right|_{r=0} = 0 \tag{5.11}$$

$$C_{ox}\left(V_{GS} - V_{fb} - \phi(R)\right) = -\epsilon_{Si}\left.\frac{d\phi(r)}{dr}\right|_{r=R} \tag{5.12}$$

$$\text{where, } V_{fb} = \phi_m - \phi_s, \phi_s = \chi^{eff} + {E_g^{eff}}/{2q} - V_f \tag{5.13}$$

$$C_{ox} = {\epsilon_{ox}}/{t_{ox}}, t_{ox} = Rln\left(1 + {t_{ox}}/{R}\right) \tag{5.14}$$

$$\phi(R) = \pm\frac{qN_{ch}R^2}{4\epsilon_{Si}} \mp 2V_T ln(1-\alpha^2) + C \tag{5.15}$$

From (5.10)-(5.15) we get

$$C = V_{GS} - V_{fb} \mp \frac{qN_{ch}R^2}{4\epsilon_{Si}} \pm \frac{qN_{ch}R}{2C_{ox}} \mp \frac{4V_T\epsilon_{Si}\alpha^2}{RC_{ox}(1-\alpha^2)} \pm 2V_T\ln(1-\alpha^2) \tag{5.16}$$

From (10) and (16)

$$\phi(r) = \pm\frac{qN_{ch}(r^2-R^2)}{4\epsilon_{Si}} \mp 2V_T ln\left(1 - \frac{\alpha^2 r^2}{R^2}\right) + V_{GS} - V_{fb} \pm \frac{qN_{ch}R}{2C_{ox}} \mp \frac{4V_T\epsilon_{Si}\alpha^2}{RC_{ox}(1-\alpha^2)}$$

$$\pm 2V_T\ln(1-\alpha^2) \tag{5.17}$$

5.2.2 The solution of 2-D Laplace's equation

Utilizing the variable separation method, the solution of (5.4) could be obtained as (El Hamid, Iñíguez and Roig Guitart, 2007; Ray and Mahapatra, 2008; Li *et al.*, 2013; Pratap *et al.*, 2014; Trivedi *et al.*, 2016; Rewari *et al.*, 2017). We get

$$v(r,z) = \sum_1^{\infty} J_0\left(\frac{\beta_n r}{R}\right)\left[C_n e^{\beta_n z/R} + D_n e^{-\beta_n z/R}\right] \tag{5.18}$$

where C_n and D_n are constants whose values are determined by boundary conditions given below

$$\epsilon_{Si}\left.\frac{dv(r,z)}{dr}\right|_{r=R} = C_{ox}v(r,z) \tag{5.19}$$

$$\psi(r,0) = V_{bi} \text{ and } \psi(r,L) = V_{bi} + V_{DS} \tag{5.20}$$

Where $V_{bi} = V_T \ln\left(\frac{N_{S,D}}{N_{ch}}\right)$ for JAM and

$$V_{bi} = V_T \ln\left(\frac{N_{S,D}N_{ch}}{ni^2}\right) \text{ for MOSFET} \tag{5.21}$$

From (5.18) and (5.19) we get the value of eigenvalue β obtained by the expression

$$J_0(\beta_n) = -\frac{\epsilon_{Si}\beta_n}{C_{ox}R} J_1(\beta_n) \tag{5.22}$$

From (5.18) and using the boundary condition of (5.20) we get

$$\sum_1^\infty J_0\left(\frac{\beta_n r}{R}\right)\left[C_n e^{\beta_n L/R} + D_n e^{-\beta_n L/R}\right] = V_{bi} + V_{DS} - \phi(r) \tag{5.23}$$

$$\sum_1^\infty J_0\left(\frac{\beta_n r}{R}\right)[C_n + D_n] = V_{bi} - \phi(r) \tag{5.24}$$

Now multiplying (5.23) and (5.24) with factor $\int_0^R \frac{\beta_n r}{R} J_0\left(\frac{\beta_n r}{R}\right) d\left(\frac{\beta_n r}{R}\right)$ to negate the summation sign, we get

$$C_n e^{\beta_n L/R} + D_n e^{-\beta_n L/R} = (A + V_{bi} + V_{DS})\frac{w}{u} + B\frac{y}{u} \tag{5.25}$$

$$C_n + D_n = (A + V_{bi})\frac{w}{u} + B\frac{y}{u} \tag{5.26}$$

$$\text{Where, } u = \int_0^R \frac{\beta_n r}{R} J_0^2\left(\frac{\beta_n r}{R}\right) d\left(\frac{\beta_n r}{R}\right) = \frac{\beta_n{}^2[J_0^2(\beta_n)+J_1^2(\beta_n)]}{2} \tag{5.27}$$

$$w = \int_0^R \frac{\beta_n r}{R} J_0\left(\frac{\beta_n r}{R}\right) d\left(\frac{\beta_n r}{R}\right) = \beta_n J_1(\beta_n) \tag{5.28}$$

$$y = \int_0^R \left(\frac{\beta_n r}{R}\right)^3 J_0\left(\frac{\beta_n r}{R}\right) d\left(\frac{\beta_n r}{R}\right) = \beta_n J_1(\beta) - 2J_2(\beta_n) \tag{5.29}$$

Where J_0 and J_1 are Bessel's function of order 0 and 1 respectively. Therefore, constants C_n and D_n could be expressed as

$$\begin{bmatrix} C_n \\ D_n \end{bmatrix} = \frac{1}{\Delta}\begin{bmatrix} e^{-\beta_n L/R} & -1 \\ -e^{\beta_n L/R} & 1 \end{bmatrix}\begin{bmatrix} P_{11} \\ P_{12} \end{bmatrix} \tag{5.30}$$

Where $\Delta= -2sinh\left({}^{\beta_n L}/{}_{R}\right)$ (5.31)

Where $P_{11} = \frac{w}{u}(A + V_{bi}) + \frac{y}{u}(B)$ and (5.32)

$P_{12} = \frac{w}{u}(A + V_{bi} + V_{DS}) + \frac{y}{u}(B)$ (5.33)

$A = \mp \frac{qN_{ch}R^2}{4\epsilon_{Si}} + V_{GS} - V_{fb} \pm \frac{qN_{ch}R}{2C_{ox}} \mp \frac{4V_T\epsilon_{Si}\alpha^2}{RC_{ox}(1-\alpha^2)} \pm 2V_T \ln(1-\alpha^2)$ (5.34)

Since $\ln\left(1 - \frac{\alpha^2 r^2}{R^2}\right) = -\frac{\alpha^2 r^2}{R^2} - \frac{(\alpha^2)^2}{2}\left(\frac{r^2}{R^2}\right)^2 \dots = -\frac{\alpha^2 r^2}{R^2}$ (5.35)

neglecting higher values from condition $0 < \alpha \ll 1$. Therefore

$B = \pm\left[\frac{qN_{ch}R^2}{4\epsilon_{Si}} + 2V_T\alpha^2\right]$ (5.36)

5.2.3 Threshold voltage formulation

A very important parameter for JAM as well as inversion MOSFET is threshold voltage (V_{th}). It is defined as the gate-source (V_{GS}) voltage, where the minimum central potential is equal to fermi potential for JAM (Gupta, 2015) and the minimum surface potential equal to twice the Fermi potential for inversion MOSFET (Pratap *et al.*, 2014). By evanescent mode analysis of the above Fourier Bessel's series. The position of minimum central/surface potential could be obtained by solving

$\left.\frac{d\psi(r,z)}{dz}\right|_{r=0/R,\ z=z_{min}} = 0, z_{min} = \frac{R}{2\beta_n} ln\left(\frac{D_n}{C_n}\right)$ (5.37)

From (5.2), (5.18) and (5.31) we get the equation

$\phi(r) + 2\delta\sqrt{C_n D_n}\Big|_{r=0/R,\ V_{gs}=V_{th}} = \varphi_0$ (5.38)

Where $\varphi_0 = V_f, 2V_f$ and $\delta = 1, J_0(\beta_n)$ for JAM and inversion MOSFET respectively.

Now $C_n D_n = G_1 V_{th}^2 + G_2 V_{th} + G_3$ (5.39)

$G_1 = M_{11}M_{12}, G_2 = M_{11}N_{12} + N_{11}M_{12}$ and $G_3 = N_{11}N_{12}$ (5.40)

$$M_{11} = \frac{1}{\Delta}\frac{w}{u}\left(e^{-\beta_n L/R} - 1\right) \tag{5.41}$$

$$N_{11} = \frac{1}{\Delta}\left\{\left[(E_{11} + V_{bi})\frac{w}{u} + \frac{y}{u}B\right]\left(e^{-\beta_n L/R} - 1\right) - \frac{w}{u}V_{DS}\right\} \tag{5.42}$$

$$M_{12} = \frac{1}{\Delta}\frac{w}{u}\left(1 - e^{\beta_n L/R}\right) \tag{5.43}$$

$$N_{11} = \frac{1}{\Delta}\left\{\left[(E_{11} + V_{bi})\frac{w}{u} + \frac{y}{u}B\right]\left(1 - e^{\beta_n L/R}\right) + \frac{w}{u}V_{DS}\right\} \tag{5.44}$$

Where $E_{11} = A - V_{GS}$ (5.45)

Now threshold voltage is given by expression-

$$\sigma_1 V_{th}^2 + \sigma_2 V_{th} + \sigma_3 \text{ and } V_{th} = \frac{-\sigma_2 \pm \sqrt{\sigma_2^2 - 4\sigma_1\sigma_3}}{2\sigma_1} \tag{5.46}$$

$$\sigma_1 = 4\delta^2(G_1) - 1, \sigma_2 = 4\delta^2 G_2 + 2(A_{11} - \varphi_0) \text{ and } \sigma_3 = 4\delta^2 G_3 + (A_{11} - \varphi_0)^2 \tag{5.47}$$

Where $A_{11} = \phi(r)|_{r=0/R} - V_{Gs}$ (5.48)

In (5.46) only the positive value of threshold voltage is considered. Threshold voltage roll-off may be defined as the threshold voltage variation between long and short channel device and expressed as (Pratap *et al.*, 2014)

$$V_{roll-of} = V_{th}|_{short-channel} - V_{tL}, V_{tL} = A_{11} - \varphi_0 \tag{5.49}$$

5.2.4 Formulation of DIBL

Drain induced barrier lowering (DIBL) is defined as the difference in minimum central/surface potential for both devices and expressed as (Li *et al.*, 2013; Bae and Yun, 2019).

$$DIBL = -\frac{V_{th}|_{V_{DS}=0.05\text{V}} - V_{th}|_{V_{DS}=1\text{V}}}{V_{DS}(0.05\text{V}) - V_{DS}(1\text{V})} \times 10^3 \text{ V/V} \tag{5.50}$$

5.2.5 Drain current modeling

From Lundstrom's theory, current in a MOS device can be expressed as the product of quasi-ballistic velocity and cross channel charge at any point throughout the channel (Hoon, 2003). Here the virtual source is taken at the top of the surface barrier. Taking into consideration the ballistic and scattering effect the drain current can be expressed as (Huang *et al.*, 2015).

$$I_D = Q \times Vel_0 \times BR \times Fili \times W \tag{5.51}$$

Where Vel_0 is an extracted parameter and represents ballistic velocity, Q is cross channel charge at virtual source, BR is the ballistic transport coefficient, $Fili$ is backscattering factor and W is the width of the channel. The total charge across the channel at any point along z can be expressed as

$$Q = q\int_0^R n(r,z)dr \tag{5.52}$$

where $n(r,z) = \omega exp\left(\frac{\psi(r,z)-V_f(z)}{V_T}\right)$ (5.53)

Where $\omega = N_{ch}$ and $\frac{ni^2}{N_{ch}}$ for JAM and inversion MOSFET respectively. At the virtual source, we can express the total charge can be expressed as (Ray and Mahapatra, 2008).

$$Q = q\omega exp\left(\frac{\psi(R/_2, z_{min})}{V_T}\right)R \tag{5.54}$$

Now drain current could be expressed as (Hoon, 2003; Curatola, Fiori and Iannaccone, 2004; Fuchs *et al.*, 2005; Tsuchiya *et al.*, 2006; Martinie, Le Carval, *et al.*, 2008; Martinie, Munteanu, *et al.*, 2008; Dura *et al.*, 2011; Huang *et al.*, 2015; Murnal and Vijaya, 2019)

$$I_D = Q \times Vel_0 \times BR \times Fili \times \pi r^2 \tag{5.55}$$

BR is the ballistic transport coefficient given by (Curatola, Fiori and Iannaccone, 2004; Fuchs *et al.*, 2005; Tsuchiya *et al.*, 2006; Huang *et al.*, 2015; Murnal and Vijaya, 2019)

$BR = \frac{1-r'}{1+r'}$, where r' depends on free carrier path (5.56)

$Fili$ is the backscattering factor expressed as (Taur, 2001; Huang *et al.*, 2015)

$$Fili = \frac{1-e^{-V_{DS}/V_T}}{1+BR\times e^{-V_{DS}/V_T}} \tag{5.57}$$

All extracted parameters are obtained from (Hoon, 2003; Huang *et al.*, 2015)

5.2.6 Modeling of transconductance (g_m) and output-conductance(g_d)

Transconductance (g_m) and output conductance (g_d) are important analog DC parameters an are given as (Yu *et al.*, 2007). The continuity of these parameters demonstrates the continuity of I_D-V_{DS} and I_D-V_{GS} curve.

$$g_m = \frac{\partial I_D}{\partial V_{GS}} \text{ and } g_d = \frac{\partial I_D}{\partial V_{DS}} \tag{5.58}$$

The derivatives are obtained at a constant drain voltage (V_{DS}) and gate voltage (V_{GS}) respectively.

5.3 Simulation setup and model validation

In the present section, we have calibrated our simulation setup and validated our model with various analytical models presented in the reported literatures. Most of the reported works have simulated their device with an M-C (Monte-carlo) simulator. Although the M-C simulator gives accurate results for quasi ballistic effects but is computationally expensive and takes a lot of time to simulate. Therefore, in our work, we have used a BTE (Boltzmann's transport equation) solver. The calibration of the simulation setup has been done by equating the simulation results with the experimental data of an already fabricated device structure. For post validation of the TCAD simulation setup, the results from our proposed analytical model will be validated by equating them with the simulation results in the succeeding section. Further, the extracted parameters are obtained from (Huang *et al.*, 2015) and are used to calibrate our TCAD model. 3-D TCAD tool from Cogenda (Cogenda, 2016) has been used for simulation and validation

of our modeled results. The various models used are *Fermi-Dirac*, *Philips* unified mobility, and *BGN* for high dopingcarrier statistics, mobility model, and bandgap narrowing inside the device, respectively. Vel_0 and free carrier path are the extracted parameters obtained from (Huang *et al.*, 2015) and calibrated with models used for simulation. A list of various of extracted parameters are given in table 5.1.

Fig. 5.2 shows the calibration of the TCAD tool with experimental results and validation of our proposed model with various 2-D models for MOSFET and JAM reported in literatures. Fig 2(a) and (b) shows the calibration of the TCAD setup with experimental data of (Song *et al.*, 2006; Choi *et al.*, 2011). The I_D-V_{GS} curve is obtained at V_{DS}=1 V and 0.05 V in both linear and logarithmic scales for junctionless MOSFET in fig. 5.2(a). Fig. 5.2(b) shows I_D-V_{GS} curve for IM MOSFET obtained at V_{DS}=1 V and 0.1 V in logarithmic scale. Although there will considerable amount of quasi-ballistic transport effect in IM MOSFET device with channel length of 30 nm but very little for junctionless MOSFET for with a channel length of 50 nm. The analysis shows that the simulation results are well-matched with the experimental data. From fig 5.2(c) it is observed that the results of our proposed analytical model match with that of the analytical model proposed for IM MOSFET in (Liu and Li, 2012) and Junctionless MOSFET in (Li *et al.*, 2013). Further it could be noticed that not only our model matches well with sub-threshold potential but also super-threshold potential of (Liu and Li, 2012). This analysis validates our proposed analytical model against other reported literatures for not only sub-threshold but also super-threshold operations. Thus, not only do our simulation results match well with the experimental data but also our proposed analytical model matches well with various other reported models for both junctionless and IM MOSFET. Specification of various physical and geometrical parameters are given in table 5.2.

TABLE 5.1: List of various extracted parameters for simulation

Device Type	*N_{ch} (cm^{-3}) Doping*	*Channel Length (nm)*	*Vel_0 (cm/s)*	*Free carrier path (nm)*	*Channel radius (nm)*
JAM MOSFET	**10^{18}**	**20**	**1.04×10^{7}**	**21**	**5**
IM MOSFET	**10^{17}**	**20**	**1.15×10^{7}**	**23**	**5**

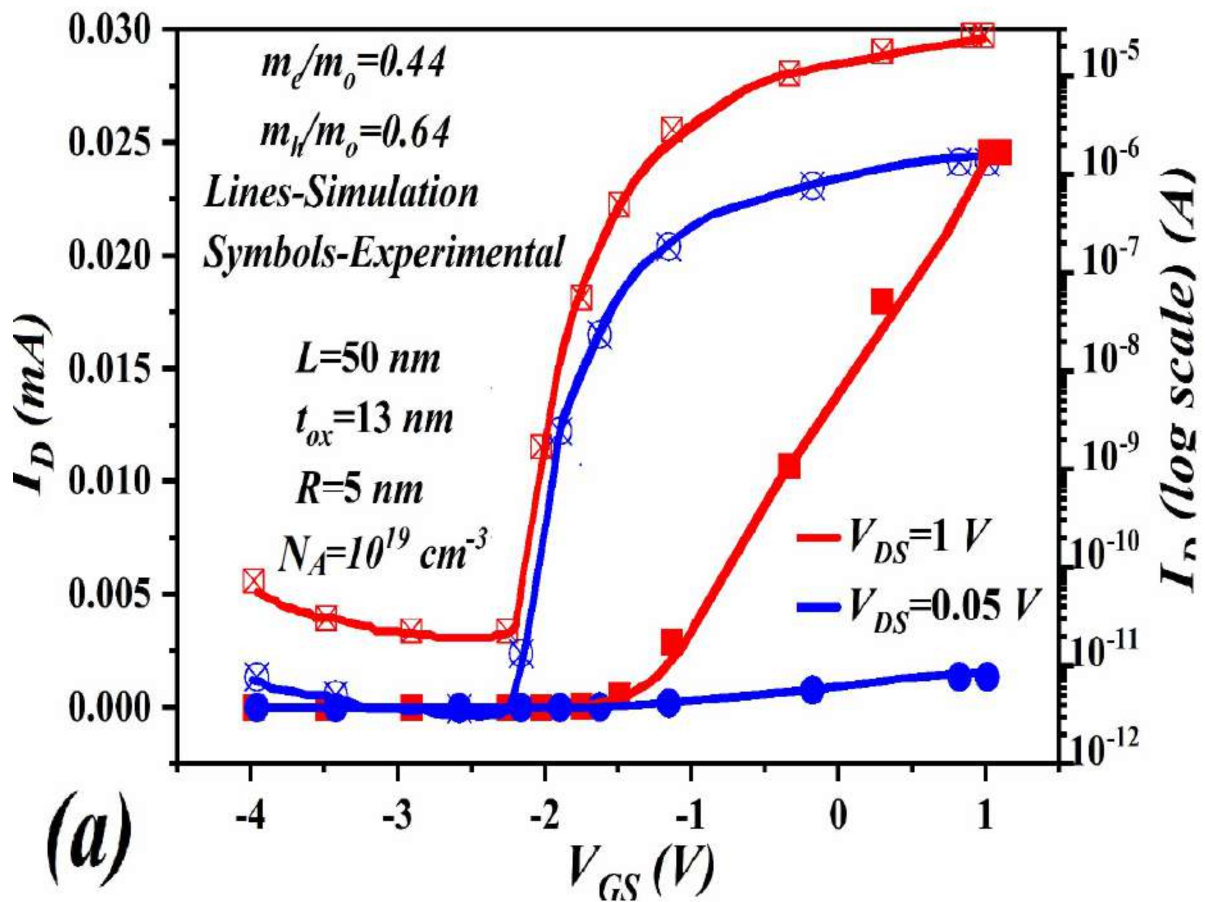

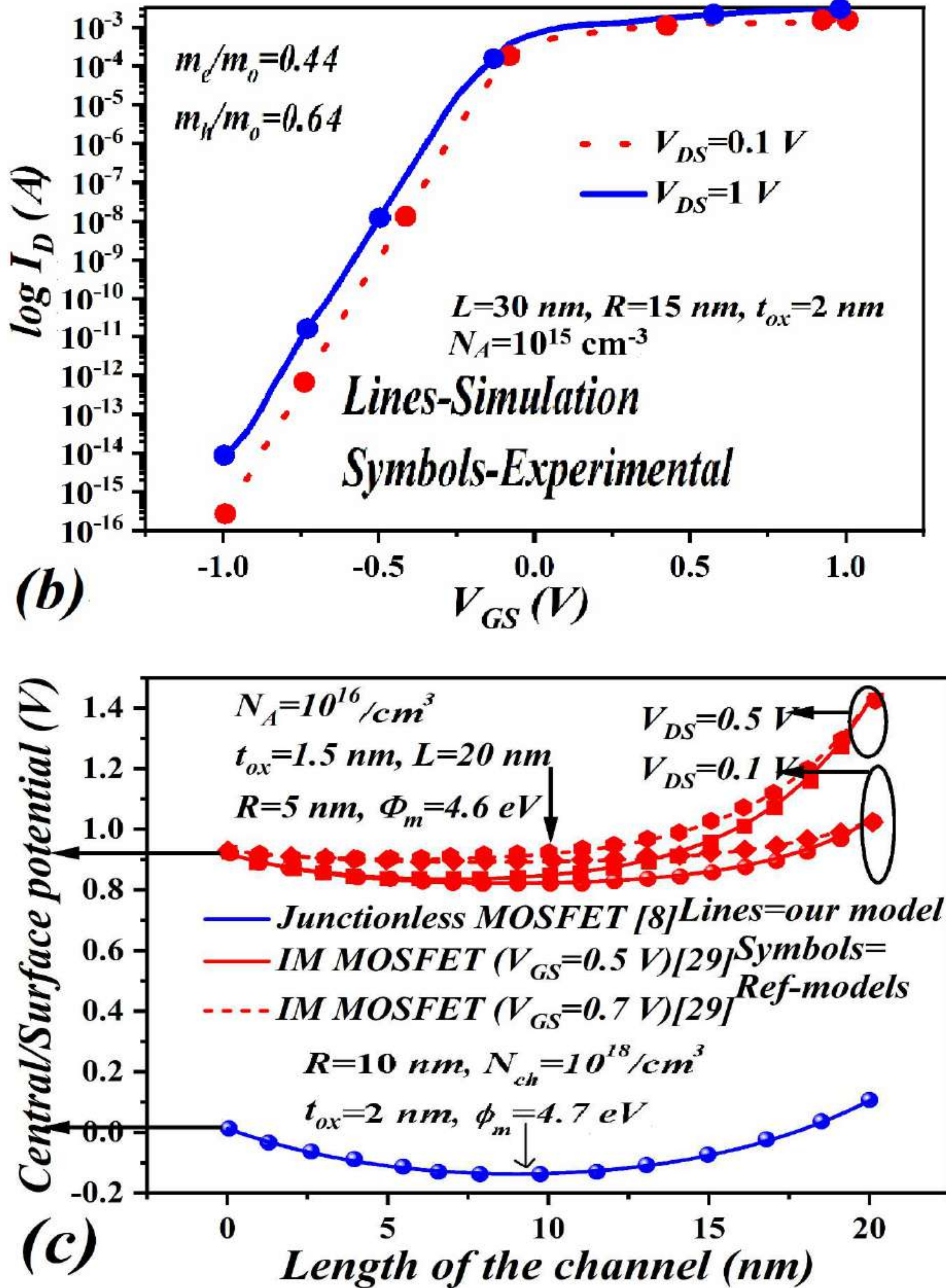

Fig. 5.2: Calibration of TCAD simulation setup with experimental results of, (a) junctionless MOSFET (Choi *et al.*, 2011), (b) IM MOSFET (Song *et al.*, 2006); (c) Validation of our proposed model with other reported 2-D models of junctionless MOSFET (Li *et al.*, 2013)[8] and IM MOSFET (Liu and Li, 2012)[29].

TABLE 5.2: Device physical and geometrical parameters

Device Type	*N_{ch} (cm^{-3})*	*Source /Drain doping (cm^{-3})*	*SiO_2/HfO_2 (nm)*	*Gate material workfunction (eV)*	*Channel length*
JAM MOSFET	**5×10^{17}- 5×10^{18}**	**10^{20}**	**1nm -3nm**	**4.9**	**10nm-40nm**
IM MOSFET	**5×10^{16}- 5×10^{17}**	**10^{20}**	**1nm-3nm**	**4.8**	**10nm-40nm**

5.4 Results and discussion

In this section, we have validated the results of our proposed analytical model with that of simulated data from the standard 3-D TCAD tool to verify the correctness of our proposed model. Further, a detailed physical analysis has also been made from the obtained results of JAM and IM MOSFET. The default oxide thickness is taken to be 2 nm unless otherwise mentioned. Since conduction in inversion MOSFET is through the surface and JAM MOSFET through the center. The central potential is highest for JAM MOSFET and the surface potential is highest for IM MOSFET. Further, minimum central/surface potential lies at the center of the channel (at z=L/2). Therefore, the continuity of these potentials with respect to V_{GS} is important from the perspective of a continuous model across all operating regimes. Fig. 5.3 shows the continuity of the middle surface and central potential with V_{GS} for both JAM and IM MOSFET. Fig 5.3 (a) shows the continuity of middle central potential (at z=L/2) of JAM and IM MOSFET with the variation of V_{GS} for V_{DS} =1 and 0.5 V at channel length of 40 nm. It could be noted that the middle central potential is continuous with V_{GS}. It could further be seen that the middle central potential increases with both V_{GS} and V_{DS} due to the increase of carriers in the channel and reduction of barrier height at higher voltages. Furthermore, it could also be observed that JAM has a higher depth of potential compared to IM MOSFET due to bulk mode of operation

of JAM MOSFET. Fig 5.3 (b) demonstrates the continuity of middle surface potential with the variation of V_{GS} at V_{DS}=1 V for a channel length of 20 nm. Since conduction in JAM is through bulk and in MOSFET is through the surface, the middle surface potential is higher for MOSFET than JAM. From the above analysis, it could be verified that our proposed analytical model is a continuous potential model with respect to V_{GS}. Fig 5.4 shows the variation of central channel potential along the length of the channel at V_{DS} =1 V and (a) V_{GS}=0 V, (b) V_{GS}=0.5 V for a channel length of 40 nm, 20 nm, and 10 nm. It could clearly be noted that the minimum central potential decreases with channel length for both JAM and inversion mode MOSFET. It is due to the decrease in barrier potential with shortening of channel length due to SCEs (short channel effects). Further, it could be inferred that the minimum central potential is higher for JAM than inversion mode MOSFET. Since conduction in inversion mode MOSFET is through the surface and for JAM through bulk (center of the channel). Fig 5.5 (a) shows the variation of central potential along the length of the channel for JAM and inversion mode MOSFET with a channel length of 10 nm, 20 nm, 40 nm at V_{DS}=1 V and V_{GS}=1 V. From fig 5.4 and fig 5.5 (a) it should be noted that the minimum central potential decreases with an increase in V_{GS}. This is because the energy barrier between the source and drain decreases due to an increase in V_{GS}, the carriers overcome this barrier and the device is in the on-state from off-state. Fig 5.5 (b) shows the variation of surface potential along the length of the channel at V_{DS}=1 V and V_{GS}=0, 0.5, 1 V with a channel length of 20 nm for all compared devices. It could be observed that minimum surface potential also decreases with an increase in V_{GS} due to the lowering of surface potential barrier with an increase in V_{GS}. Furthermore, it should also be noted that the minimum central/surface potential decreases with a decrease in channel length due to decrease of barrier with a decrease in channel length (SCEs). Fig 5.6 (a) shows the variation of central channel potential along the length of the channel at different radii. It could be observed that the minimum central channel potential decreases with an increase in radius. This may be attributed

to the fact that the source-channel barrier decreases with an increase in R. Further, the control of the gate decreases with an increase in the radius of the channel, thus the channel becomes less depleted of carriers, which also decreases its threshold voltage. Fig 5.6 (b) shows the variation of central channel potential along the length of the channel for different oxide thicknesses. It may be noted that the minimum central potential decreases with an increase in oxide thickness. It is because with an increase in oxide thickness the gate capacitance decreases which in turn decreases the control of the gate over the channel. Thus, the channel becomes less depleted with an increase in oxide thickness. This also reduces the energy barrier between source and channel. Fig. 5.6 (c) shows the change in central channel potential with doping variations for both JAM and IM MOSFET. It may be observed that central channel potential increases with increase in doping for IM MOSFET whereas for JAM MOSFET it reduces with

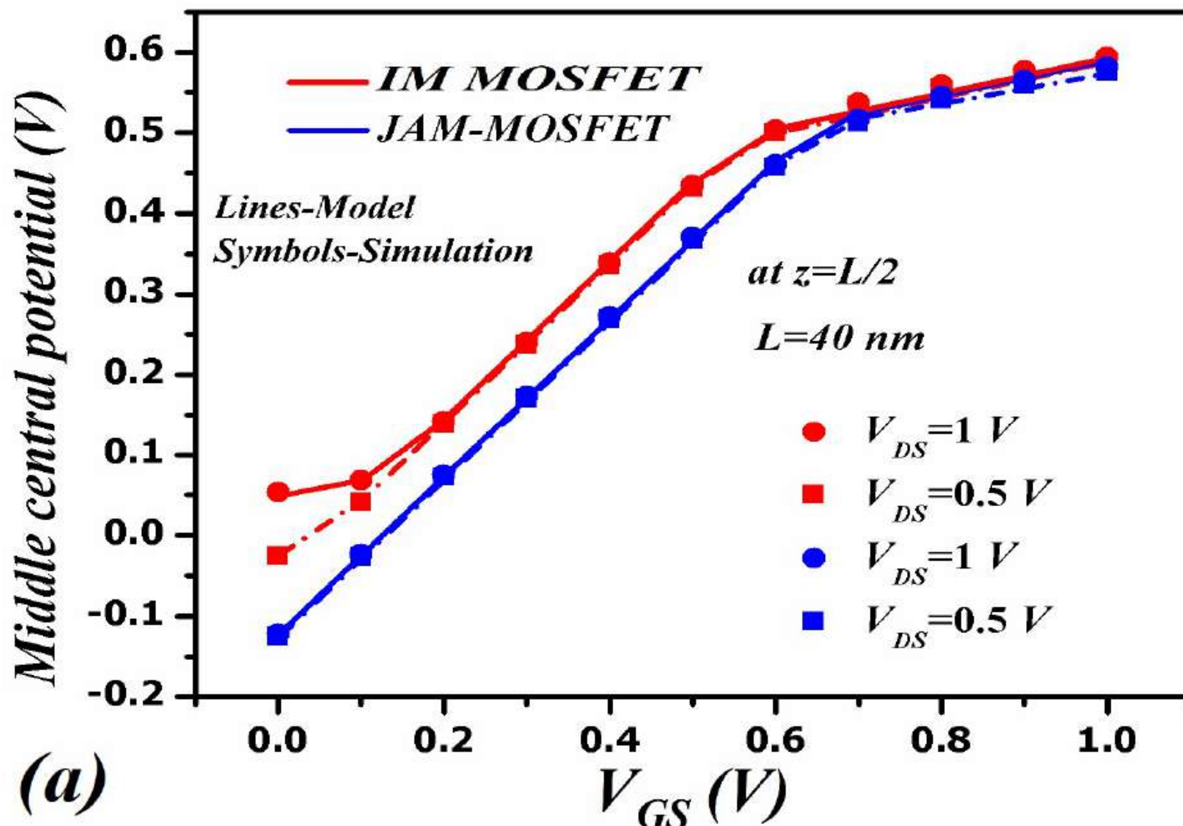

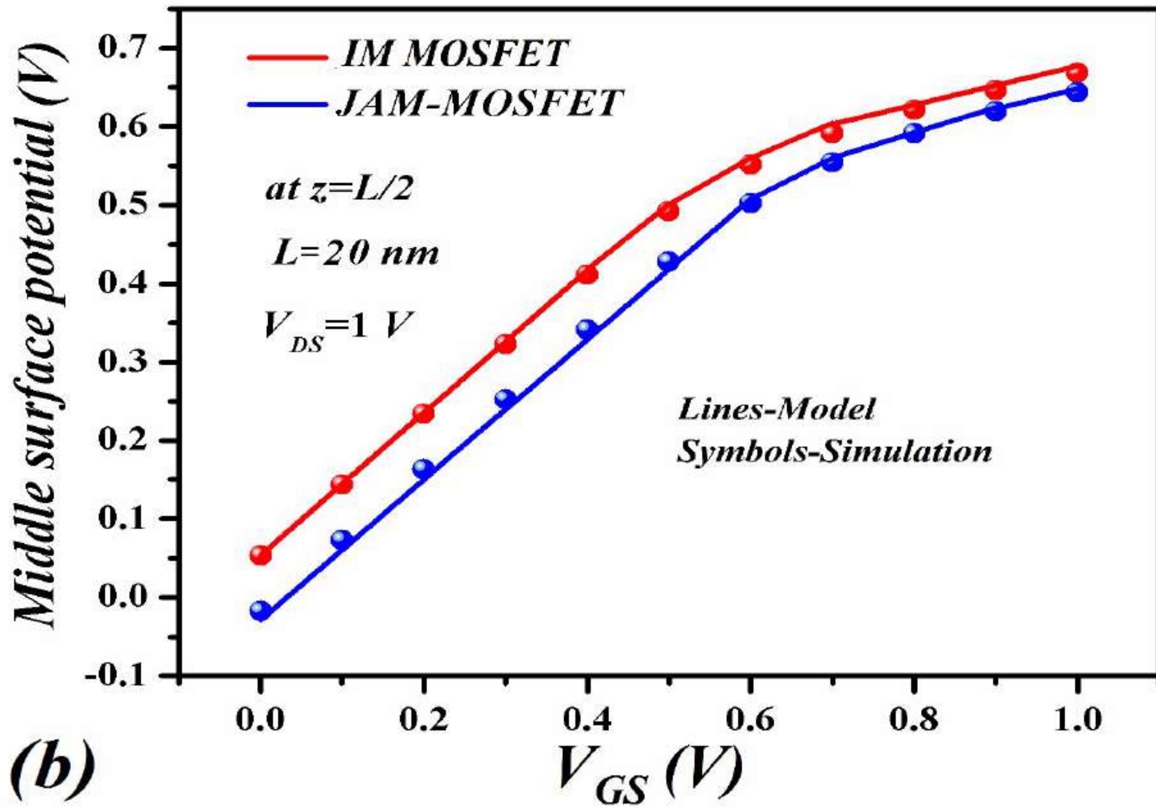

Fig. 5.3: (a) Continuity of middle central potential with the variation of V_{GS} for V_{DS}=0.5 V and 1 V (L=40 nm), (b) continuity of middle surface potential with the variation of V_{GS} for V_{DS}=1 V (L=20 nm); in both JAM and IM MOSFET.

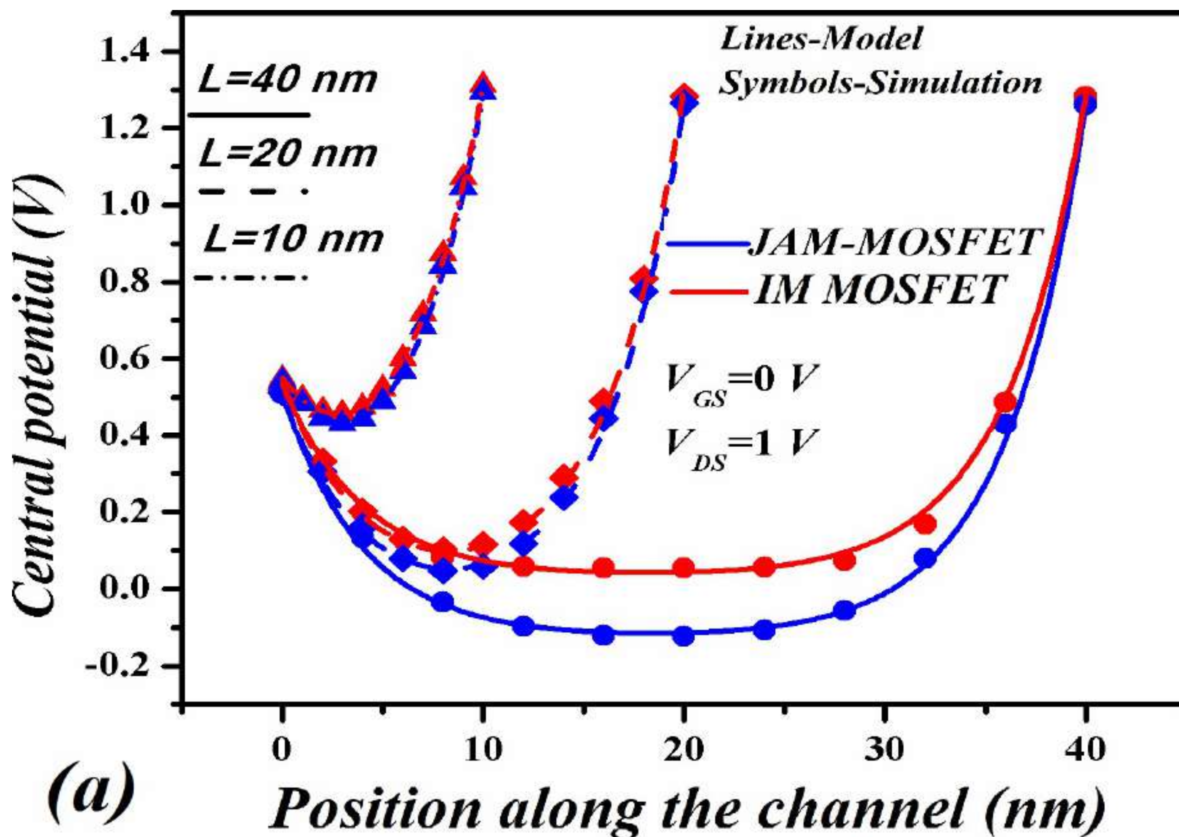

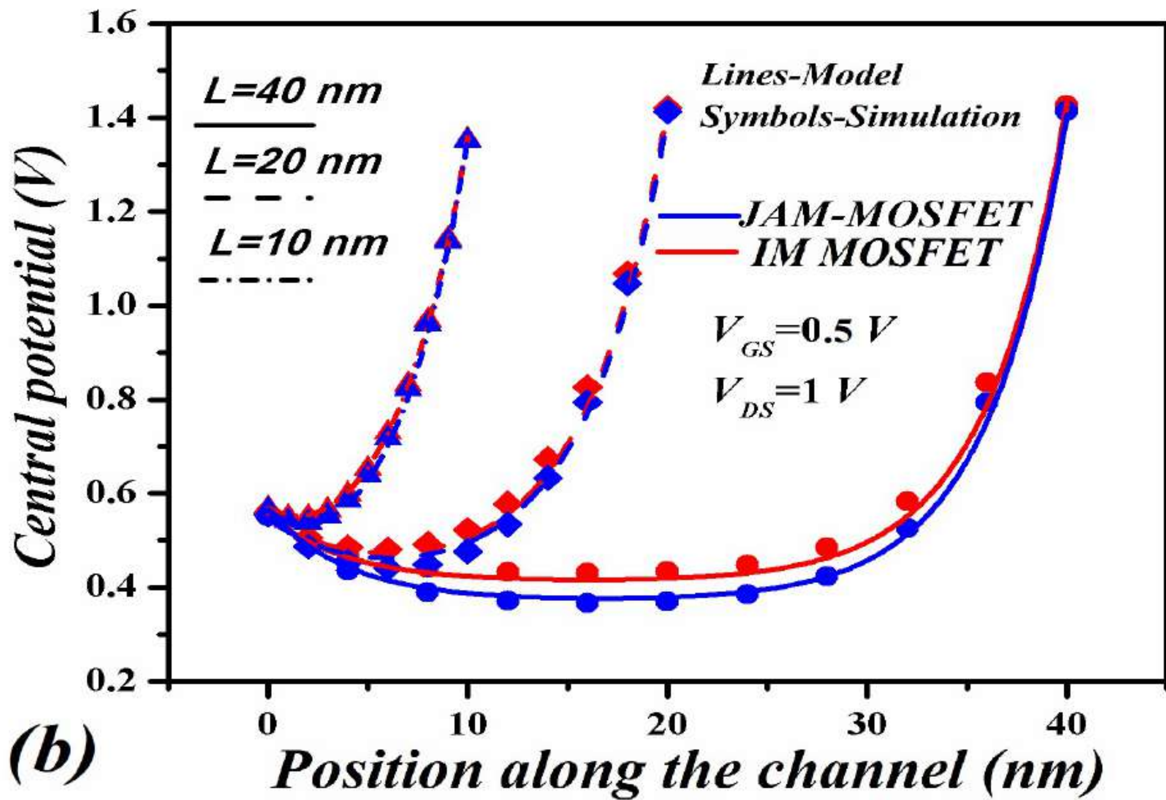

Fig. 5.4: Variation of central channel potential with position along the channel; (a) at V_{GS}=0 V and V_{DS}=1 V, (b) at V_{GS}=0.5 V and V_{DS}=1 V; for various channel lengths of L= 40 nm, 20 nm and 10 nm for both JAM and IM MOSFET.

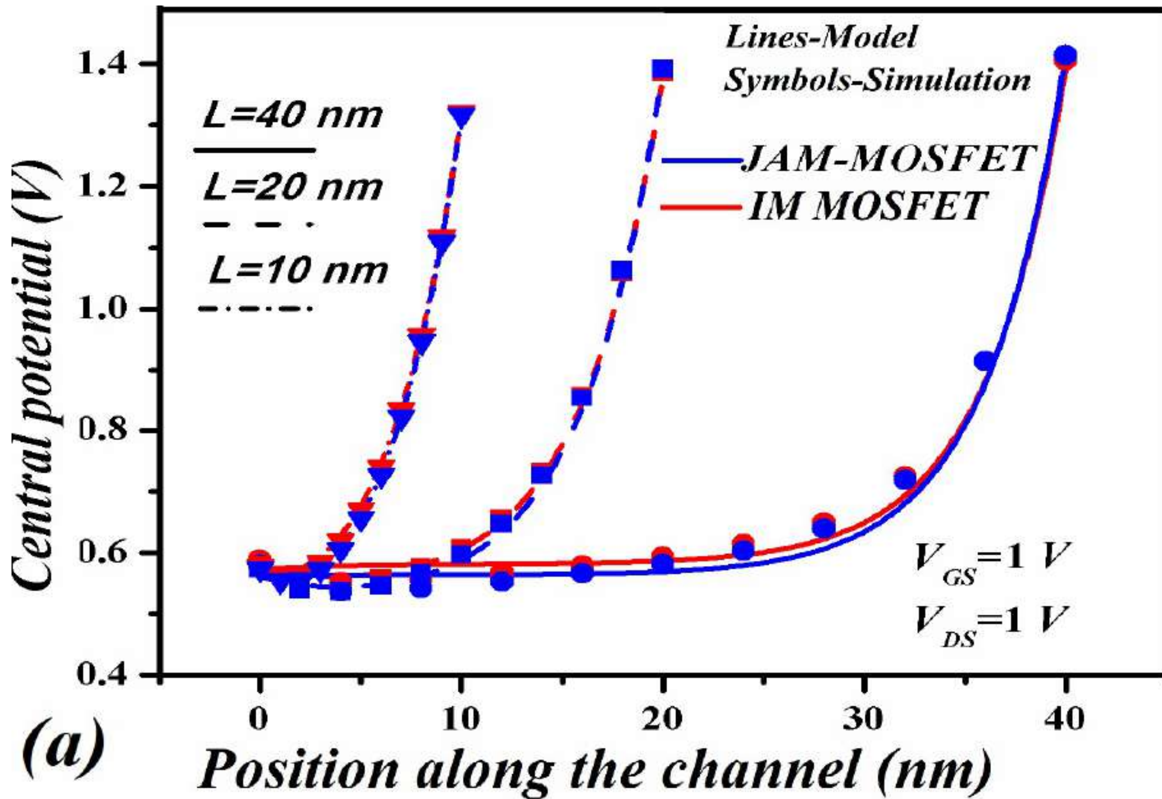

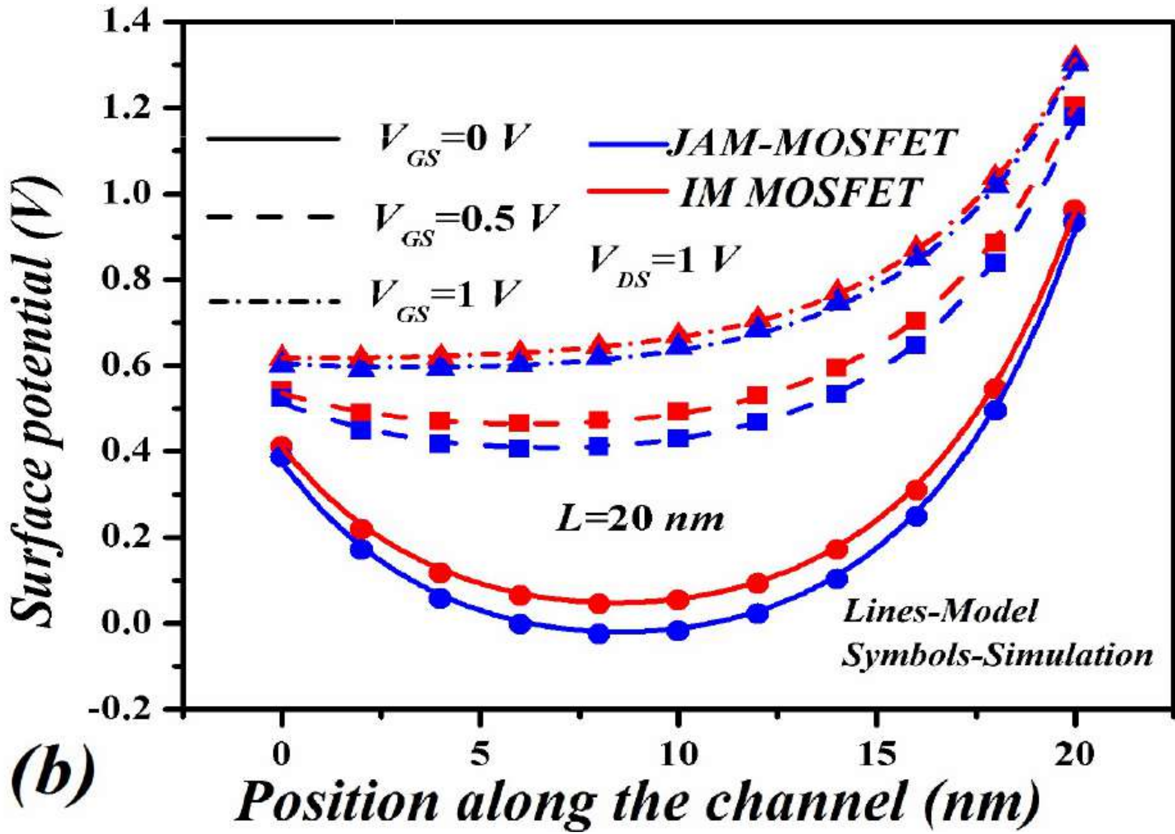

Fig. 5.5: (a) Variation of central channel potential with position along the channel at (V_{GS}=1 V and V_{DS}=1 V) for various channel lengths of L= 40 nm, 20 nm and 10 nm in both JAM and IM MOSFET, (b) variation of channel surface potential with position along the channel at (V_{GS}=0 V, 0.5 V, 1 V and V_{DS}=1 V) for channel length of L=20 nm in both JAM and IM MOSFET.

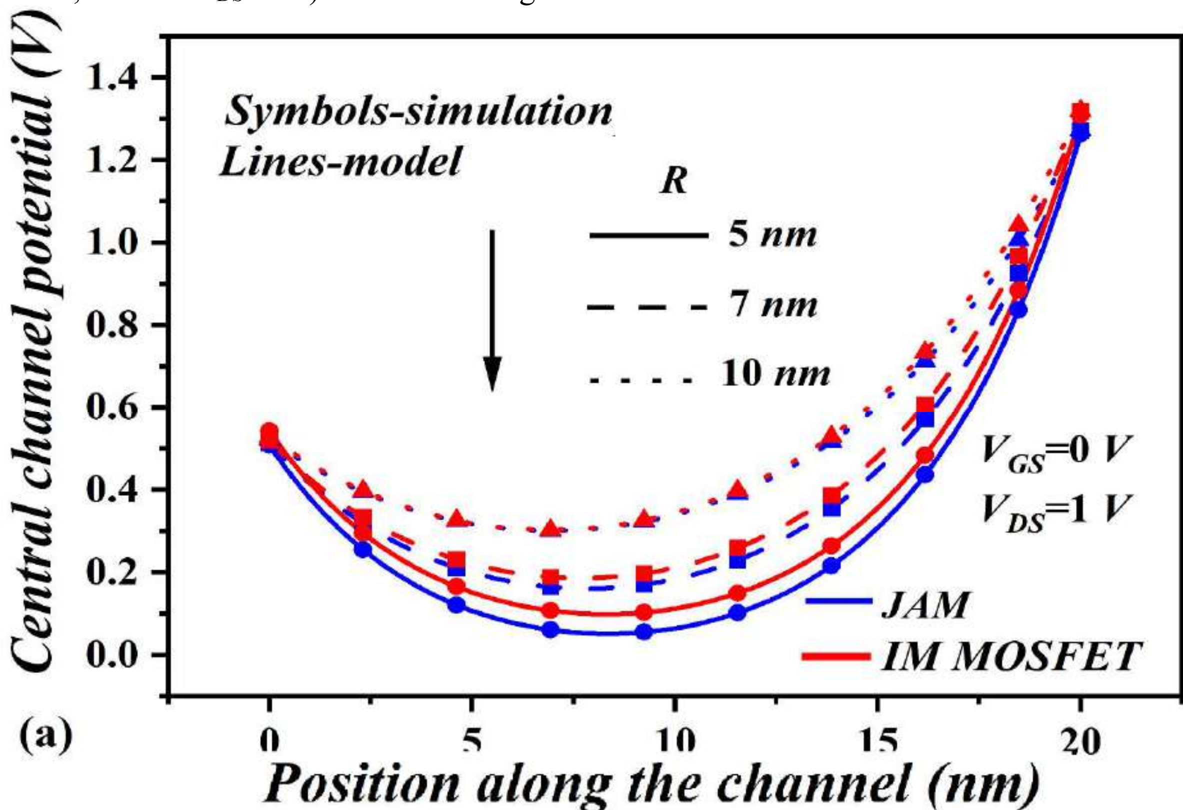

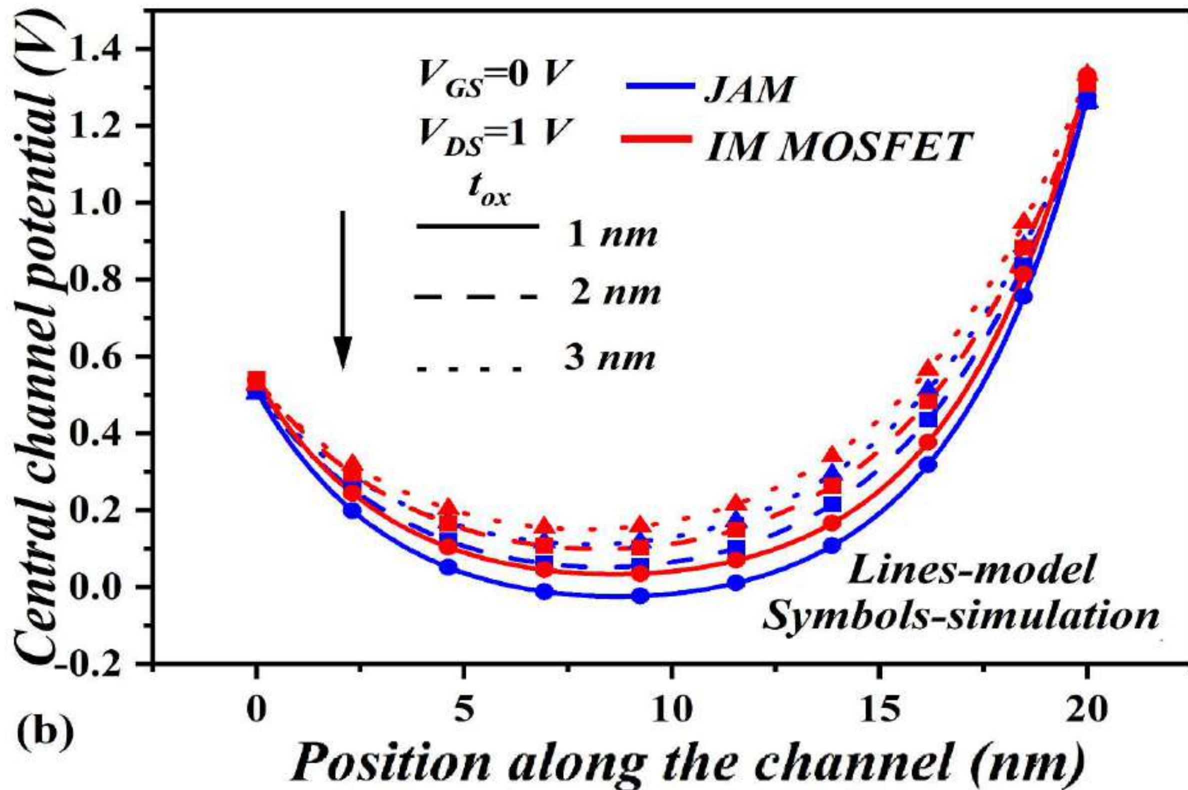

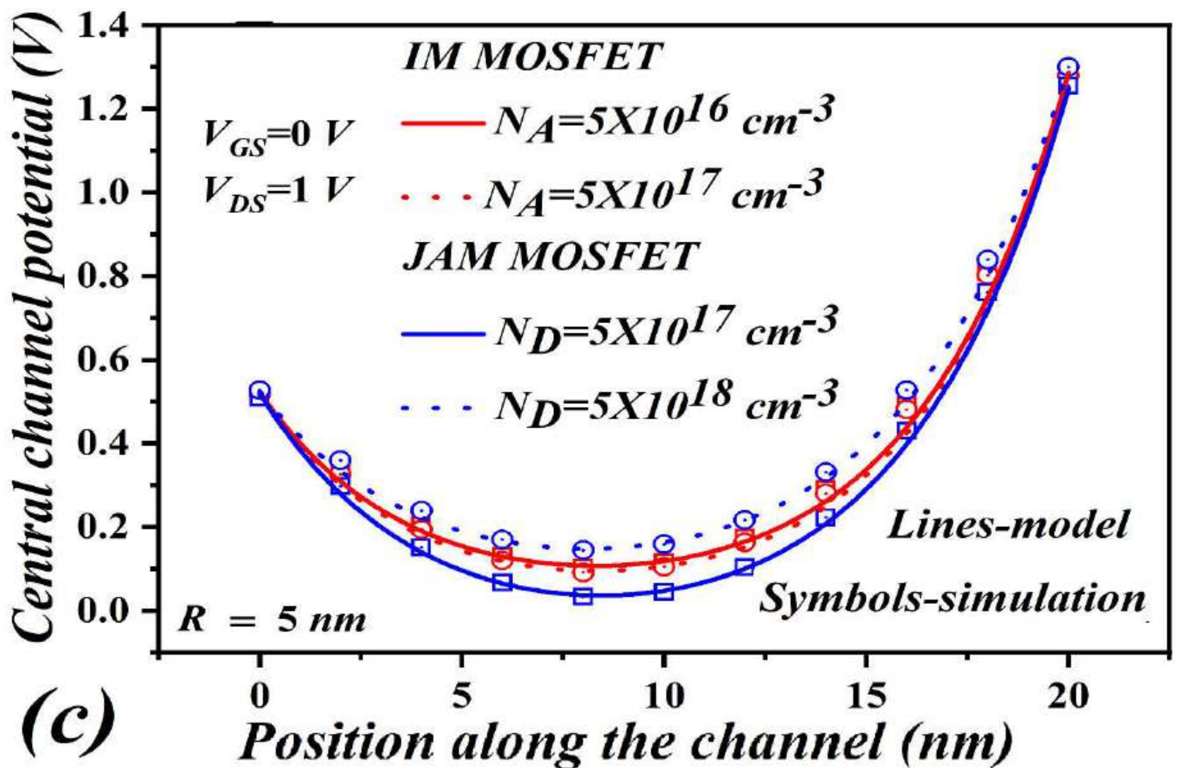

Fig. 5.6: Variation of central channel potential with position along the channel at V_{GS}=0 V and V_{DS}=1 with channel length L=20 nm; (a) for radius R=5 nm, 7 nm and 10 nm, (b) for oxide thickness t_{ox}=1 nm, 2 nm and 3 nm; (c) for different channel doping concentration [JAM MOSFET (5×10^{17}-5×10^{18}) and IM MOSFET (5×10^{16}-5×10^{17})]; in both JAM and IM MOSFET.

increase in doping. This may be attributed to the inversion mode of working for IM MOSFET compared to the bulk mode operation (behaves like a resistor) for JAM MOSFET. Further, it may also be noted that potential variation with doping change is much less for IM MOSFET compared to JAM MOSFET. Therefore, IM MOSFETs are more immune to doping variations than JAM MOSFETs. Fig 5.7(a) shows the variation of threshold voltage with different channel lengths throughout the technology nodes at V_{DS}=1 V. It could be observed that the threshold voltage for JAM MOSFET is higher than that of inversion mode MOSFET. It could be attributed to the fact that both minimum central and surface potential is higher for JAM than IM MOSFET for the considered gate workfunction and doping concentration. Fig 5.7 (b) shows the threshold voltage roll-off variations with different channel lengths at V_{DS}=1. It could be observed that the roll-off for JAM is little less (for 10 nm channel length) than IM MOSFET for the considered device specifications. Fig 5.8 shows the variation of DIBL with various

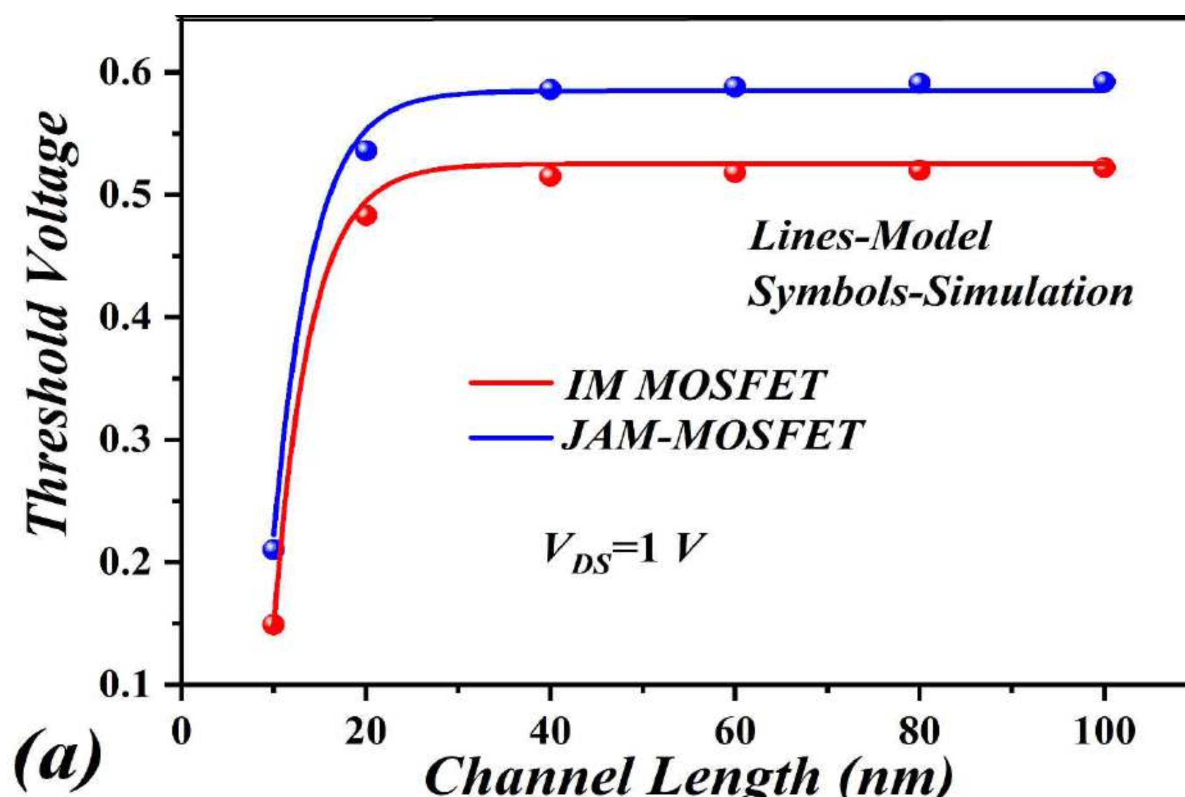

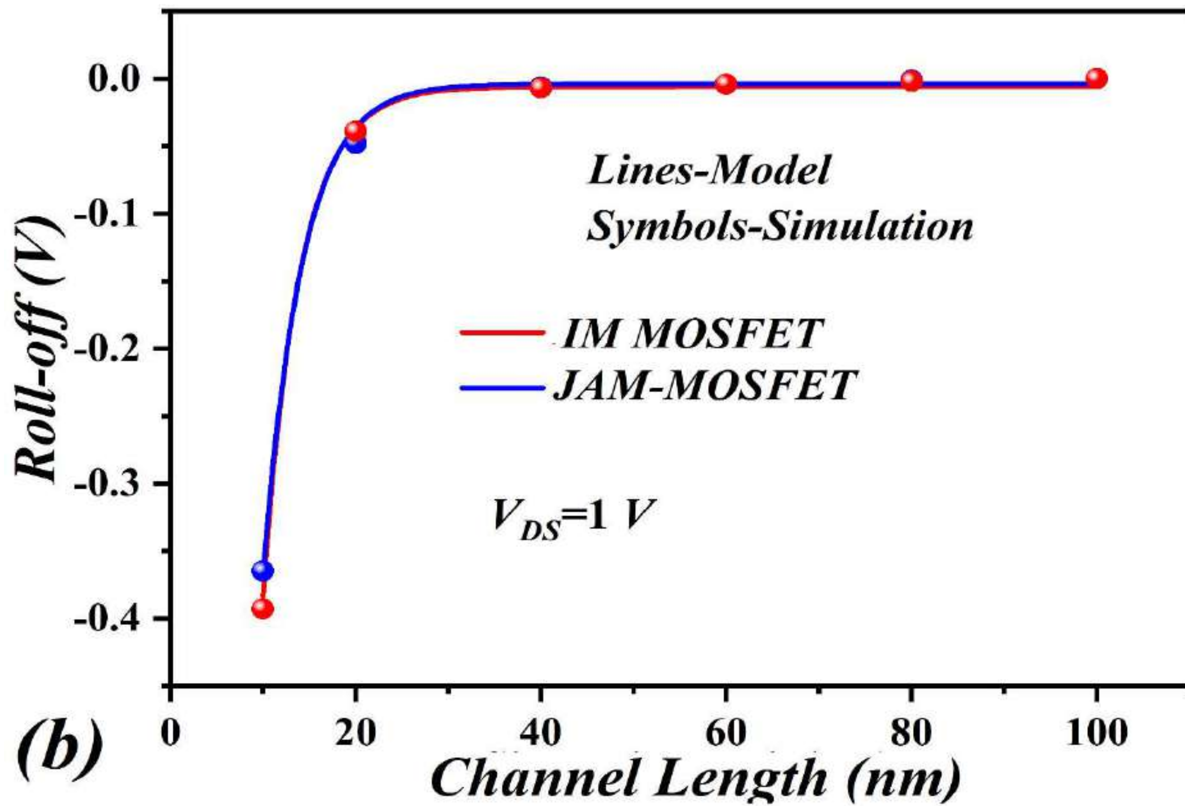

Fig. 5.7: (a) Variation of threshold voltage with the channel length, (b) variation of roll-off with channel length; at V_{DS}=1 V for compared devices.

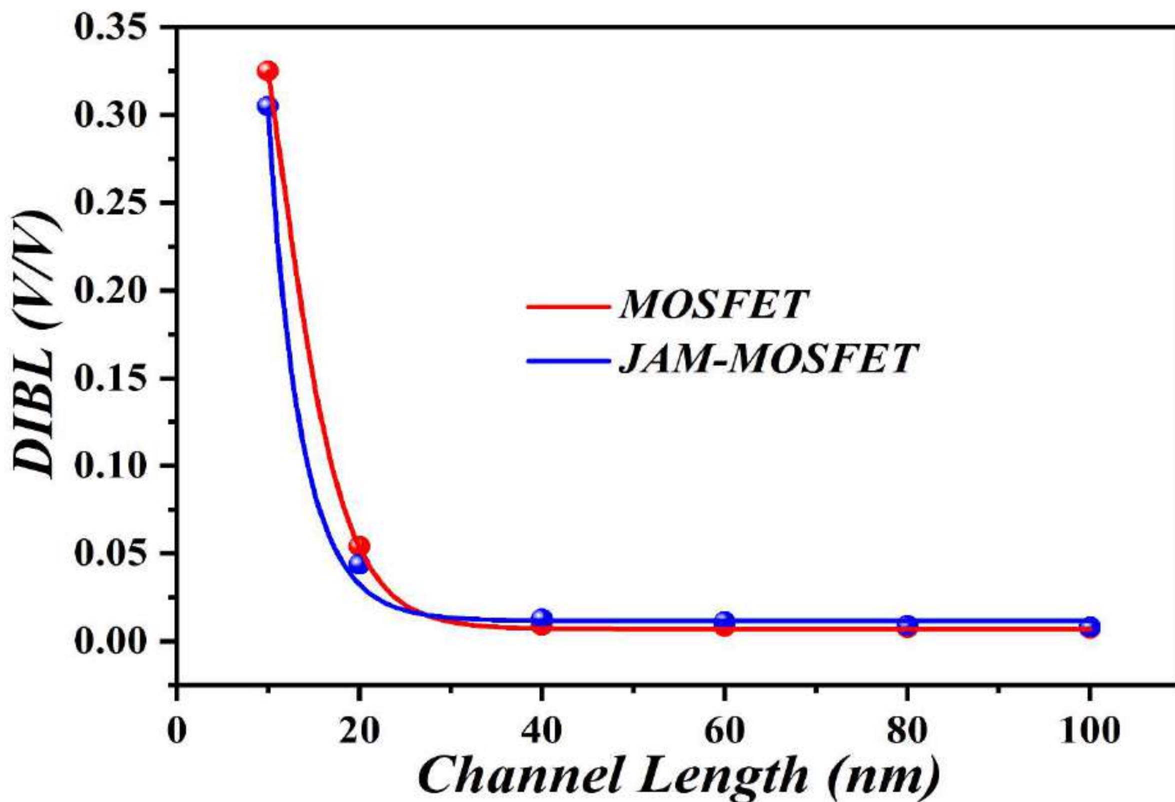

Fig. 5.8: Variation of DIBL with channel length for compared devices.

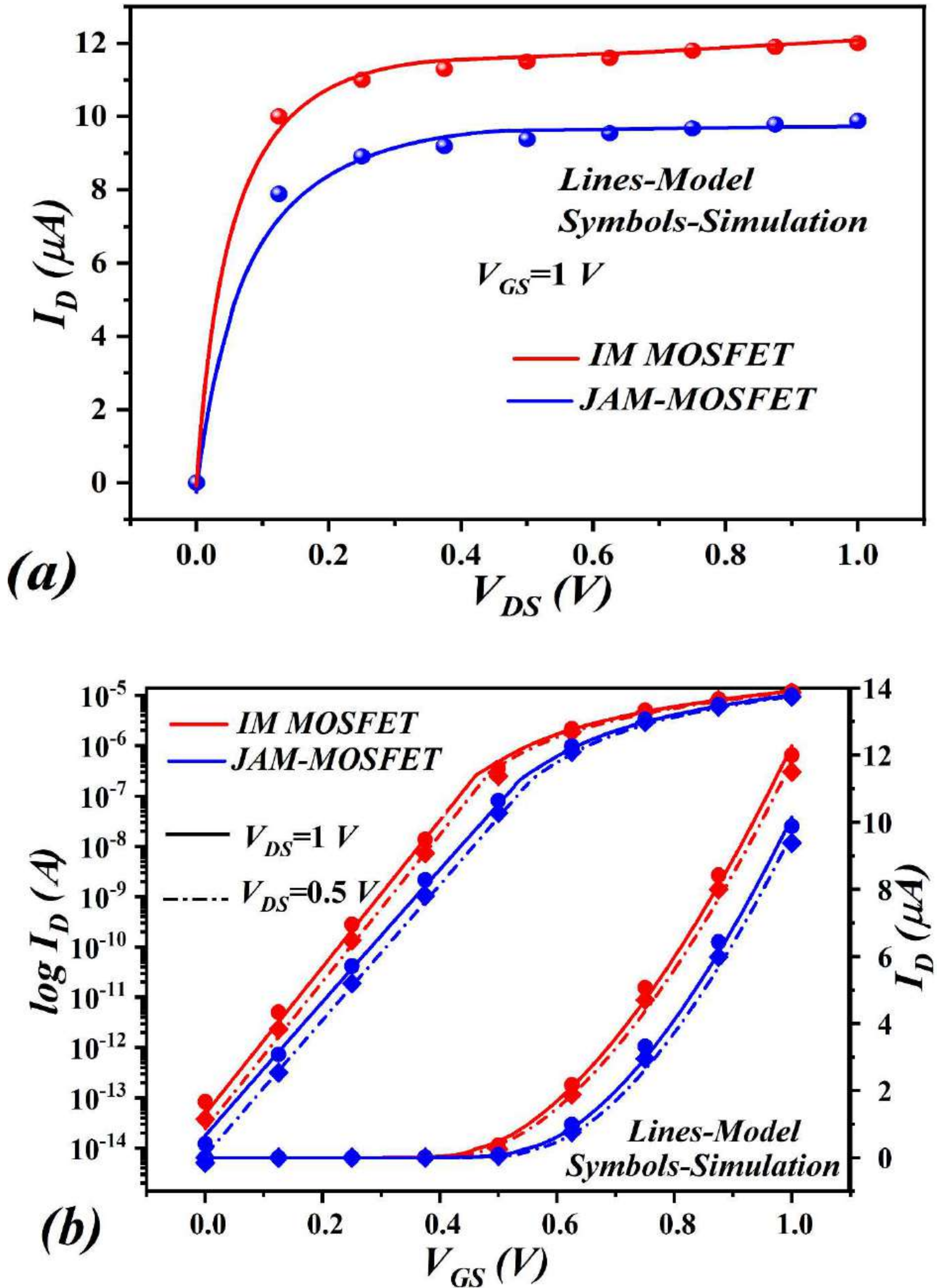

Fig. 5.9: (a) Variation of drain current (I_D) with V_{DS} at V_{GS}=1 V, (b) variation of drain current (I_D) with V_{GS} at V_{DS}=1 V and 0.5 V (in both linear and logarithmic scale); for compared devices.

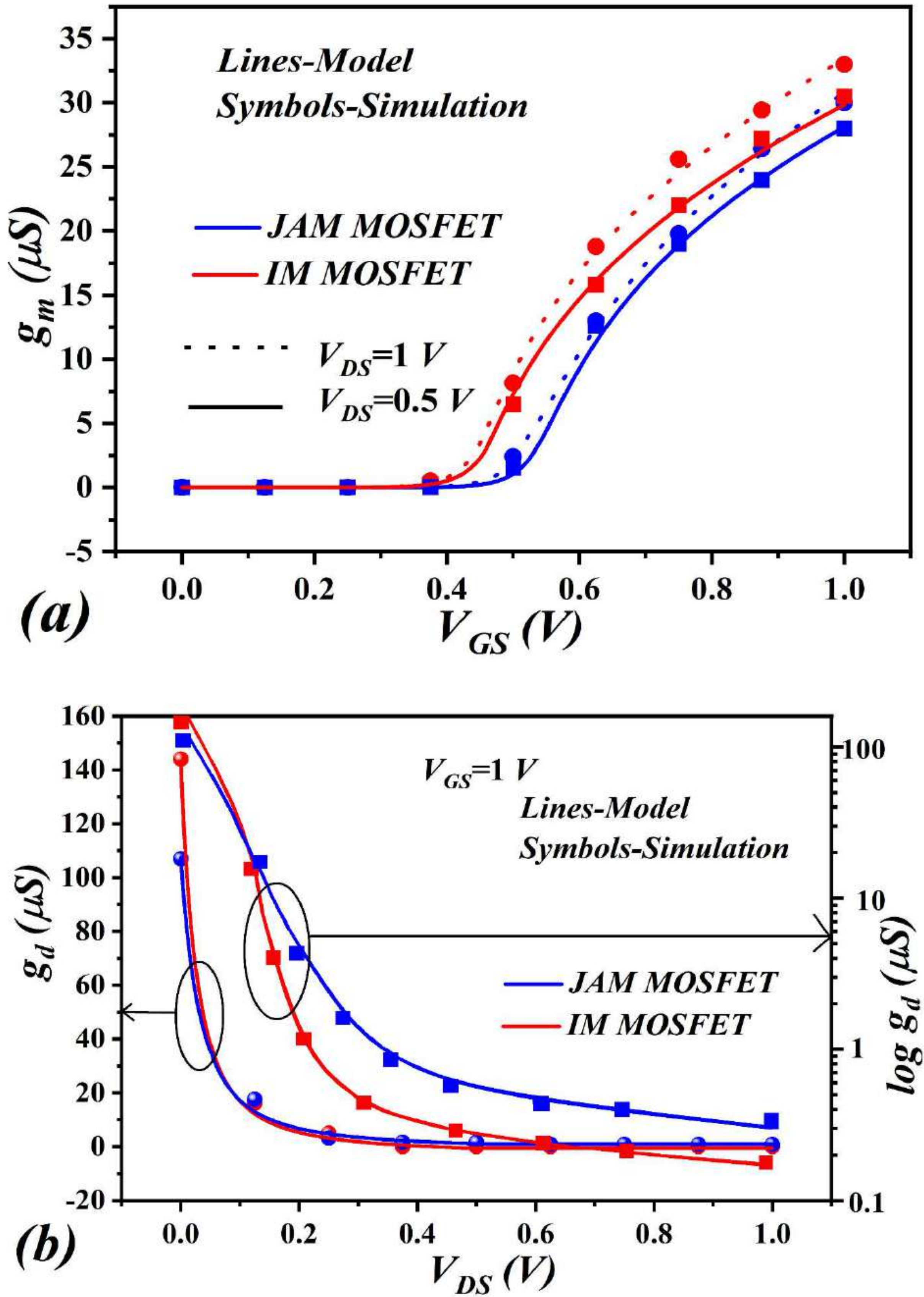

Fig. 5.10: (a) Variation of transconductance g_m with V_{GS} at V_{DS}=1 and 0.5 V, (b) variation of output conductance g_d with V_{DS} at V_{GS}=1 V in linear and logarithmic scale.

channel lengths throughout the technology nodes. It could be demonstrated from the results that JAM is more immune towards DIBL (even for 10 nm technology node) than IM MOSFET. Fig 5.9(a) demonstrates the variation of ID with VDS for 20 nm channel length devices at a fixed VGS of 1 V. It may be observed that drain current (ID) for IM MOSFET is higher than in the JAM for the considered device specifications. Moreover, ID increases slightly in saturation region in IM MOSFET compared to JAM MOSFET. Fig 5.9(b) shows the variation of ID with VGS for VDS=1 V and 0.5 V with a 20 nm channel length. The results are shown on both linear and logarithmic scales. It could be noticed that ID increases with increase in VDS above threshold region due to an increase in drain field and below threshold due to DIBL induced increase in carrier (due to reduced barrier). Further, it could also be observed that although the I_{ON} of JAM is less than MOSFET but I_{OFF} is also reduced for the considered device specifications. This increases the overall I_{ON}/I_{OFF} ratio for JAM. The first derivative of I_D-V_{DS}, I_D-V_{GS} are important DC parameters and are important to determine the continuity of the analytical drain current model. Fig 5.10(a) shows the variation of transconductance (g_m) with V_{GS} at V_{DS}=1 V and 0.5 V. Fig 5.10 (b) shows the variation of output-conductance (g_d) with V_{DS} at V_{GS}=1 V in both linear and logarithmic scale. The channel length for both the cases is 20 nm. It should be noted that both the transconductance and output-conductance are higher for inversion mode MOSFET than JAM. This could be attributed to the fact that both I_D-V_{DS} and I_D-V_{GS} are higher for inversion mode MOSFET than JAM for considered device specifications. The above discussion related to different DC electrical parameters demonstrates that our proposed analytical model matches well with the numerical simulation results. Further, it also could be demonstrated that the model works equally well for both JAM and inversion mode MOSFET and the modeled potential is continuous with gate voltage (V_{GS}). The quasi-ballistic drain current model can be used to model devices up-to 10 nm technology node. Thus,

our proposed analytical model could be well used to build a DC-compact model valid up-to 10 nm technology node (quasi-ballistic).

5.5 Conclusion

In this chapter, we have presented a unified 2-D short channel model for JAM and inversion mode MOSFET. A continuous potential model has been used to derive a quasi-ballistic drain current model. Further, threshold voltage, roll-off, DIBL, transconductance, and output-conductance has also been modeled for both JAM and inversion mode MOSFET. This analytical model can be applied to short channel length up-to 10 nm. Below the channel length of 10 nm, quantum mechanical effects and full ballistic transport between source and drain have to be treated and therefore are out of the scope for the present manuscript. Further, this model can support devices from undoped level to the doping of 10^{19} cm^{-3}, above this doping Eq. 5.35 will not converge, hence our proposed model will fail.